# Advances in PIV Uncertainty Quantification

## Towards a Comprehensive Framework

Adatrao, S.

**DOI**
10.4233/uuid:a15a3a3b-79c3-4cee-add4-bdf727606d06

**Publication date**
2023

**Document Version**
Final published version

**Citation (APA)**
Adatrao, S. (2023). *Advances in PIV Uncertainty Quantification: Towards a Comprehensive Framework*. [Dissertation (TU Delft), Delft University of Technology]. https://doi.org/10.4233/uuid:a15a3a3b-79c3-4cee-add4-bdf727606d06

# Advances in PIV Uncertainty Quantification

## Towards a Comprehensive Framework

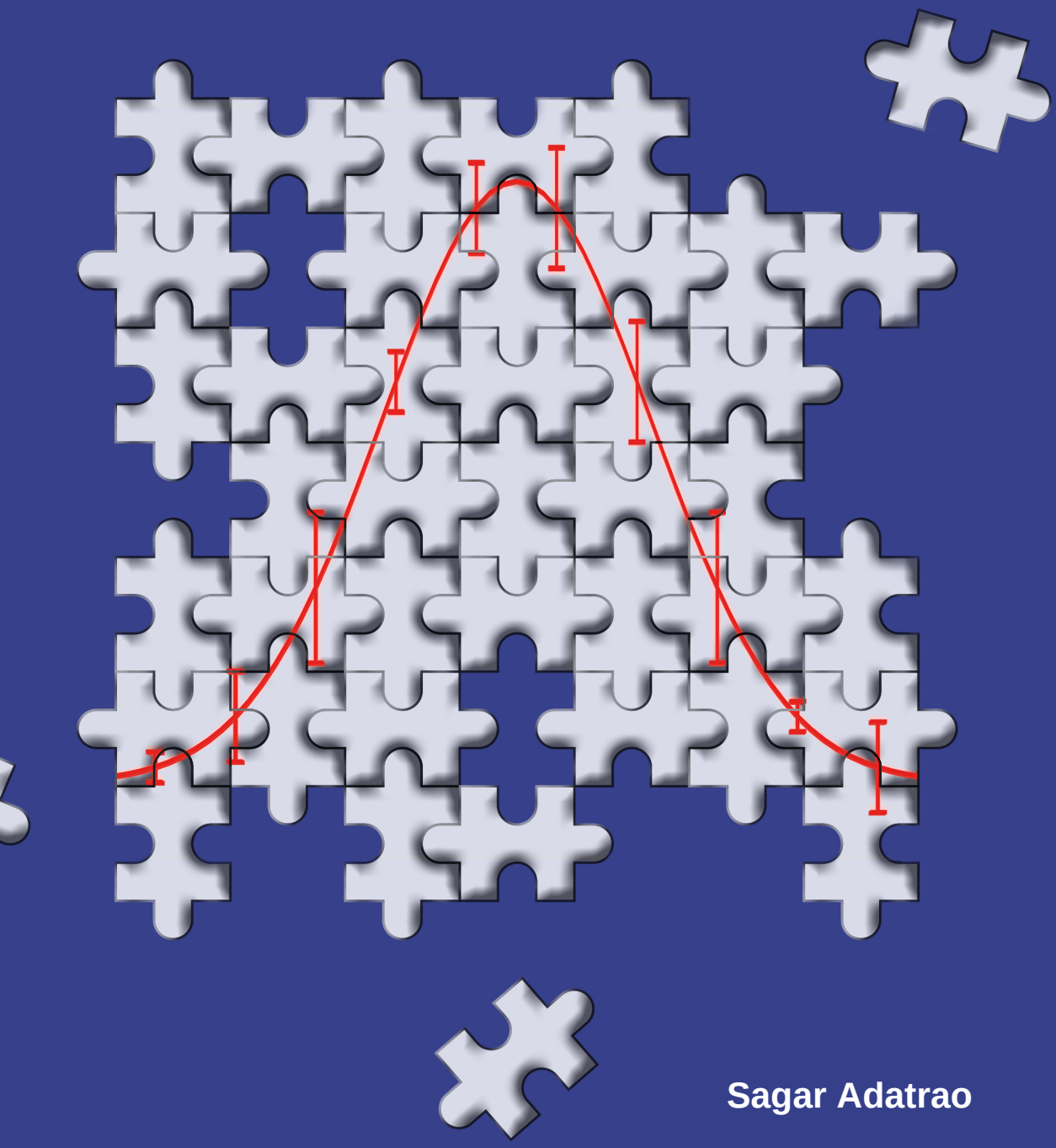

Sagar Adatrao

# Advances in PIV Uncertainty Quantification

## Towards a Comprehensive Framework

## Dissertation

for the purpose of obtaining the degree of doctor
at Delft University of Technology
by the authority of the Rector Magnificus prof.dr.ir. T.H.J.J. van der Hagen
chair of the Board for Doctorates
to be defended publicly on
Monday 11 December 2023 at 10:00 o'clock

by


## Sagar ADATRAO

Master of Science by Research in Mechanical Engineering,
Indian Institute of Technology Madras, India
born in Alibag, India

This dissertation has been approved by the promotors.

Composition of the doctoral committee:

| | |
|---|---|
| Rector Magnificus | chairperson |
| Prof.dr. F. Scarano | Delft University of Technology, promotor |
| Dr. A. Sciacchitano | Delft University of Technology, copromotor |

Independent members:

| | |
|---|---|
| Prof.dr.ir. C. Poelma | Delft University of Technology |
| Prof.dr.ing. T. Astarita | University of Naples Federico II, Italy |
| Prof.dr. B. Smith | Utah State University, The USA |
| Dr.ing. M.A. Mendez | von Karman Institute for Fluid Dynamics, Belgium |
| Dr. B. Wieneke | LaVision GmbH, Germany |
| Prof.dr.ir. C.J. Simao Ferreira | Delft University of Technology, reserve member |

ISBN: 978-94-6384-510-6



Printed by: Koninklijke Rijnja Den Haag

# Summary

Particle Image Velocimetry (PIV) is a leading technique that allows flow velocity measurements in two- and three- dimensional domains. PIV is a full-field, non-intrusive and quantitative technique. However, due to the complexity of the measurement chain, PIV results are often affected by errors from various sources. It is therefore necessary to identify these errors and quantify the uncertainties. The available PIV uncertainty quantification (UQ) approaches are limited in estimating systematic uncertainties in the measurements and mostly focus on the random uncertainty. In order to exploit full benefits of PIV, the knowledge of the full uncertainty comprising both random and systematic uncertainties is necessary. The present work proposes a comprehensive PIV-UQ framework which not only quantifies the systematic uncertainties but is also universal as it can potentially be used for any measurement irrespective of the measurement setup (e.g. planar PIV, tomographic PTV, large scale PIV or microscopic PTV) or the output quantity (e.g. mean velocity or higher order statistics).

Initially, background and motivation for the present work are discussed in chapter 1 along with objectives and outline of the thesis. Chapter 2 presents the working principle of PIV and different aspects in the acquisition and analysis of the PIV images. The errors and uncertainties in PIV are illustrated in chapter 3, where various error sources and PIV-UQ approaches are discussed.

In the present work, a survey on PIV error sources and UQ is performed and the outcomes are presented in chapter 4. The aim of the survey is to understand how users and researchers in academia and industry perceive the PIV technique, especially for what concerns the measurement errors and uncertainties.

As peak-locking is recognized as one of the major error sources in PIV measurements, a novel approach is devised for the quantification of systematic uncertainty due to peak locking which also leads to correction of

the peak-locking errors. The approach, applicable to statistical flow properties such as time-averaged velocity and Reynolds stresses, relies on image recordings with multiple time separations $\Delta t$ and a least-squares regression of the measured quantities. The methodology is assessed for planar PIV measurements of the flow over a NACA0012 airfoil in chapter 5.

A comprehensive framework based on a statistical tool called Design of Experiments (DOE) is introduced for uncertainty quantification in chapter 6. DOE allows to quantify the total uncertainty as well as the systematic uncertainties arising from various experimental factors. The approach is based on measuring a quantity (e.g. time-averaged velocity or Reynolds stresses) several times by varying the levels of the experimental factors which are known to affect the value of the measured quantity. Then, using Analysis of Variances (ANOVA), the total variance in the measured quantity is computed and hence the total uncertainty. The methodology is assessed for planar PIV measurements of the flow over a NACA0012 airfoil as well as applied to the investigation by stereoscopic PIV of the flow at the outlet of a ducted Boundary Layer Ingesting (BLI) propulsor.

Finally, a novel approach is proposed in chapter 7 to eliminate background reflections in PIV images as they produce high systematic errors in the vector fields if not removed. The approach relies upon anisotropic diffusion of the light intensity, which is used to generate a background image to be subtracted from the original image.

The thesis ends with summary of the major results and conclusions drawn in the chapters 4 to 7.

# Samenvatting

Particle Image Velocimetry (PIV) is een toonaangevende techniek waarmee stromingssnelheidsmetingen in twee- en driedimensionale domeinen mogelijk zijn. PIV is een volledig veld, niet-intrusieve en kwantitatieve techniek. Door de complexiteit van de meetketen worden de resultaten van PIV echter vaak beïnvloed door fouten uit verschillende bronnen. Het is daarom noodzakelijk om deze fouten te identificeren en de onzekerheden te kwantificeren. De beschikbare benaderingen voor het kwantificeren van de PIV-onzekerheid (Uncertainty Quantification, UQ) zijn beperkt in het schatten van systematische onzekerheden in de metingen en richten zich meestal op de willekeurige onzekerheid. Om de voordelen van PIV ten volle te benutten, is kennis van de volledige onzekerheid nodig, die zowel toevallige als systematische onzekerheden omvat. In dit werk wordt een uitgebreid PIV-UQ raamwerk voorgesteld dat niet alleen de systematische onzekerheden kwantificeert, maar ook universeel is, omdat het potentieel voor elke meting kan worden gebruikt, ongeacht de meetopstelling (bijv. planaire PIV, tomografische PTV, grootschalige PIV of microscopische PTV) of de outputgrootheid (bijv. gemiddelde snelheid of statistieken van hogere orde).

In hoofdstuk 1 worden eerst de achtergrond en motivatie van dit werk besproken, samen met de doelstellingen en de opzet van het proefschrift. Hoofdstuk 2 presenteert het werkingsprincipe van PIV en verschillende aspecten bij het verwerven en analyseren van de PIV-beelden. De fouten en onzekerheden in PIV worden geïllustreerd in hoofdstuk 3, waar verschillende foutbronnen en PIV-UQ benaderingen worden besproken.

In dit werk wordt een onderzoek uitgevoerd naar PIV-foutenbronnen en UQ en de resultaten worden gepresenteerd in hoofdstuk 4. Het doel van de enquête is om te begrijpen hoe gebruikers en onderzoekers in de academische wereld en de industrie tegen de PIV-techniek aankijken, vooral wat betreft de meetfouten en -onzekerheden.

Aangezien peak-locking wordt gezien als een van de belangrijkste foutbronnen in PIV-metingen, is een nieuwe aanpak ontwikkeld voor de kwantificering van de systematische onzekerheid als gevolg van peak-locking, die ook leidt tot correctie van de peak-locking fouten. De aanpak, die toepasbaar is op statistische stromingseigenschappen zoals tijdgemiddelde snelheid en Reynolds spanningen, is gebaseerd op beeldopnames met meerdere tijdseparaties $\Delta t$ en een kleinste-kwadraten regressie van de gemeten grootheden. De methodologie wordt beoordeeld voor vlakke PIV metingen van de stroming over een NACA0012 aërodynamisch vlak in hoofdstuk 5.

In hoofdstuk 6 wordt een uitgebreid raamwerk voor onzekerheidskwantificering geïntroduceerd, gebaseerd op een statistisch hulpmiddel genaamd Design of Experiments (DOE). DOE maakt het mogelijk om zowel de totale onzekerheid als de systematische onzekerheden te kwantificeren die voortkomen uit verschillende experimentele factoren. De aanpak is gebaseerd op het meermaals meten van een grootheid (bijvoorbeeld tijdgemiddelde snelheid of Reynoldsspanningen) door de niveaus van de experimentele factoren, waarvan bekend is dat ze de waarde van de gemeten grootheid beïnvloeden, te variëren. Vervolgens wordt met behulp van ANOVA (Analysis of Variances) de totale variantie in de gemeten grootheid berekend en daarmee de totale onzekerheid. De methodologie wordt beoordeeld voor vlakke PIV-metingen van de stroming over een NACA0012-airfoil en toegepast op het onderzoek met stereoscopische PIV van de stroming bij de uitlaat van een gekanaliseerde Boundary Layer Ingesting (BLI) propulsor.

Ten slotte wordt in hoofdstuk 7 een nieuwe aanpak voorgesteld om achtergrondreflecties in PIV-beelden te elimineren, omdat deze hoge systematische fouten in de vectorvelden veroorzaken als ze niet worden verwijderd. De aanpak is gebaseerd op anisotrope diffusie van de lichtintensiteit, die wordt gebruikt om een achtergrondbeeld te genereren dat van het originele beeld wordt afgetrokken.

Het proefschrift eindigt met een samenvatting van de belangrijkste resultaten en conclusies uit de hoofdstukken 4 tot en met 7.

# Table of Contents

# Chapter 1
# Introduction

## 1.1. Background

Most of the natural and man-made phenomena deal with fluid flows. Fluid dynamics is a branch of science which deals with basic understanding as well as complex applications of the fluid flows. Aerodynamics, for example, plays an important role in the design and development of aircraft. The air flow around the aircraft needs to be studied to investigate its performance in presence of different flow conditions. This aerodynamic study can be carried out by means of theoretical computation, numerical analysis or experimental investigation.

The theoretical approach is based on the analytical solution of non-linear differential equations called the Navier-Stokes equations. This approach is only used for very simple flows and geometries because of the complexity of solving those equations (Anderson 2011, among others).

The numerical analysis or computational fluid dynamics (CFD) relies on solving the continuous equations with the help of computers after discretizing them. Large eddy simulation (LES) and Reynolds averaged Navier-Stokes (RANS) equations are computationally less expensive as compared to direct numerical simulation (DNS). The LES and RANS are characterized by the assumptions on the behaviour of small turbulent scales, whereas the DNS solves the Navier-Stokes equations without any models for turbulent properties so that all motions in the flow are resolved (Robinson 1991, among others).

The experimental investigations are necessary in the cases of complex fluid flows and models where the accuracy of theoretical approach and numerical simulations might not be high, especially close to the boundaries of the model. In early days, the flow measurements were mostly carried out with

probe-based techniques like Pitot tube (Pitot 1732) and hot-wire anemometry (HWA, Fingerson and Freymuth 1983). Laser Doppler velocimetry (LDV, Adrian 1983) was the first non-intrusive technique used for velocity measurements. However, these three techniques are point-wise techniques in the sense that they measure the velocity at a single location in the flow. That makes it very laborious if one is interested in the velocity field along a plane or volume in the flow. The problem was solved by adding seeding particles in the flow and illuminating them by a light source by Prandtl (1905) so that the velocity at numerous points in the flow can be evaluated at a time. The images of the seeding particles show streaks which represent the motion of the particles and hence the motion of the fluid. The technique was named as particle streak velocimetry. The main drawback of the technique is the use of limited number of tracer particles due to overlapping streaks, resulting in relatively lower spatial resolution. To overcome the limitations of particle streak velocimetry, a technique called particle image velocimetry (PIV) was introduced (Adrian 1991) which is characterized by higher spatial resolution and accuracy due to better flow illumination and processing algorithms.

## 1.2. PIV in brief

PIV is the chief technique for the quantitative visualization of fluid flows. The concept of PIV is to measure the displacement of seeding or tracer particles mixed in the fluid over a short time interval. It is to be noted that the seeding particles should follow the fluid flow accurately. As shown in figure 1.1, the seeding particles are illuminated by a light source such as a pulsed laser and the light scattered by the particles is recorded by a digital camera. The digital images are captured as two frames separated by a short time gap $\Delta t$. The displacement of the particles during this time interval is estimated by cross-correlation of the two image frames. The measured displacement of the particles is easily converted to their velocity using the value of $\Delta t$. Since it is assumed that the particles follow the flow perfectly, their displacement or velocity can be equated to that of the fluid flow.

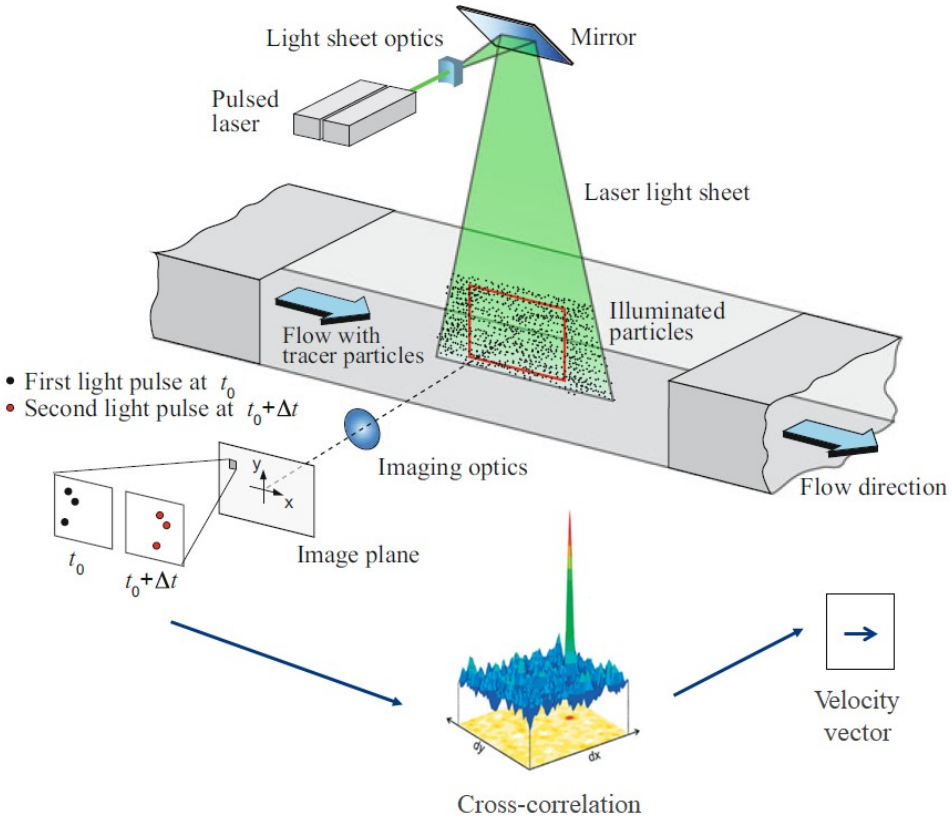


Figure 1.1. A typical set-up of planar PIV, adapted from Raffel et al. (2018)

PIV is widely used for fluid dynamics experiments in universities, research institutes and industries. Its applications are in various fields like turbulence research (Westerweel et al. 2013), hypersonic flows (Schrijer et al. 2006), turbo machineries (Wernet 1997), aeroacoustics (Tuinstra et al. 2013), micro-channels (Meinhart et al. 1999), combustion (Honoré et al. 2000), biomedical flows (Jamison et al. 2012), etc. Some of the PIV applications are illustrated in figure 1.2.

# 1. Introduction

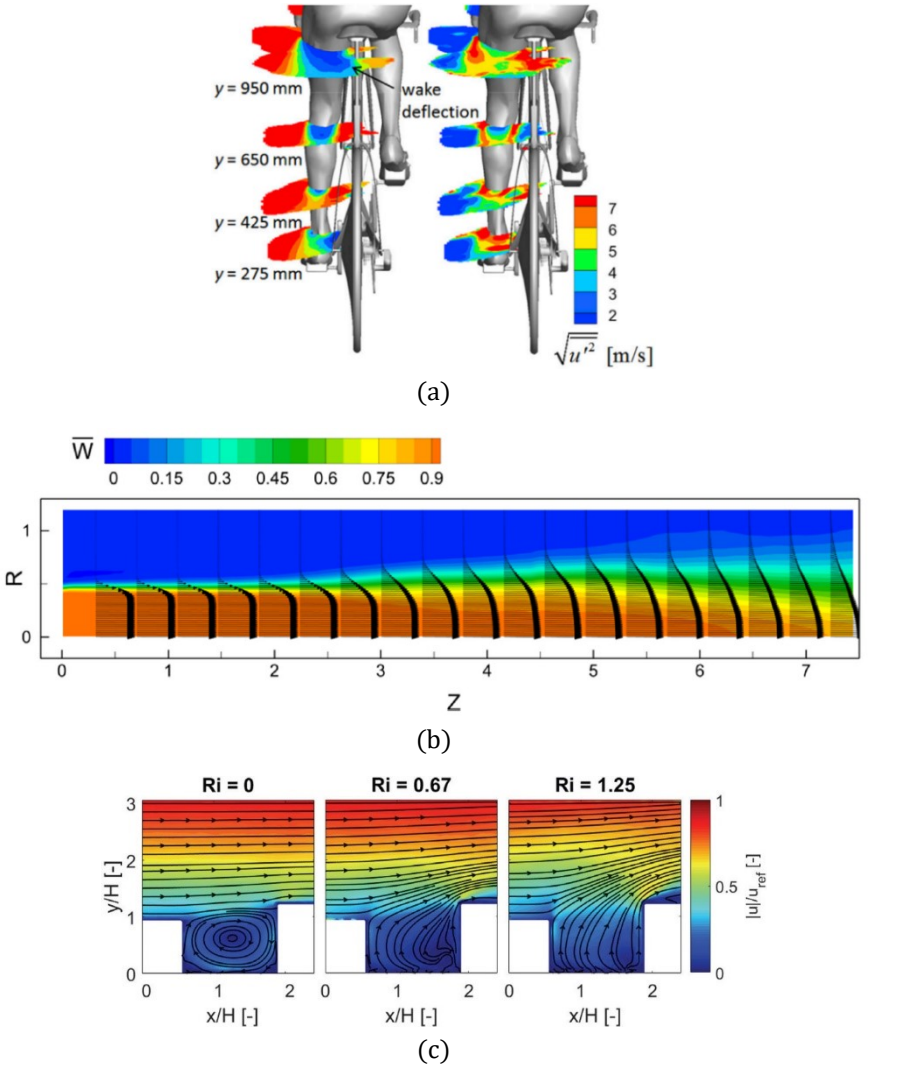


Figure 1.2. Examples of PIV applications: (a) Streamwise velocity fluctuations at different planes along leg of a full-scale cyclist mannequin, experiment conducted at Open Jet Facility in TU Delft (Terra et al. 2020); (b) Iso-contours of mean axial velocity of a circular jet at the nozzle exit, experiment conducted at water facility at the Aerodynamic Laboratories of TU Delft (Violato and Scarano 2011); (c) Mean velocity magnitude contours for different Richardson number in urban flow over a model of a city quarter in a newly built part of Zürich, experiment conducted at Empa Atmospheric Boundary Layer (ABL) wind tunnel in ETH Zürich (Tsalicoglou et al. 2018)

## 1.3. Motivation for the present work

PIV is a full-field, non-intrusive and quantitative technique. These advantages make it potentially suitable for understanding complex flows, aerodynamic certification and validation of results based on numerical simulations (computational fluid dynamics, CFD). However, the technique is seldom employed outside universities. Its use in industry is extremely scattered because PIV data are not considered sufficiently trustworthy for system certification and design validation on top of high cost of the PIV system and high cost of training people to use it. Figure 1.3 shows an example of CFD validation by PIV for an airfoil with circulation control (Jones et al. 2008). Although numerical and experimental results show clear similarities, they do not match perfectly. We cannot validate the CFD simulations by comparing them with PIV results as long as PIV uncertainty (i.e. an interval that likely contains the error) is unknown.

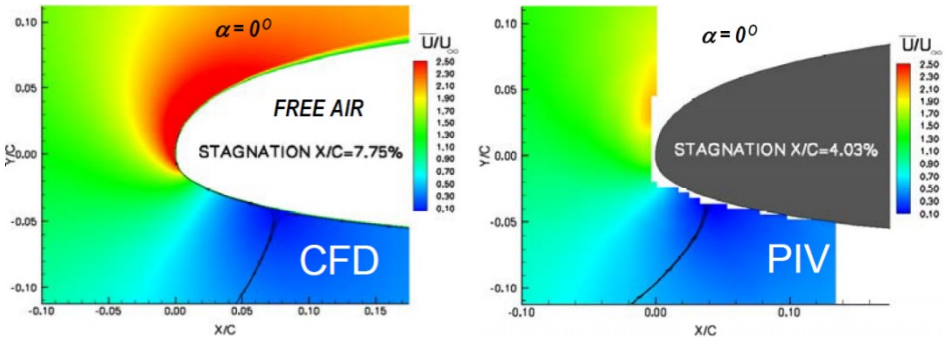


Figure 1.3. Comparison between CFD and PIV: velocity field and stagnation streamline of the leading edge of an airfoil with circulation control (Jones et al. 2008)

Despite the quantification of the PIV uncertainty being the key to discern measurement errors from the true flow physics, PIV uncertainty quantification (UQ) is often hindered by the complexity of the measurement chain, which introduces errors from various sources such as particles, illumination, calibration, imaging and processing. Most of the early approaches for PIV-UQ are a-priori based on theoretical modelling or Monte

Carlo simulations (Westerweel 2000, Westerweel 2008, Stanislas et al. 2005, Stanislas et al. 2008, Kähler et al. 2016, among others). Those approaches often yield largely inaccurate uncertainty estimates, because of simplified hypotheses or the assumption of too idealized conditions. Several a-posteriori approaches have also been proposed for PIV-UQ (Timmins et al. 2012, Sciacchitano et al. 2013, Charonko and Vlachos 2013, Xue et al. 2015, Wieneke 2015, Bhattacharya et al. 2018), which evaluate the uncertainty directly from the computed displacement or velocity field. However, such approaches mostly focused on quantifying the uncertainty from random errors and were limited in the quantification of the systematic uncertainty (Sciacchitano et al. 2015). The reader is referred to chapter 3 for more information on these PIV-UQ approaches along with their advantages and limitations.

In volumetric and tomographic PIV measurements, a-posteriori UQ is further complicated by the use of multiple cameras, calibration and presence of ghost particles (i.e. reconstruction noise produced by erroneous reconstruction of actual particles at incorrect locations due to multiple lines of sight of the multiple cameras). Approaches based on the compliance with physical laws have been proposed (Atkinson et al. 2011, Scarano and Poelma 2009) which have limited applicability and rely upon assumptions often not verified.

It is also worth to note that most of the measurements or experiments also feature errors in the results due to subjective error sources like human factor, changes in surrounding, etc. Figure 1.4 shows velocity field measurements in a confined array of cylinders (Smith and Oberkampf 2014). These measurements were repeated daily over the course of a month in the facility shown in figure 1.4(a). A sample of time-averaged stream-wise velocity profiles behind the fourth cylinder is shown in figure 1.4(b). It is clear from these data that the position of the wake varied daily. These variations in state of the flow field would lead to changes in velocity at any particular position that were much larger than the instrument uncertainty.

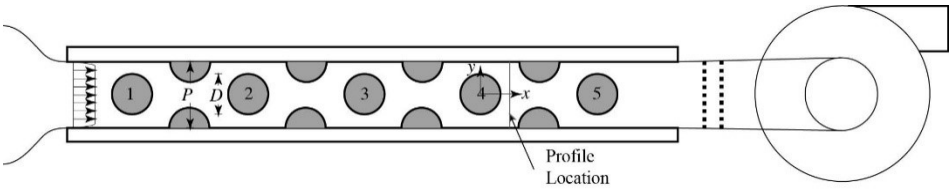


(a)

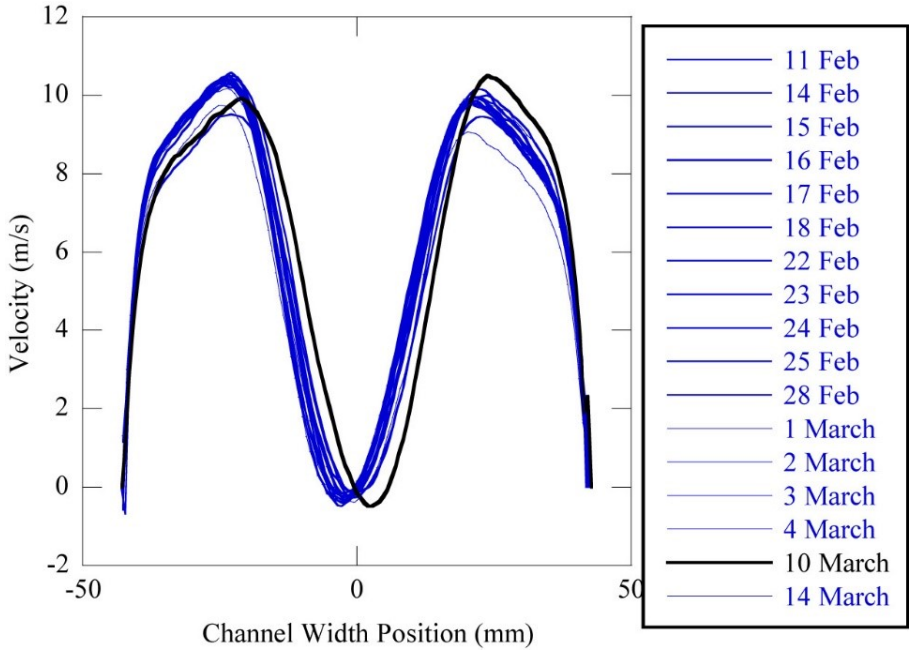


(b)

Figure 1.4. (a) Schematic of the flow facility discussed in Harris et al. (2013), flow is from left to right; (b) Time-averaged stream-wise velocity acquired on the line indicated in the experimental setup in (a) over the course of more than one month, adapted from Smith and Oberkampf (2014)

Moreover, the main results of the 4th international PIV challenge (Kähler et al. 2016) showed that, even for the same set of image recordings, large differences in the PIV results occurred among the participants due to the selection of the different processing parameters. Additionally, the systematic errors in PIV arise not only in the selection of the processing

algorithm and the related parameters, but also during the data acquisition phase (Sciacchitano 2019). For instance, peak-locking errors were found to be dependent on the inter-frame time separation by Nogueira et al. (2011), Legrand et al. (2012), among others. Because PIV-UQ algorithms do not account for the systematic error sources or account for them only partly, they give an incomplete or underestimated prediction of the total uncertainty. In order to optimize the PIV data acquisition and processing of a specific experiment, it is crucial to know which experimental factors contribute the most to the uncertainty of the measured velocity fields.

Thus, the investigations up till now provide an incomplete picture on the PIV uncertainty. If we want to fully exploit the potential of PIV for fluid dynamics research and development, the work must be completed including systematic uncertainty.

There are a large number of researchers worldwide who use PIV for flow measurements. The error sources encountered by them and the UQ approaches they employ depend on their level of experience, the type of experimental setup (e.g. planar PIV, stereoscopic PIV, tomographic PIV/PTV or LPT, micro-PIV, etc.), the flow cases (e.g. high speed flow, multi-phase flow, etc.) and flow properties (e.g. instantaneous or statistically derived) of interest (Kähler et al. 2016). Therefore, conducting a survey and collecting their opinions would create awareness in the PIV community and foster further developments for error minimization.

Peak-locking (also referred to as pixel-locking) is recognized as one of the major error sources in PIV measurements. Such an error source, mainly ascribed to particle image diameters small with respect to the sensor's pixel size, causes a bias of the measured particle image displacement towards the closest integer value (Westerweel 1997, Adrian and Westerweel 2011, Michaelis et al. 2016, Raffel et al. 2018). It is particularly relevant in high-speed PIV measurements with CMOS cameras, whose large pixel size (of the order of 10 to 20 μm) yields particle image diameters often smaller than one pixel. For example, peak locking can be detected in vector fields when there are dominant vortical structures in the flow field and the relative variation of the measured velocities is small. Due to the peak-locking errors the

circular cross-sectional shapes of the vortices are altered, as illustrated in figure 1.5 (Raffel et al. 2018).

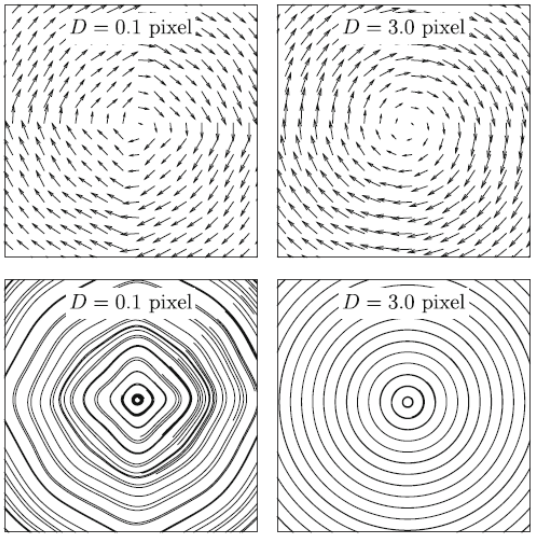


Figure 1.5. The effect of peak locking on vector field and stream lines of a synthetic Lamb-Oseen vortex for two particle image diameters. The maximum displacement is only 0.5 pixel (Raffel et al. 2018)

It is to be noted that the measurements with particle image diameters greater than one pixel are also affected by the peak-locking errors, although the peak-locking errors are likely to be less prominent than the random errors in this case (Westerweel 1997). Thus, the recent development of high-speed cameras has been influencing the study on peak-locking errors and their correction in PIV. Moreover, the peak-locking errors significantly affect the turbulence statistics extracted from the PIV measurements. When the flow velocity fluctuations encompass at least one pixel unit, the mean velocity is usually unaffected by the peak-locking errors in the instantaneous velocities. In such cases, the peak-locking errors appear instead in the fluctuations of velocity leading to inaccurate estimation of higher-order turbulence statistics, e.g. Reynolds stresses (Christensen 2004). Hence, the quantification and correction of the peak-locking errors in the PIV measurements is crucial for the evaluation of accurate turbulence statistics.

## 1. Introduction

The problem of peak-locking errors due to small particle image diameters, especially in the case of CMOS cameras for high-speed PIV measurements, is still unsolved.

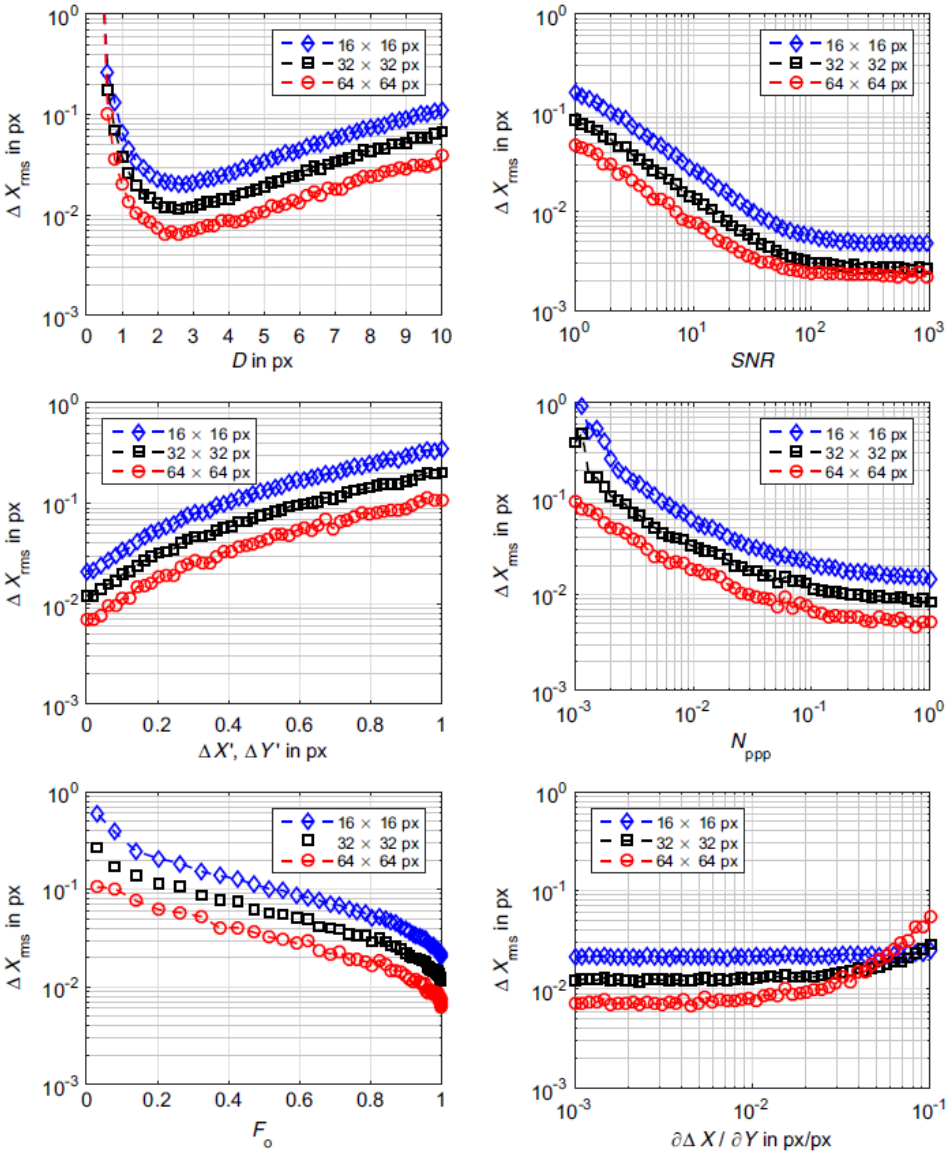


Figure 1.6. Effect of different parameters on the uncertainty of the estimated shift vector component $\Delta X$ (Scharnowski and Kähler 2016a)

PIV measurements also have the systematic uncertainties due to sources other than peak locking, e.g. change in camera angles, particle image density, interrogation window size in processing, etc. Figure 1.6 summarizes the effects of six parameters, namely particle image diameter ($D$), signal-to-noise ratio ($SNR$), fluctuations in particle image shift ($\Delta X'$, $\Delta Y'$), seeding density ($N_{PPP}$), out-of-plane loss-of-pairs ($F_o$) and displacement gradient ($\partial \Delta X / \partial Y$), on the random error of the estimated particle image shift (Scharnowski and Kähler 2016a). The systematic effect of such parameters on the total uncertainty of the measurements can be significant. Therefore, it is important to quantify the complete uncertainty (both random and systematic components) of flow measurements, and the contribution of the experimental factors to the uncertainty. In PIV, UQ methods have been proposed that are mainly focused on the random uncertainty, which can be retrieved from the data statistics. Approaches based on the error sampling method (Smith and Oberkampf 2014) or comparisons of different PIV measurements at the same locations (DeBonis et al. 2012) showed that PIV uncertainties are potentially significantly larger than those predicted by conventional PIV-UQ approaches because of the presence of systematic error sources. Hence, there is a need to develop a PIV-UQ approach where the significant experimental factors can be identified along with the systematic uncertainties arising from them. Moreover, the approach should be comprehensive in that it can be applied universally, irrespective of the kind of PIV setup, e.g. planar PIV, tomographic PTV, large scale PIV or microscopic PTV, for uncertainty quantification in any of the measured quantities, e.g. mean velocity or higher order statistics.

Finally, it is also observed that the background reflections in PIV images is a critical problem as the reflections produce high systematic errors in the vector field if they are not removed from the images. Figure 1.7 shows a raw image pair and the corresponding cross-correlation function in an interrogation window (Sciacchitano and Scarano 2014). As it can be seen in figure 1.7(a), the raw images are affected by strong laser light reflections, especially at the model's surface. The image interrogation by cross-correlation fails to return a valid peak that corresponds to the particle motion because of the presence of a self-correlation stripe in the correlation

map [figure 1.7(b)]. The problem of reflections removal is found to be not resolved especially in the case of unsteady reflections in a limited number of PIV recordings (insufficient for statistical convergence). Hence, it is highly significant to work on removing the reflections to minimize the uncertainty.

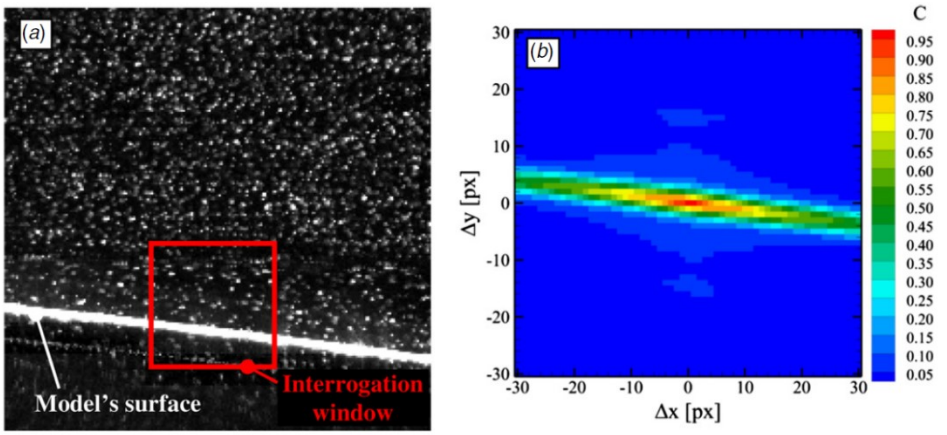


Figure 1.7. Raw image pair (left) and corresponding displacement field in chosen interrogation window (right) (Sciacchitano and Scarano 2014)

## 1.4. Thesis objectives

In summary, the present research aims at quantifying the total uncertainty of PIV data, i.e. labelling the quality of PIV results by devising a comprehensive framework for uncertainty quantification.

The specific objectives of the thesis are:

a) To conduct a survey among PIV researchers and users worldwide to know the significant PIV errors and UQ strategies

b) To quantify the systematic uncertainty due to peak-locking errors using a multi-$\Delta t$ approach which relies on image recordings with multiple inter-frame time separations $\Delta t$ and a least-squares regression of the measured quantities

c) To propose a comprehensive PIV-UQ framework based on Design of Experiments (DOE) and Analysis of Variances (ANOVA), where DOE allows to quantify the total uncertainty as well as the systematic uncertainties arising from various experimental factors by varying their levels in the measurements

d) To eliminate background reflections from PIV images, caused by the laser light impinging on solid surfaces

## 1.5. Thesis outline

The present chapter mainly describes the motivations behind the work along with the specific objectives of the thesis. Furthermore, an outline of the thesis is discussed briefly. The PIV technique and its various aspects are outlined in chapter 2. The error sources in PIV and the available PIV uncertainty quantification approaches are discussed in chapter 3. The survey on the PIV errors and uncertainties and its outcomes are presented in chapter 4. In chapter 5, an approach based on multiple $\Delta t$ acquisitions for peak-locking error correction and uncertainty quantification is explained. The results of the assessment of the approach for wind tunnel measurements of flow over a NACA0012 airfoil are also shown in that chapter. To analyze the significance of various experimental parameters and quantify the systematic uncertainties arising from them, a methodology based on statistical tools of DOE and ANOVA is proposed and explained in chapter 6. The methodology is experimentally assessed for planar PIV measurements of the flow over a NACA0012 airfoil in a wind tunnel. Moreover, the methodology is applied to a stereoscopic PIV experiment dealing with the flow at the outlet of a ducted Boundary Layer Ingesting (BLI) propulsor. The results of this application are also briefly shown in the chapter 6. An approach based on anisotropic diffusion to eliminate undesired background reflections from PIV images is introduced in chapter 7. The results of its application and comparison with conventional image pre-processing methods are also illustrated. Finally, chapter 8 presents a summary of the main results and conclusions.

# 1. Introduction

# Chapter 2
# Particle Image Velocimetry

## 2.1. Working principle

The PIV technique is based on the principle of measuring the fluid velocity by means of measuring the displacement of seeding particles dispersed in the fluid. The seeding particles are small enough to follow the fluid motion without altering the fluid and flow properties. The particles are illuminated twice with a small time gap by a light sheet generated from a light source, typically a pulsed laser. The light scattered by them is recorded by a digital imaging device, typically a CCD camera, placed perpendicular to the measurement plane. A typical setup of planar PIV measurements is shown in figure 2.1.

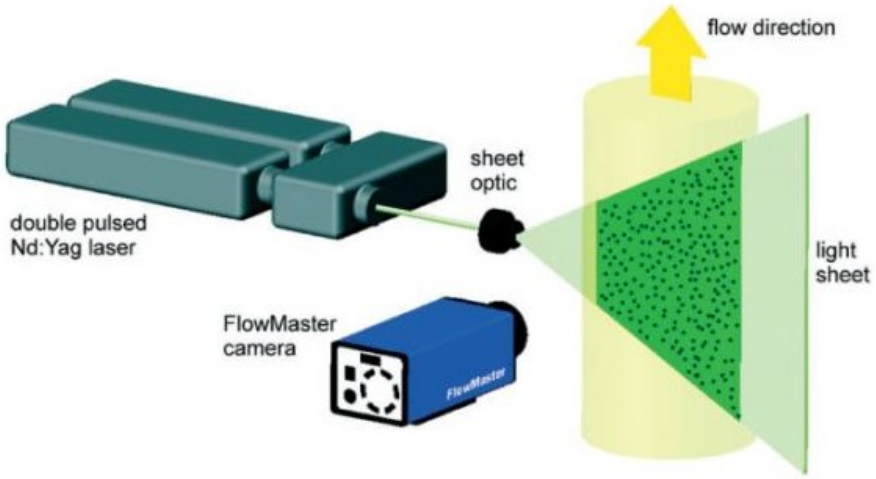


Figure 2.1. A typical set-up of planar PIV measurement system (www.lavision.de)

The planar measurements are referred to as two-dimensional-two-component (2D2C) measurements as they provide two components of velocity in a plane. By using two cameras capturing the same measurement plane from different angles, it is possible to estimate the third component (perpendicular to the measurement plane) of the velocity. This arrangement is known as Stereoscopic PIV system or 2D3C measurements (Prasad and Adrian 1993, among others) as shown in figure 2.2. Moreover, tomographic PIV enables to determine all three velocity components in three dimensional (3D3C) measurement domain (Elsinga et al. 2006) as shown in figure 2.3.

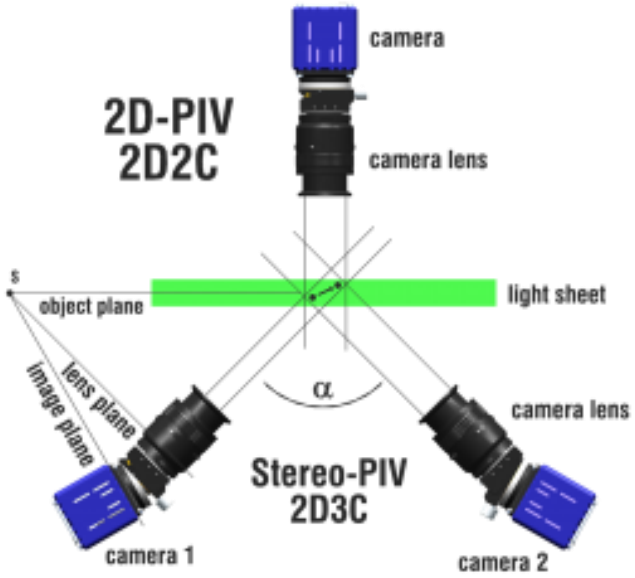


Figure 2.2. Experimental setup for single-camera 2D-PIV and dual camera stereoscopic PIV (Wieneke 2017)

The acquired images are typically analyzed on a digital computer with the help of image interrogation algorithms. The particle images are analyzed by cross correlation of the particle-image patterns in smaller interrogation windows or sub-domains. The estimated particle displacement is converted to the local fluid velocity by dividing it by the time interval between two light

pulses. The steps are repeated for the entire image to evaluate the instantaneous velocity in the chosen measurement plane in the fluid flow. Many advanced improvements and algorithms have been developed for higher accuracy and spatial resolution (Adrian and Westerweel 2011, Raffel et al. 2018, among others).

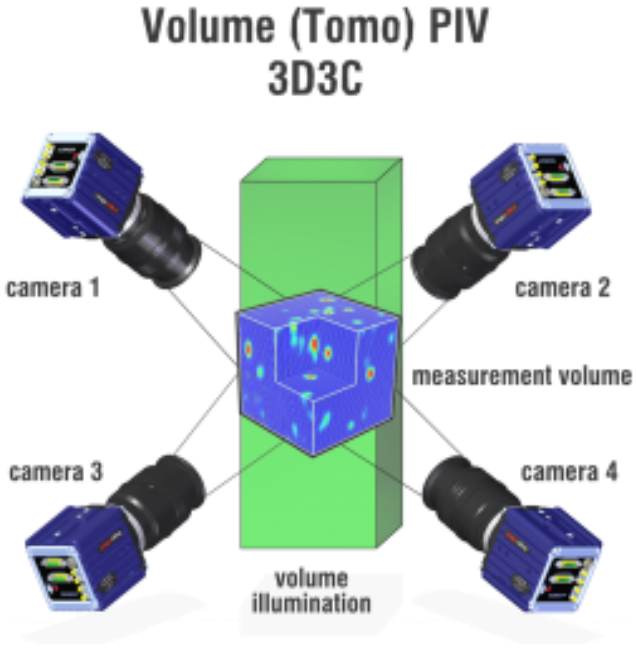


Figure 2.3. Experimental setup for volumetric tomographic PIV (Wieneke 2017)

## 2.2. Flow seeding

Small microscopic particles are used as seeding in fluid flows for PIV measurements. Ideally, the seeding particles are randomly distributed in the flow and carried along the flow without disturbing the flow properties. Therefore, choosing the correct seeding material is crucial and requires the knowledge of mechanical properties of small particles dispersed in the fluid flow. Moreover, scattering properties of the particles are important and the

particles are required to scatter enough light for their detection by the cameras.

### 2.2.1. Mechanical properties of seeding particles

Since the seeding particles in PIV are very small, they can be considered to be analogous to a sphere in a fluid in Stokes flow regime (Melling 1997). The slip velocity $V_s$ of a particle of diameter $d_p$ can be given by (Raffel et al. 2018):

$$V_s = V_p - V_f = d_p^2 \frac{(\rho_p - \rho_f)}{18\mu} \frac{dV_p}{dt} \tag{2.1}$$

where, $V_p$ and $V_f$ are the particle velocity and fluid velocity, respectively, $\rho_p$ and $\rho_f$ are the particle density and fluid density, respectively, and $\mu$ is the dynamic viscosity of the fluid. Equation (2.1) shows that the condition for neutrally buoyant particles $(\rho_p - \rho_f)/\rho_f \ll 1$ allows the particles to follow the flow perfectly i.e. the slip velocity $V_s$ to be zero. Though this condition can be easily achieved in liquid flows, it cannot be fulfilled in gas flows, where $\rho_p/\rho_f = O(10^3)$.

The term relaxation time $\tau_p$ can be used to estimate whether the seeding particles follow the flow accurately or not. It is defined as the response time of the particle to a sudden change in the fluid velocity. From equation (2.1) the relaxation time for the particle of diameter $d_p$ can be given by:

$$\tau_p = d_p^2 \frac{(\rho_p - \rho_f)}{18\mu} \tag{2.2}$$

For the particle to follow the flow accurately, the relaxation time should be low. Since the value of relaxation time depends on the values of the particle diameter and density, the condition can be achieved by small particle diameter or by having the particle density very similar to that of the fluid. In turbulent flows, the capability of seeding particles to follow the flow is estimated by the particles' Stokes number $S_k$. It is calculated as the ratio of relaxation time $\tau_p$ to characteristic flow time scale $\tau_f$,

$$S_k = \frac{\tau_p}{\tau_f} \tag{2.3}$$

The particles' Stokes number should be less than 0.1 for the particles to follow the flow accurately (Samimy and Lele 1991).

For gas flows, seeding particles with small diameters of the order of 1 μm are usually chosen for good flow tracking capability. As shown in table 2.1 (Sciacchitano 2014), the common materials for the seeding particles in gas flows are titanium dioxide ($TiO_2$), alumina ($Al_2O_3$), glass, olive oil and di-ethyl-hexyl-sebacate (DEHS). The particle response times achieved are in the range of 1 μs to 20 μs. For large scale flows with large field of view, helium filled soap bubbles are used due to the possibility of having larger seeding particles of diameter of around 1mm (Bosbach et al. 2009).

Table 2.1. Typical seeding particles for gas flows (Sciacchitano 2014)

| Material | $\rho_p$ [kg/m³] | $d_p$ [μm] | $\tau_p$ [μs] | Reference |
|---|---|---|---|---|
| $TiO_2$ | 4230 | 0.01 – 0.5 | 0.4 – 3.7 | Ragni et al. (2011) |
| $Al_2O_3$ | 4000 | 0.3 | 20 – 28 | Urban and Mungal (2001) |
| Glass | 2600 | 1.67 | 22.6 | Melling (1997) |
| Olive oil | 970 | 3 | 22.5 | Melling (1997) |
| DEHS | 912 | 1 | 2 | Ragni et al. (2011)<br>Kähler et al. (2002) |

### 2.2.2. Scattering properties of seeding particles

As described in the previous section, the seeding particles are required to follow the flow. Moreover, the particles should scatter enough light so that they are present in the PIV images. The intensity of light scattered by the

seeding particles depends on the ratio of particles' refractive index to that of the fluid; on the particles' size, shape and orientation; and on polarization and observation angles (Raffel et al. 2018). For spherical particles of diameters $d_p$ larger than the wavelength λ of incident light, Mie's scattering theory applies (Mie 1908). Following Mie's theory, the scattering can be characterized by normalized diameter $q$:

$$q = \frac{\pi d_p}{\lambda} \tag{2.4}$$

If $q$ is larger than unity, approximately $q$ local maxima appear in the angular distribution from 0° to 180° as shown in figure 2.4 (Raffel et al. 2018). For increasing $q$, the ratio of forward to backward scattering increases rapidly. Therefore, it is advantageous to record in the forward scatter. However, recording in the forward scatter is limited due to limited depth of field and limited optical access. Therefore recording is mostly done from the sides.

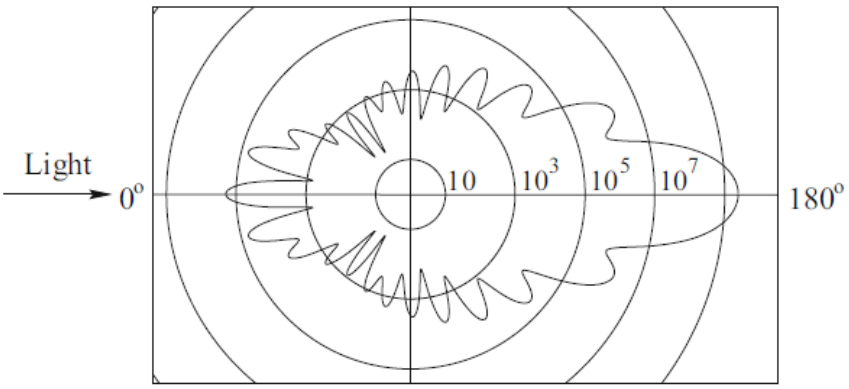


Figure 2.4. Light scattering by a 1 μm oil particle in air (Raffel et al. 2018)

According to Mie's theory, the scattering signal increases with increase in the particles' diameter. Therefore, larger particles are suitable as the seeding particles to achieve higher signal. Moreover, the materials with high index of refraction are preferred as the scattering efficiency increases with increase in the ratio between particle and fluid refractive indices.

## 2.3. Illumination

In PIV, the seeding particles need to be illuminated and imaged twice with a certain time gap $\Delta t$. The duration of illumination, called pulse duration $\delta t$, should be short. The particle images should not appear as streaks but as circular dots. This can be achieved if the particle image displacement during the illumination i.e. for time $\delta t$ is very small compared to the particle image size:

$$\delta t \ll \frac{d_\tau}{MV_p} \tag{2.5}$$

where, $d_\tau$, $M$ and $V_p$ are the particle image diameter, optical magnification factor and particle velocity, respectively.

The seeding particles are captured on a two-dimensional image from a three-dimensional field. Therefore, only the particles from a very small slice of the three-dimensional domain need to be illuminated when one is interested in two-dimensional measurements of the flow field. This is possible with the help of a thin light sheet illuminating the seeding particles in small slice. The thin light sheet is achieved with the help of optics consisting of cylindrical and/or spherical lenses as shown in figure 2.5.

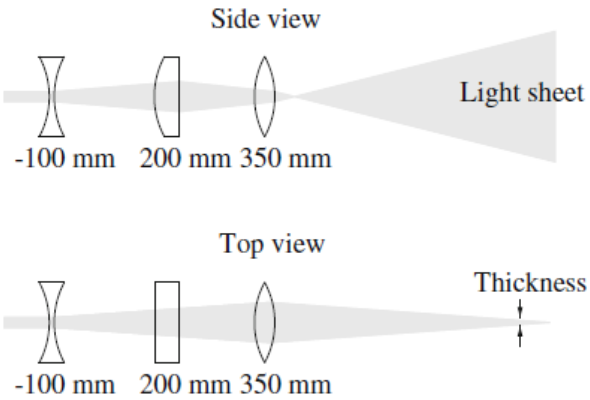


Figure 2.5. Light sheet optics using two spherical lenses (one of them with negative focal length) and one cylindrical lens (Raffel et al. 2018)

Lasers are the most widely used illumination sources for PIV experiments as they emit monochromatic light with high energy density that can be shaped into a thin light sheet using the lenses. The lasers commonly used in PIV measurements are pulsed Q-switched solid state Nd:YAG and Nd:YLF. The Nd:YAG lasers can emit light with a wavelength of 532 nm with a pulse duration of 5 ns to 10 ns and pulse energy between 10 mJ and 1 J. The repetition rates achievable with these lasers are only up to 50 Hz. Therefore, for high-speed flows Nd:YLF lasers are usually employed as they have higher repetition rate of 1 to 10 kHz. They produce light of 527 nm wavelength with pulse energy between 10 and 60 mJ.

## 2.4. Imaging

In PIV, the particle images are acquired by an imaging system consisting of camera and optical lenses. The imaging system is characterized by its focal length ($f$), f-stop or f-number ($f_\#$) and optical magnification factor ($M$) as given by:

$$\frac{1}{f} = \frac{1}{d_i} + \frac{1}{d_o} \ , \qquad f_\# = \frac{f}{D} \ , \qquad M = \frac{d_i}{d_o} \tag{2.6}$$

where, $d_i$, $d_o$ and $D$ are image distance i.e. the distance between lens and image plane, object distance i.e. the distance between lens and object plane, and the lens aperture diameter, respectively. Furthermore, the magnification factor M can also be given by the ratio of image size to the object size or field of view ($FOV$):

$$M = \frac{pixel\ size \times number\ of\ pixels\ in\ the\ sensor}{FOV} \tag{2.7}$$

Therefore, by following geometric optics, the geometrical diameter of particle images of the particles of diameter $d_p$ is:

$$d_{geom} = M d_p \tag{2.8}$$

According to Fraunhofer diffraction theory, the particles imaged by an aberration-free lens do not appear as point images but rather spread over a small spot known as Airy disc (Hecht 2002). The particle image diameter due to the diffraction effect is given by (Raffel et al. 2018):

$$d_{diff} = 2.44 f_{\#}(M+1)\lambda \tag{2.9}$$

In practice, for PIV images, the light distribution in the Airy disc is approximated by a Gaussian intensity distribution with $e^{-2}$ diameter of $0.74\,d_{diff}$ as shown in figure 2.6.

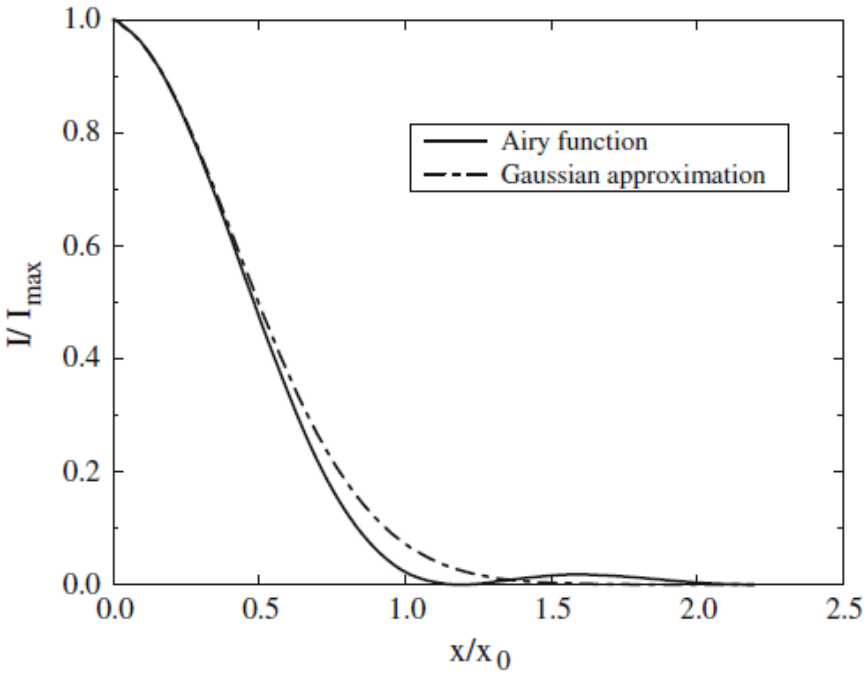


Figure 2.6. Normalized intensity distribution of Airy pattern and its approximation by a Gaussian curve (Raffel et al. 2018)

If the lens aberrations are assumed to be negligible, then the resulting particle image diameter is given by:

$$d_\tau = \sqrt{d_{geom}^2 + d_{diff}^2} \tag{2.10}$$

In presence of lens aberrations, the particle image diameter can be different from that estimated with the above formula. Refer to Raffel et al. (2018) for detailed description of the effect of lens aberrations on imaging the small particles. Moreover, equation (2.10) is valid only for the particles in focus i.e. the particles falling within the depth of field. The focal depth of field $\delta_z$ of the optical system can be given by (Raffel et al. 2018):

$$\delta_z = 4.88 f_\#^2 \lambda (M+1)^2 / M^2 \tag{2.11}$$

The focal depth represents the region in which the particles are in focus. The focal depth should be at least equal to the thickness of laser sheet in order to minimize the background noise by out-of-focus particles.

## 2.5. Image recording

In early days, PIV measurements were employed with photographic films to record the images. In order to record the images at two time instances, the shutter of photographic camera was opened twice during two light pulses. That resulted into a single PIV image consisting of the particle images at two time instances, known as single-frame-double-exposure, which caused difficulty in identifying the direction of flow. Another limitation of the photographic recording was that the unavailability of images during the recording phase. The images were only available and viewed after photochemical processing of the photographic films. Figure 2.7(a) shows an example of the image recorded by photographic film.

Due to the limitations of the photographic recording for PIV experiments, it is replaced by digital image recording using image sensors: charge couple device (CCD) and complementary metal oxide semiconductor (CMOS). Both sensor types consist of pixels i.e. the array of sensitive elements which convert the incoming light photons into electric charge. The electric charge is finally converted to the digital signals as various intensity levels in digital

images (Falchi and Romano 2009). CCD sensors have limited number of output nodes which results into their limited repetition rate of about 10 Hz (Hain et al. 2007). Contrary, in case of CMOS sensors, each pixel has individual output leading to high acquisition frequency up to 10 kHz. However, they have lower fill factor (ratio of optically sensitive area to the total area of pixel, Raffel at al. 2018) compared to the CCD sensors. Therefore, CMOS sensors have larger pixel size of 10 to 20 μm against 5 to 7 μm of CCD sensors in order to increase light sensitivity. Figure 2.7(b) shows an example of the image captured by CMOS camera.

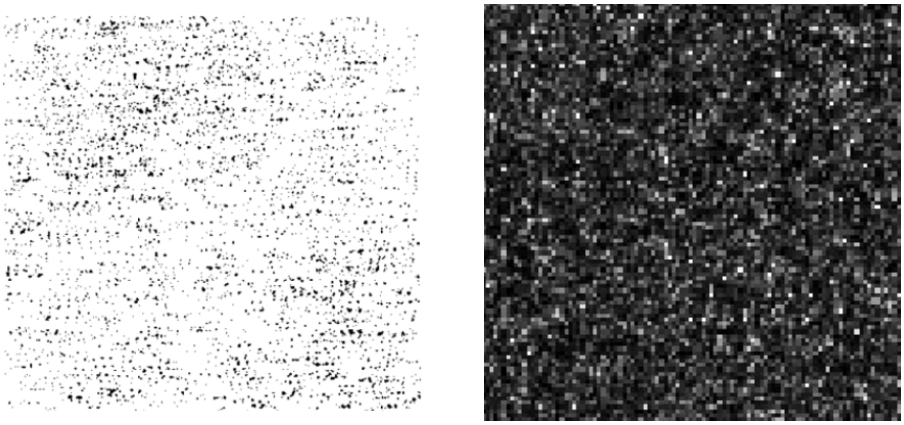

(a) (b)

Figure 2.7. (a) an example of image captured by photographic recording taken from Adrian (1991), the grey levels have been inverted; (b) an example of image captured by CMOS camera

Recent developments in image sensors have provided scientific CMOS (sCMOS) sensors with better image quality and system performance. They are suitable for PIV experiments with limited laser power or low contrast between particles and background to get better quality images. They have resolution of about 5 mega pixels with low readout noise and high frame rates.

## 2.6. Evaluation of images

The major steps in evaluating the particle images are:

a) **Division of image into interrogation windows:**
The image is divided into small cells or windows such that each of them contain enough number of particle images (around 10) for analysis. The interrogation windows are usually of size 16 × 16 pixels to 128 × 128 pixels. Each interrogation window from the first image is analyzed with respect to the corresponding window of the second image to estimate a local velocity vector for that window.

b) **Cross-correlation analysis:**
A discrete cross-correlation function is computed between the two corresponding interrogation windows of the pair of images. It results into a cross-correlation map, where the position of peak relative to origin gives the average displacement of the particles in that interrogation window. The normalized cross-correlation function $C$ for two interrogation windows $I_1(x, y, t)$ and $I_2(x, y, t+\Delta t)$ of size $I \times J$ pixels from the two images captured at $t$ and $t+\Delta t$ is given by (Huang et al. 1997):

$$C(m,n) = \frac{\sum_{i=1}^{I}\sum_{j=1}^{J}[I_1(i,j) - \overline{I_1}] \cdot [I_2(i+m, j+n) - \overline{I_2}]}{\sqrt{\sum_{i=1}^{I}\sum_{j=1}^{J}[I_1(i,j) - \overline{I_1}]^2 \cdot [I_2(i+m, j+n) - \overline{I_2}]^2}} \tag{2.12}$$

where, $\overline{I_1}$ and $\overline{I_2}$ are the spatial averages within the interrogation windows of $I_1$ and $I_2$, respectively. Equation (2.12) is known as direct cross-correlation. The convolution theorem (De Groot 1989) in combination with fast Fourier transform (Raffel et al. 2018) are more efficient ways to obtain the cross-correlation function.

c) **Estimation of fractional displacement:**
The position of the highest peak in cross-correlation map corresponds to the particle image displacement. Therefore, the displacement or the particle image shift is computed as an integer

value in pixels. For more accurate estimation of the particle image shift, peak interpolation is necessary. Various peak-fitting algorithms have been proposed, like centre of mass method, parabolic fit and Gaussian fit (Raffel et al. 2018). The Gaussian peak fit for horizontal displacement is given by (Willert and Gharib 1991):

$$\Delta x = i + \frac{\ln C(i-1,j) - \ln C(i+1,j)}{2[\ln C(i-1,j) + \ln C(i+1,j) - 2\ln C(i,j)]} \tag{2.13}$$

where, $(i, j)$ is the discrete position of the peak of cross-correlation function. Since the particle image shape is approximated to Gaussian, the Gaussian peak-fitting is more accurate than the other types of fittings (Raffel et al. 2018).

d) **Conversion from pixels to physical units:**

The computed particle image shift or displacement is in pixels. The velocity in physical units (e.g. m/s) is obtained by dividing it by the time separation between the laser pulses $\Delta t$ and magnification factor $M$ calculated using equation (2.7) and then multiplying by the pixel size of the image sensor $s$:

$$u = \frac{\Delta x \cdot s}{\Delta t \cdot M} \tag{2.14}$$

where, $u$ and $\Delta x$ are the horizontal velocity in physical units and particle image displacement in pixels, respectively.

It is to be noted that nowadays, more advanced algorithms consisting of multiple passes and window deformation are used for evaluation of images Some of the velocity fields computed by PIV are shown in figure 2.8.

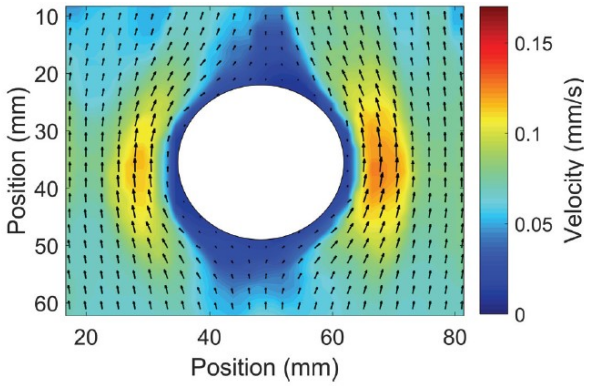


(a)

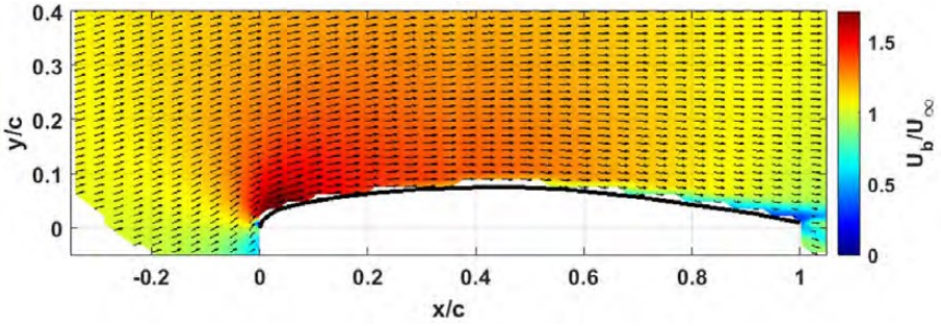


(b)

Figure 2.8. Examples of PIV velocity fields: (a) flow around a cylinder in a Hele-Shaw cell (Kislaya et al. 2018), (b) flow over a high-lift airfoil (Faleiros et al. 2019)

# Chapter 3
# PIV Errors and Uncertainty

## 3.1. Definitions and classification of measurement errors

Measurement error is defined as the difference between the measured value and the true value of a quantity. For a measured quantity $X$, the error δ with respect to it true value $X_{true}$ is:

$$\delta = X - X_{true} \tag{3.1}$$

The measurement errors are classified into two components, namely systematic (or bias) error and random error (ISO-GUM 2018):

$$\delta = \beta + \varepsilon \tag{3.2}$$

where, β and ε are the systematic and random errors, respectively. The systematic or bias errors are constant and do not vary during all the measurements (Coleman and Steele 2009). However, in the PIV community, the systematic errors are considered to be fixed or relatively fixed function of their sources (Smith and Oberkampf 2014). Conversely, the random errors are not constant and usually change their values during the measurements.

Figure 3.1 shows the effect of errors on successive measurements of a quantity $X$. For measurement $X_1$, the difference between the measured value and the true value is the total error $\delta_{X_1}$. As per equation (3.2), the total error is the sum of systematic error β and random error $\varepsilon_1$. As the random error is not the same for all measurements, different value of the total error $\delta_{X_2}$ can be seen for another measurement $X_2$ in figure 3.1.

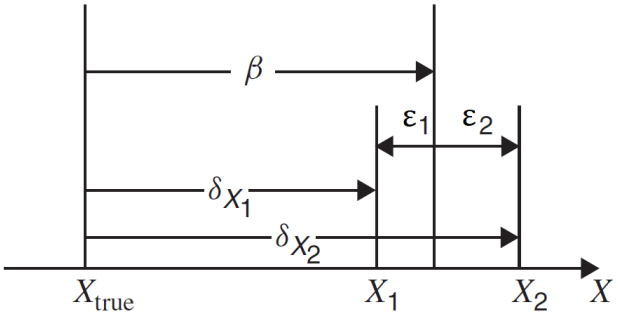


Figure 3.1. Effect of errors on successive measurements of a quantity $X$ (Coleman and Steele 2009)

## 3.2. Definitions and classification of measurement uncertainties

Measurement uncertainty is defined as an interval which is likely to contain, with a given confidence level, the magnitude of total measurement error. Figure 3.1, where two measured values of $X$ are shown, can be extended to plot distribution of the measured values from $N$ number of measurements as shown in figure 3.2(a).

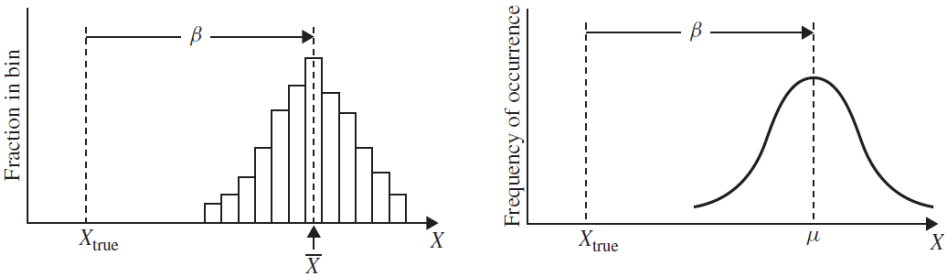


(a) (b)

Figure 3.2. Successive measurements of a quantity X: (a) sample population distribution and (b) parent population distribution (Coleman and Steele 2009)

This distribution of sample population of $N$ measured values of $X$ is characterized by a higher number of measured values near the mean $\bar{X}$ and

lower number of measured values away from the mean $\bar{X}$. As the number of measurements approached infinity, the distribution of sample population approaches to that of the parent population shown in figure 3.2(b). The mean of the parent population μ becomes the true value $X_{true}$ in the absence of systematic errors i.e. when $\beta = 0$.

Measurement uncertainties are of two types- systematic and random based on the type of error source they arise from i.e. systematic or random error source, respectively. Following ISO-GUM (2018), a standard uncertainty is defined as an estimate of the standard deviation of the parent population from which a particular elemental error originates. The total standard uncertainty $u_X$ is given by the sum of squares of the systematic standard uncertainty $b_X$ and random standard uncertainty $r_X$ (Coleman and Steele 2009):

$$u_X = \sqrt{b_X^2 + r_X^2} \tag{3.3}$$

In the estimation of uncertainty, it is necessary to specify some range ($X_{best} \pm u_X$) within which $X_{true}$ might lie. However, no probability can be associated with this range while using the standard $u_X$ uncertainty for it. Therefore, an expanded uncertainty $U_X$ is required to state that $X_{true}$ lies within the interval ($X_{best} \pm U_X$) with certain confidence. Here, $X_{best}$ is the best estimate of $X_{true}$ and assumed to be equal to the mean $\bar{X}$ of the $N$ number of measurements.

The expanded uncertainty is calculated from the standard uncertainty by multiplying it with a coverage factor k:

$$U_X = k u_X \tag{3.4}$$

The coverage factor is determined based on the error distribution. The error distribution is assumed to be Gaussian for most of the experimental data. The coverage factors of 1,2 and 3 in Gaussian distribution lead to 68%, 95% and 99.7% confidence levels, respectively.

## 3.3. Error sources in PIV

PIV measurements are characterized by different stages of the measurement chain, like experimental setup, image acquisition, velocity estimation and data reduction. All these stages might introduce errors as shown in figure 3.3 (Sciacchitano 2019).

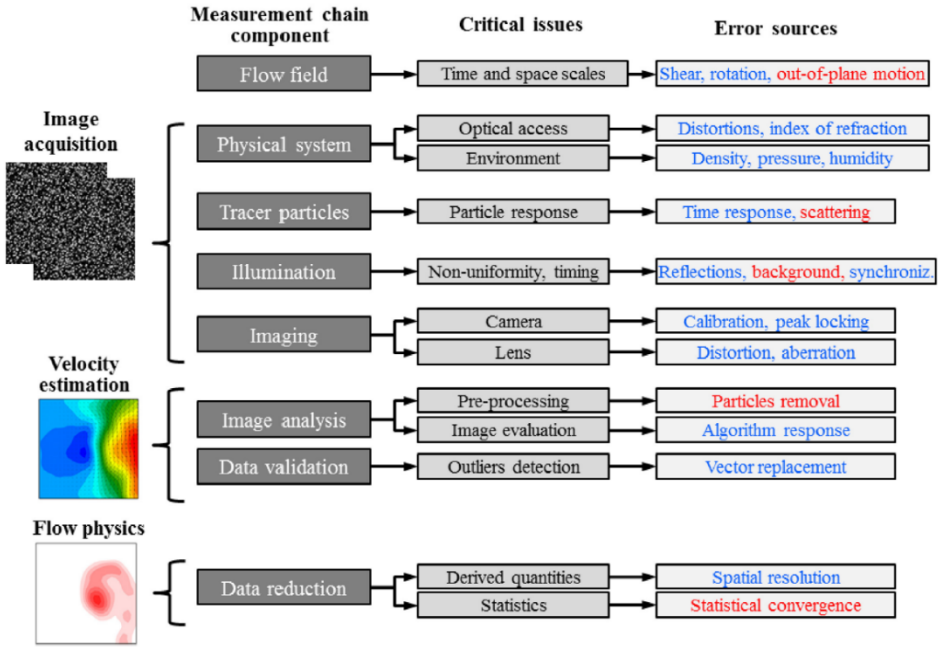


Figure 3.3. Major stages of PIV measurement chain and the relevant error sources; error sources indicated in blue and red are mainly systematic and mainly random, respectively (Sciacchitano 2019)

The errors in PIV measurements can be categorized into errors caused by system components, errors due to the flow itself and errors related to the evaluation technique (Raffel et al. 2018).

### 3.3.1. Errors caused by system components

#### 3.3.1.1. Errors related to installation and alignment

In planar (2D2C) PIV measurements, if the laser sheet or measurement plane is not aligned properly with the desired plane in the flow field, then the velocity components retrieved from the evaluation do not correspond to the true velocity components. This introduces a systematic error in the results (Discetti and Adrian 2012, Raffel et al. 2018, among others). Moreover, in presence of significant out-of-plane motion of particles, perspective errors are introduced. The magnitude of perspective error increases with increasing distance from the optical axis of camera lens as shown in figure 3.4 (Raffel et al. 2018). These errors can be reduced by decreasing the observation angle α (i.e. by increasing the distance between the image plane and measurement plane or by reducing the field of view), by using telecentric lenses (Konrath and Schöder 2002) or by acquiring the images in stereoscopic configuration with two cameras (Prasad 2000).

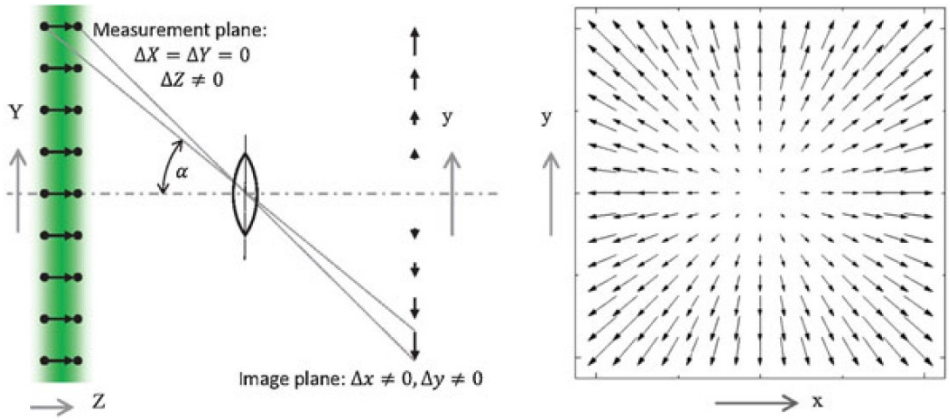


Figure 3.4. Illustration of the perspective error for a constant out-of-plane particle motion ($\Delta Z \neq 0$) and zero in-plane motion ($\Delta X = \Delta Y = 0$)

Furthermore, the errors during calibration process can be significant if the calibration plate does not align perfectly with the measurement plane or the calibration plate itself has manufacturing defects. The calibration errors can

also occur if the laser sheet is thick and the distance between image plane and measurement plane is relatively short. The magnification, in this case, can vary drastically across the laser sheet thickness introducing errors in the flow velocity estimation (Raffel et al. 2018).

#### 3.3.1.2. Timing and synchronization errors

The measurement errors are introduced when the value of time gap $\Delta t$ between two light pulses deviates from the selected value by the experimenter. This can be caused by different cable lengths used to trigger the system components or change in the firing order of the laser oscillators of double-pulsed laser when the oscillators are not identical (Raffel et al. 2018). To detect and correct these timing errors in PIV measurements of the flows with large Mach numbers or the measurements with large magnification (in microfluidics), it is recommended to use a fast diode to monitor the exact pulse delay with an oscilloscope.

#### 3.3.1.3. Illumination errors

Errors can be introduced when the two laser pulses are not aligned perfectly or when they have different intensity profiles. That can lead to variation in the intensities of particle images (Nobach and Bodenschatz 2009, Nobach 2011). Since the cross-correlation operator is insensitive to absolute intensity variations in the images, the slight variation in the intensities of two light pulses or slight spatial intensity variation along the light sheet do not cause the measurement errors (Wieneke 2017). Nevertheless, it is important that the illumination system provides sufficient light intensity in order to have enough contrast between the background and seeding particles in the images (Scharnowski and Kähler 2016b).

#### 3.3.1.4. Imaging errors

Peak-locking is one of the most significant error sources in PIV measurements (Westerweel 1997, Christensen 2004, Overmars et al. 2010, among others). It usually occurs when the particle image diameter is very

small (less than one pixel) which causes the measured displacement to be biased to the nearest integer value. The measured displacement is therefore underestimated or overestimated based on the amount of sub-pixel displacement. The magnitude of peak-locking error depends on the algorithm used for fitting cross-correlation peak (Roesgen 2003). The peak-locking errors have a significant effect on the estimation of turbulence statistics accurately (Christensen 2004). Various approaches have been proposed to minimize or correct the peak-locking errors, such as using smaller optical aperture or higher f-stop ($f_{\#}$), image defocussing (Overmars et al. 2010), optical diffusers (Michaelis et al. 2016, Kislaya and Sciacchitano 2018), multi-$\Delta t$ acquisition (Nogueira et al. 2009, 2011, Legrand et al. 2012, 2018) and data post-processing approaches (Roth and Katz 2001, Hearst and Ganapathisubramani 2015, Michaelis et al. 2016).

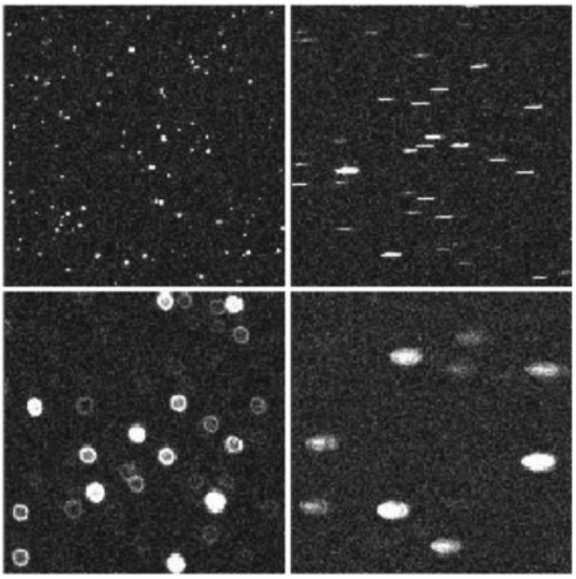

Figure 3.5. Effect of optical aberrations and out-of-focus imaging; where the upper left image shows the ideal imaging conditions (focused particle images without strong optical aberrations), the lower left image illustrates out-of-focus particle images and the right column reveals the effect of astigmatic aberrations superimposed on the focused (upper image) and unfocused particle images (lower image) (Raffel et al. 2018)

Image noise can also cause errors in imaging the seeding particles. It affects the performance of image evaluation algorithms in measuring the particle image displacements. Digital cameras are characterized by three types of noise sources, namely background noise, photon noise and device noise (Adrian and Wesrerweel 2011). Optical elements between the flow and imaging system, such as glass window, can cause optical aberrations which introduce errors in the measurements. The image distortions (see figure 3.5) can also be introduced by the imaging system itself if the field of view is large and the distance between image plane and measurement plane is small (Raffel et al. 2018).

### 3.3.2. Errors due to the flow

The flow features usually also have an effect on the accuracy of PIV measurements. Flow fluctuations, velocity gradients and streamline curvatures might cause measurement errors due to the particle slip or due to the failure of image processing algorithms to estimate the velocity field correctly in presence of these flow features (Sciacchitano 2019). The effect of in-plane velocity gradients on the velocity estimation can be minimized by state-of-the-art algorithms with window deformation (Scarano and Riethmuller 2000). However, due to the finite number of particles in the interrogation windows, the out-of-plane velocity gradients affect the accuracy of measuring the in-plane velocity components. Moreover, the variations in the fluid properties, like temperature, density, viscosity, or in the Reynolds and Mach numbers during the course of experimental tests cause additional errors in the measurements. The seeding particles entering or leaving the light sheet (in-plane and/or out-of-plane motion of particles) can produce background noise in the correlation function as they are not matched with the other particles. Also, the particles present at different depths across the light sheet can produce overlapping particle images causing the random errors in the measurements (Nobach and Bodenschatz 2009, Nobach 2011). For microscopic PIV measurements of very low velocity flows (less than 1mm/s), measurement errors are introduced due to Brownian motion of the seeding particles (Olsen and Adrian 2001). Such

an error increases with increase in the fluid temperature and decreases with increase in particle diameter and flow velocity (Devasenathipathy et al. 2003)

### 3.3.3. Errors related to the evaluation technique

The errors related to image evaluation techniques and processing parameters have been analyzed in details as can be seen in the international PIV challenges (Stanislas et al. 2003, 2005, 2008, Kähler et al. 2016). In the early days of PIV, major attention was on detection and removal of outliers i.e. the wrong vectors from the estimated velocity field (Keane and Adrian 1990, Westerweel and Scarano 2005). Though it is relatively easy to detect and remove the isolated outliers, the problem of clusters of outliers still need more attention (Masullo and Theunissen 2016). From the end of 1990s, the research has been focused on minimization of uncertainty and maximization of spatial resolution in the development of PIV algorithms (Sciacchitano 2019). The researchers have assessed the effectiveness of various PIV evaluation algorithms based on correlation analysis, interrogation window sizes and shapes, cross-correlation peak-fitting, vector interpolation schemes, etc.

## 3.4. PIV uncertainty quantification

In PIV, the local flow velocity $u$ is computed by estimating the displacement $\Delta x$ of particle images within a short time step $\Delta t$ (Adrian and Westerweel 2011):

$$u = \frac{\Delta x}{\Delta t} = \frac{\Delta X}{M \Delta t} \tag{3.5}$$

where, $\Delta X$ is the displacement in the object plane and $M$ is the magnification factor of imaging system. The uncertainty of the velocity is estimated by Taylor's series method (Coleman and Steele 2009), considering $\Delta X$, $\Delta t$ and $M$ as independent variables:

$$\left(\frac{U_u}{u}\right)^2 = \left(\frac{U_{\Delta X}}{\Delta X}\right)^2 + \left(\frac{U_{\Delta t}}{\Delta t}\right)^2 + \left(\frac{U_M}{M}\right)^2 \tag{3.6}$$

The uncertainty of laser pulse separation $U_{\Delta t}$ is considered as a Type B uncertainty i.e. it cannot be evaluated from data statistics of repeated measurements. Its value is usually provided by the manufacturer. Whereas, the work on quantification of uncertainty of the magnification factor $U_M$ is limited. Gui et al. (2001) estimated the magnification uncertainty based on the uncertainties of the sizes of field of view in the object plane and image plane. The magnification uncertainty has also been calculated based on the uncertainties of position and size of dots on the calibration plate, image distortion due to perspective errors, the misalignment between calibration plate and measurement plane and the misalignment between calibration plate and image plane (Campagnole dos Santos et al. 2018). When the calibration procedure is performed properly, the magnification and calibration uncertainties are negligible. Therefore, the uncertainty of displacement $U_{\Delta X}$ is a dominant term in equation (3.6) and most of the PIV uncertainty quantification (UQ) approaches focus on estimating $U_{\Delta X}$. These PIV-UQ approaches are classified as a-priori and a-posteriori approaches (Sciacchitano et al. 2013). A-priori approaches provide a general value of uncertainty using theoretical modelling of the measurement chain or numerical and experimental assessment with synthetic images. Conversely, a-posteriori approaches provide the uncertainty of instantaneous or averaged velocity field by analyzing the measured data (Sciacchitano 2019).

### 3.4.1. A-priori uncertainty quantification approaches

A-priori approaches have been proposed in the early days for PIV-UQ. Such approaches are mostly based on the theoretical modelling of the measurement chain and/or Monte Carlo simulations using synthetic images.

#### 3.4.1.1. A-priori uncertainty quantification by theoretical modelling

In the earliest days of PIV, Adrian (1986) proposed to quantify the uncertainty of measured particle image displacement as $cd_\tau$, where $d_\tau$ is the

particle image diameter and $c$ is a parameter related to the uncertainty in detecting particle image centroid. The particle image diameter can be computed a-priori by analytical formula or a-posteriori from auto-correlation function (Adrian and Westerweel 2011). The typical values of $c$ are in the order of 0.1. However, this approach is very simplistic and does not account for the errors like peak locking which is evident for small particle image sizes. Moreover, the approach does not take into account the effect of flow conditions, like velocity gradients, out-of-plane motion, streamline curvature and imaging conditions. The approaches based on theoretical models are mostly based on simplified assumptions of the flow conditions and image evaluation and are, therefore, limited to provide actual uncertainty values.

#### 3.4.1.2. A-priori uncertainty quantification by numerical or experimental assessment

Since the approaches based on theoretical models use simplified assumptions and do not consider the experimental complexity and image evaluation, many researchers employed numerical or experimental assessment to quantify the uncertainty a-priori. The approaches of numerical simulations (Monte Carlo) use synthetic images which are generated with random distribution of seeding particles and with a known motion. The synthetic images are advantageous for the analysis as the true velocity field is known beforehand, the values of experimental parameters can be modified easily without affecting the other parameters as well as their values can be set to the values not easily achievable in the real experiments (e.g. low or high turbulence levels). The synthetic images and Monte Carlo simulations have been used very often for a-priori PIV-UQ and analysis due to these advantages. The measurement errors have been characterized for different evaluation algorithms in PIV as a function of parameters, like particle image size and displacement, displacement gradient, seeding density, out-of-plane particle motion, image interpolation algorithm, cross-correlation peak fit algorithm (Sciacchitano 2019). However, the synthetic images are known to yield low measurement errors due to ideal imaging and

flow conditions. Therefore, experimental assessments have been proposed which better represent the conditions of real experiments. For such assessments, the measurement error is computed by comparing the measured velocity field to the true velocity field. The true velocity field is either imposed or quantified via a more accurate measurement system (Sciacchitano 2019). The measurement errors from the experimental assessments are found to be large, especially in presence of severe out-of-plane motion, peak locking, under resolved length scales and low image quality. Moreover, the human factor is also significant in the PIV measurements as the values of different experimental parameters are chosen based on personal experience (Kähler et al. 2016).

### 3.4.2. A-posteriori uncertainty quantification approaches

In PIV, as the measurement errors depend on several factors throughout the measurement chain and they might vary in space and time, the errors and uncertainties are not uniform within the measured flow field. Therefore, a-posteriori uncertainty quantification is necessary where the local uncertainty of each velocity vector can be quantified (Sciacchitano 2019). Various a-posteriori UQ approaches have been proposed for PIV measurements. Following Bhattacharya et al. (2018), these approaches are classified into indirect and direct methods. The indirect methods make use of information pre-calculated from calibration, whereas the direct methods estimate the uncertainty directly from the measured velocity field. Some of the commonly used indirect methods, namely uncertainty surface method (Timmins et al. 2012) and cross-correlation peak ratio criterion (Charonko and Vlachos 2013), and direct methods, namely particle disparity method (Sciacchitano et al. 2013) and correlation statistics approach (Wieneke 2015) are discussed briefly in the following sections.

#### 3.4.2.1. Uncertainty surface method

The uncertainty surface method (Timmins et al. 2012) was the first a-posteriori approach for PIV-UQ to quantify instantaneous uncertainty of each velocity vector. In this approach, it is required to identify major error

sources in the experiment. Timmins et al (2012) considered four sources, namely particle image diameter, seeding density, shear rate and particle image displacement. Synthetic images are then generated by varying the values of these chosen parameters and the images are analyzed by PIV evaluation algorithms. The computed velocity fields are compared with the known true velocity fields to determine the error distributions as a function of the selected parameters and generate an uncertainty surface. The experimental PIV images are analyzed using the generated uncertainty surface to compute the uncertainty bounds for each velocity vector. The working principle of the method is shown schematically in figure 3.6.

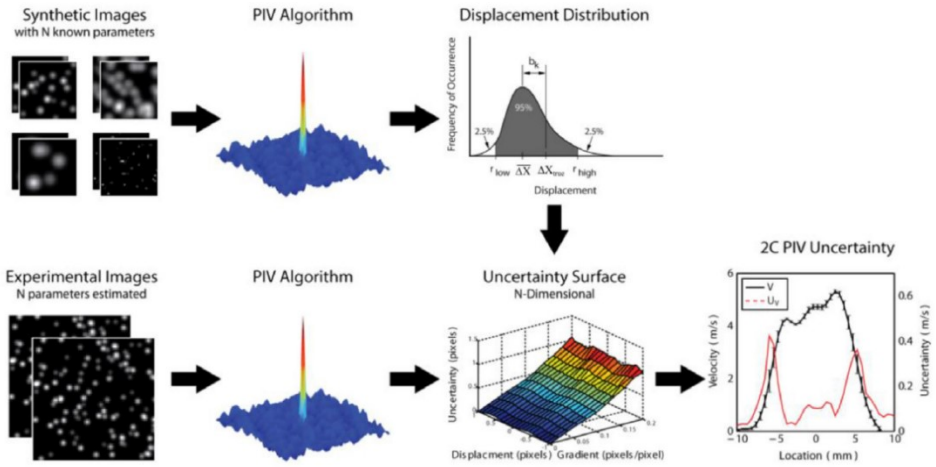


Figure 3.6. Schematic representation of the working principle of the uncertainty surface method (Sciacchitano 2019)

The uncertainty surface method determines the error distributions without any assumption of their shape and can distinguish systematic and random uncertainty components. However, the method relies on selection of the major error sources and estimation of their values, which are also affected by the measurement uncertainty. Moreover, generation of the uncertainty surface is time consuming and the uncertainty surface needs to be generated every time when the parameters are changed (Sciacchitano 2019).

### 3.4.2.2. Cross-correlation peak ratio criterion

Approaches based on cross-correlation peak ratio criterion (Charonko and Vlachos 2013, among others) estimate the uncertainty from the quantities derived from cross-correlation plane without requiring any assumption or selection and evaluation of error sources (Sciacchitano 2019).

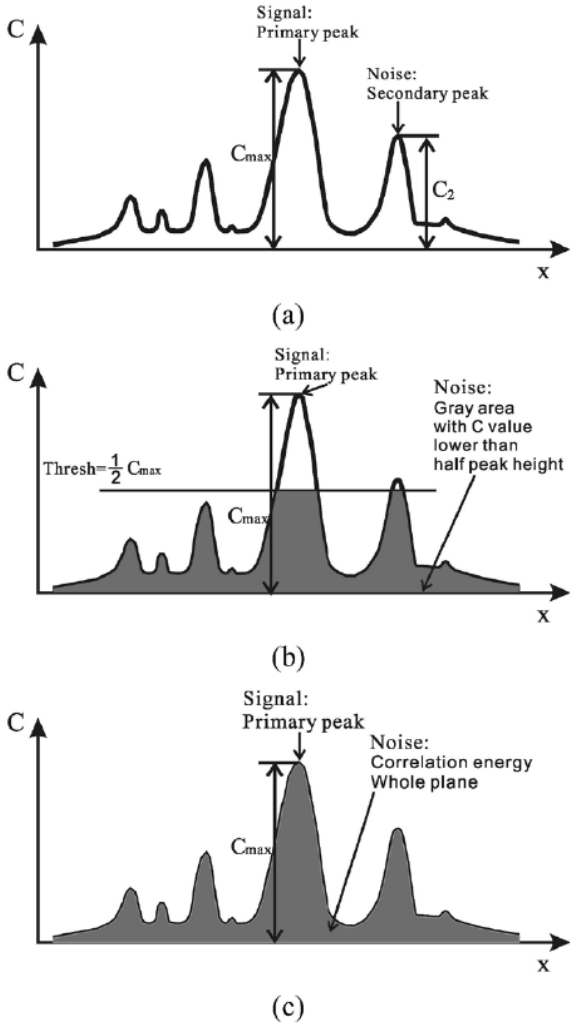


Figure 3.7. Graphical representation of 1D cross-correlation SNR: (a) primary peak ratio (PPR), (b) peak to root mean square ratio (PRMSR), (c) peak to correlation energy (PCE) (Xue et al. 2014)

In such methods, a metric ϕ representative of the signal-to-noise ratio (SNR) of the cross-correlation function is computed and is considered to be an empirical function of the experimental parameters or error sources. Different metrics for the evaluation of the cross-correlation SNR have been proposed in the literature, some of them are as shown in figure 3.7. Overall, these approaches are easy to implement and fully rely on the estimated cross-correlation function. However, the metric ϕ is empirically developed using synthetic images and the uncertainties of the displacement components are computed from the estimated uncertainty of the total displacement by following certain assumptions (Sciacchitano 2019).

### 3.4.2.3. Particle disparity method

Particle disparity or image matching method (Sciacchitano et al. 2013) is based on the contribution of individual particle images to the cross-correlation peak. If the particle images between the two PIV images match perfectly then there is a sharp peak in the cross-correlation function and the uncertainty is minimum. The width of the correlation peak represents the uncertainty bounds (see figure 3.8).

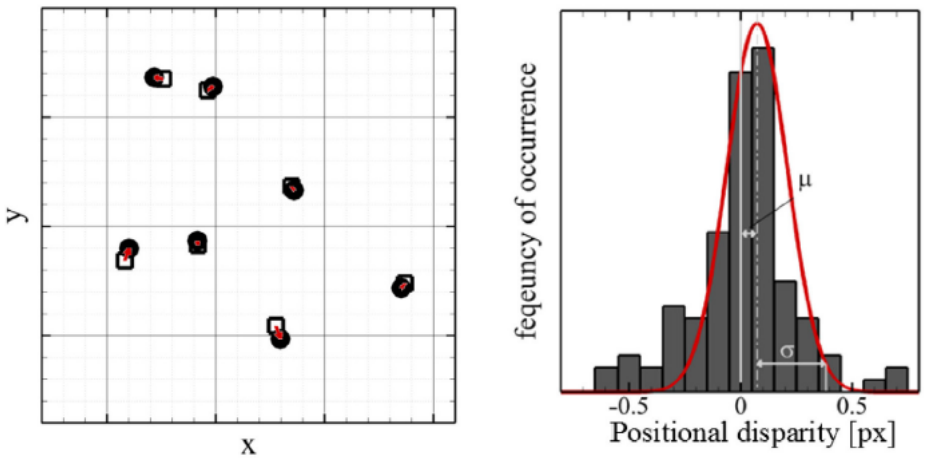


Figure 3.8. Illustration of the positional disparity between paired particle images (left) and their distribution (right) (Sciacchitano 2019)

When the particle images in the two images do not match perfectly, the correlation peak is wider and the uncertainty is higher. The method provides the standard uncertainty of each velocity vector without any assumptions on the flow and imaging conditions. However, it is dependent on identifying the individual particle images which can be erroneous in presence of overlapping particle images and poor imaging conditions (Sciacchitano 2019).

### 3.4.2.4. Correlation statistics approach

Correlation statistics approach (Wieneke 2015) is an extension of the particle disparity method (Sciacchitano et al. 2013) and based on the contribution of individual pixels in the images to the cross-correlation peak. While applying this approach, it is necessary to employ iterative multi-pass PIV algorithm with window deformation and predictor-corrector filtering (Sciacchitano 2019). The predictor-corrector scheme, after convergence, provides a symmetric cross-correlation peak by compensating the errors. The measurement error can be given by comparing the measured displacement associated with the symmetric correlation peak to the true displacement characterized by asymmetric correlation peak as shown in figure 3.9. The approach thus evaluates the contribution of each pixel in the image to the asymmetry of the correlation peak which in turn is associated with the uncertainty of the measured displacement.

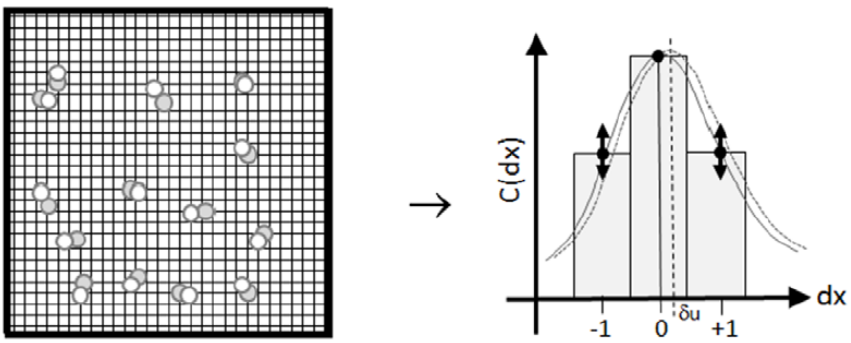


Figure 3.9. Illustration of the working principle of the correlation statistics method (Wieneke 2015)

# Chapter 4
# Survey on PIV Errors and Uncertainty Quantification

## Abstract

A survey on PIV error sources and uncertainty quantification (UQ) is performed and the outcomes are presented in this chapter. The aim of the survey is to understand how users and researchers in academia and industry perceive the PIV technique, especially for what concerns the measurement errors and uncertainties. A questionnaire is designed to determine the respondents' areas of work/research, type of PIV setup they typically employ, flow properties they measure, challenges they encounter, most significant error sources and their UQ strategies. Over 100 respondents have provided valuable answers to the questions and supporting explanations. The responses are analyzed both quantitatively and qualitatively. The quantitative results are presented in form of figures, such as pie charts, bar graphs, bubble plots, and are supported by the analysis of the descriptive answers from the respondents. Overall, this chapter not only provides a picture of the current status of PIV perceived by the users and researchers but also highlights areas where further development is needed.

## 4.1. Introduction

The complex measurement chain, which includes setting up the experiment, recording the particle images, processing them and then analyzing the results, is affected by errors from various sources (Sciacchitano 2019).

---

The work in this chapter has been published in Adatrao and Sciacchitano (2022) Survey on PIV errors and uncertainty quantification. 20th International Symposium on Applications of Laser and Imaging Techniques to Fluid Mechanics, Lisbon, Portugal, July 11-14.

Moreover, these error sources have different severity for different PIV users due to their level of experience, the type of experimental setup (e.g. planar PIV, stereoscopic PIV, tomographic PIV/PTV or LPT, micro-PIV, etc.), the flow cases (e.g. high speed flow, multi-phase flow, etc.) and flow properties (e.g. instantaneous or statistically derived) of interest (Kähler et al. 2016). However, a hierarchical classification of the PIV error sources has never been attempted, possibly because of the vast diversity of the experiments conducted in the PIV community. In particular, it is not clear which error sources affect the most the accuracy and precision of PIV measurements. Knowledge on this would create awareness in the PIV community and foster further developments for error minimization.

Additionally, error analysis and uncertainty quantification (UQ) are also of primary importance to the PIV users as demonstrated by the increasing number of scientific publications on the topic (see Sciacchitano 2019, among others). PIV results with known uncertainty levels are more trustworthy and therefore suitable for industrial applications and validation of numerical simulations. However, the experimental protocols and strategies for PIV-UQ may vary significantly among research groups and even individual researchers. It is thus considered important to determine how the PIV community tackles the topic of uncertainty quantification, and to understand whether the PIV users consider the available tools and approaches for PIV-UQ sufficient.

The present chapter aims to perform a survey among PIV users and researchers from all over the world to characterize the views of the community on PIV errors and uncertainty. The structure and design of the questionnaire for the survey is explained in section 4.2. The results of the survey are presented in section 4.3 with emphasis on the participants' views on advantages and limitations of PIV over other measurement techniques, PIV error sources and PIV-UQ.

## 4.2. Survey structure

The questionnaire, which is illustrated in form of a flow chart in figure 4.1, consists of 11 main questions with answers of two kinds, namely multiple-choice and descriptive answers. The multiple-choice questions allow simple quantitative analyses, whereas the descriptive answers provide qualitative data to support the quantitative results.

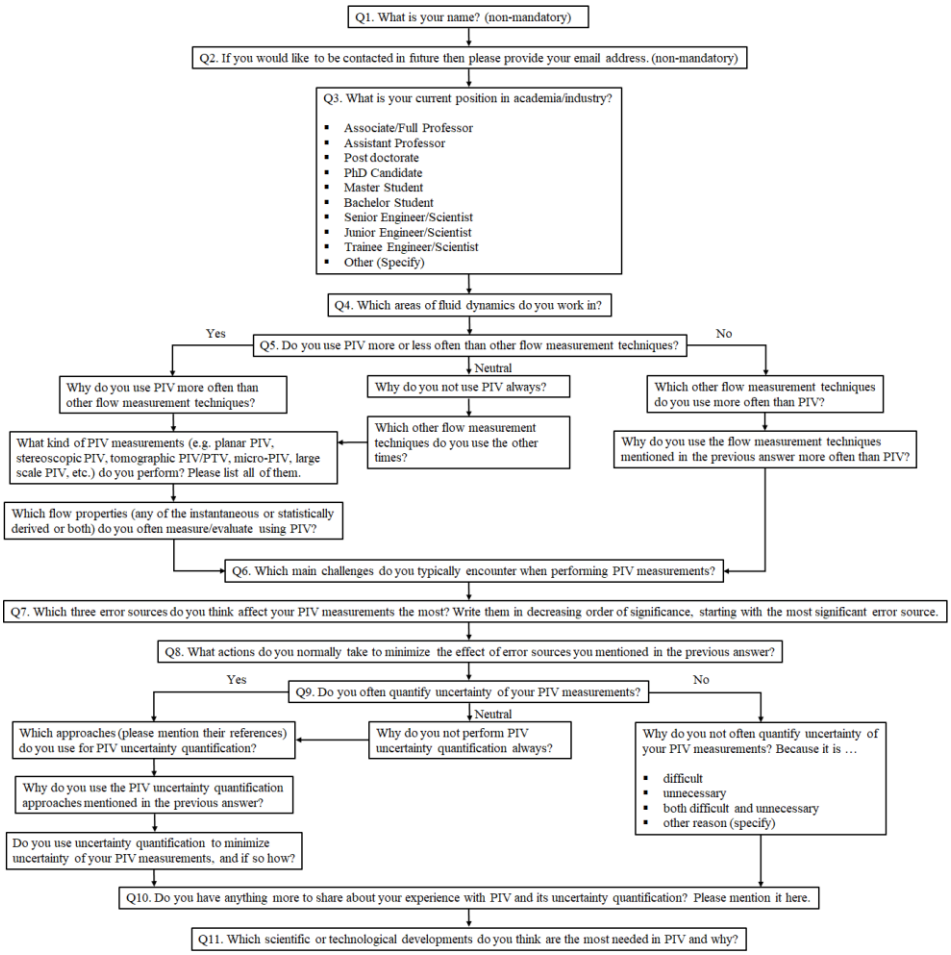


Figure 4.1. Flow chart of questionnaire designed for the survey

## 4. Survey on PIV Errors and Uncertainty Quantification

The questions have been formulated in order to receive answers from respondents about their areas of work/research, kind of PIV setup they employ, flow properties they measure, challenges they encounter, significant error sources and their PIV-UQ strategies. The questionnaire has been sent to 475 researchers from various countries and responses were received from 103 of them. Figure 4.2 shows the division of the respondents based on their present role in academia and industry.

Around 22% of the respondents are Associate/Full Professors, 13% are Assistant Professors, 21% are Post Doctorates, 18% are PhD Candidates, 20% are Senior Engineers/Scientists from the industries and other 6% are also from the industries with different function names. The respondents work in various research fields from fundamental sciences (such as biology, heat transfer, etc.) to applied sciences and engineering (such as automotive, aerospace etc.), from small scale flows to large scale flows, from low speed to high speed flows, and also in the development of measurement techniques for analyzing the fluid flows.

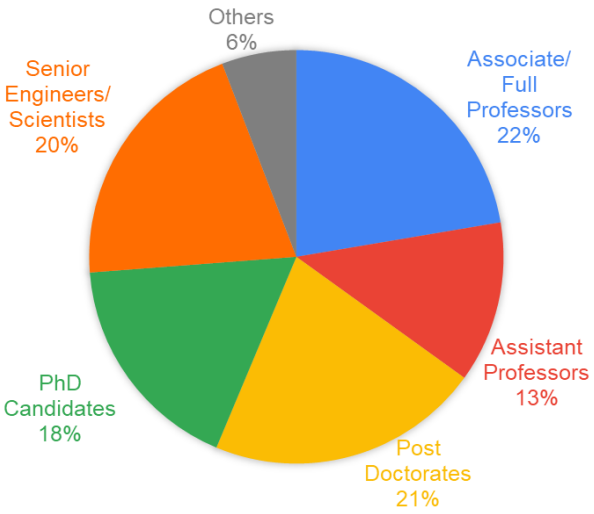


Figure 4.2. Pie chart of division of roles in academia and industry of the survey respondents

## 4.3. Results

The responses of the survey are analyzed both quantitatively and qualitatively. The results are presented in this section to highlight the views of the PIV users and researchers on advantages and limitations of PIV, significant error sources and uncertainty quantification methodologies.

### 4.3.1. Advantages and limitations of PIV

It is observed that not all the respondents use PIV as their primary measurement technique. Around 78% of them use PIV more often than other measurement techniques (typically Hotwire Anemometry, Laser Doppler Velocimetry, etc.), around 10% use other techniques more often than PIV, and the remaining 12% use PIV as frequently as the other techniques. The perceived advantages and limitations of PIV are summarized in figure 4.3.

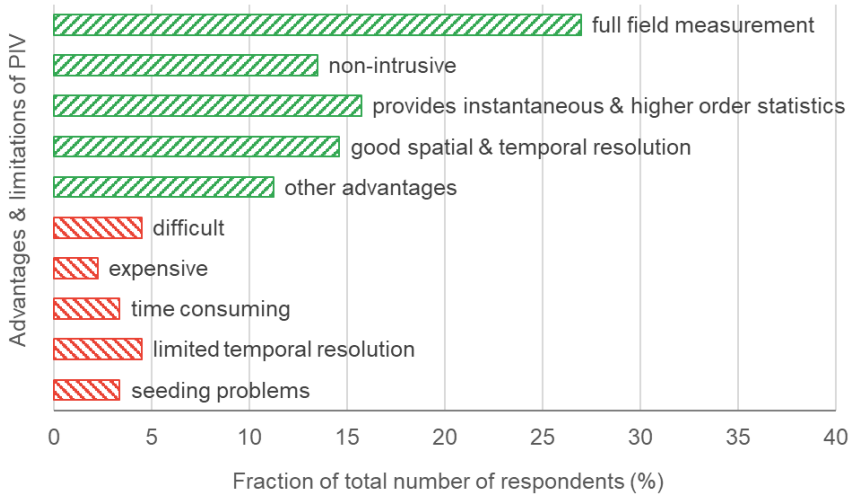


Figure 4.3. Advantages (green) and limitations (red) of PIV that make the technique more or less favorable than other techniques, respectively

The major advantages and limitations are shown in the bar graph where the length of the bar represents the percentage of respondents who have mentioned the respective advantage or limitation. Around 27% of the

respondents use PIV because it provides full field data as opposed to a single point measurement like Hotwire Anemometry (HWA) or Laser Doppler Velocimetry (LDV). PIV is non-intrusive (14% of the respondents), provides not only averaged velocity fields but also instantaneous and higher order statistics (16% of the respondents) and provides good spatial and temporal resolution (15% of the respondents). Another 11% of the respondents prefer PIV due to other advantages, namely high data efficiency, high accuracy and high information density, among others. Contrary, the main limitations and disadvantages in using PIV are that it is difficult to setup and execute, expensive to perform, time consuming (in terms of setup, acquisition and processing), provides limited temporal resolution compared to the other techniques (e.g. HWA) and is prone to various seeding problems (distribution, density, etc.). Overall, the survey shows that more researchers prefer PIV over other measurement techniques as its advantages overpower its limitations.

### 4.3.2. PIV error sources

In order to discuss the error sources in the PIV measurements, it is important to determine which types of PIV setup are most commonly used by the respondents. A pictorial representation of the types of PIV setup employed is shown in figure 4.4 in the form of a bubble chart.

The location of the center of the bubble along the vertical axis and its diameter represent the percentage of the total respondents who typically perform that kind of PIV experiment. It is clear that most of the PIV users perform planar 2-dimensional-2-component i.e. 2D2C (28% of the respondents) and stereoscopic 2D3C measurements (23%), followed by tomographic 3D3C PIV measurements (16%). Nevertheless, 3D measurements, especially tomographic particle tracking velocimetry (PTV) or Lagrangian particle tracking (LPT), are becoming more common. They are reported by 11% of the respondents. As mentioned earlier, the developments in the hardware and software have expanded the applications of PIV such that it is being used in large scale (9%) as well as micro scale (8%) measurements. The bubble of other measurements in the figure 4.4

accounts for 5% of the PIV users who work with specific applications, such as echo PIV and fluorescent PIV.

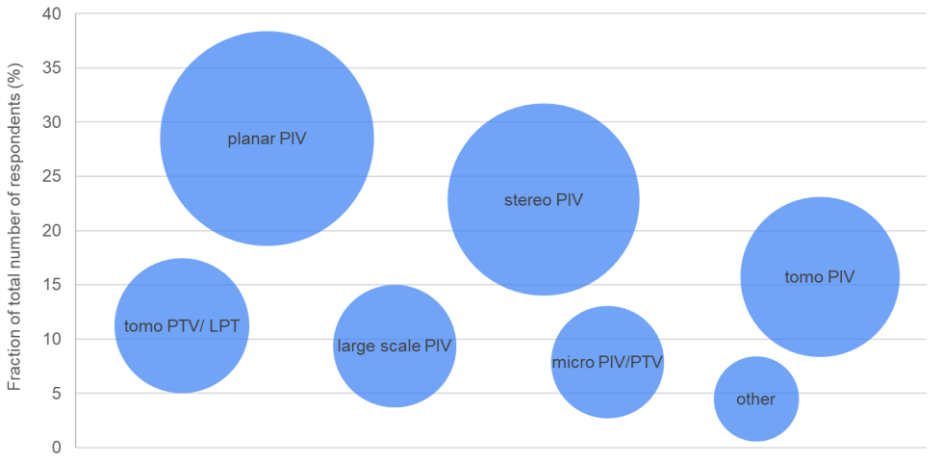


Figure 4.4. Types of PIV used by the survey respondents

All these PIV measurements suffer from errors from various sources during experimental setup, image acquisition and data processing. Figure 4.5 presents the most significant error sources encountered by the PIV community. It is clear that the problems related to the background image reflections and seeding are more severe than those of limited spatial resolution and distortions/ aberrations of the optical access. It is found that PIV users consider the error sources related to the experimental setup or image acquisition as more troublesome than those from the processing algorithms.

It is to be noted that the error sources have some correlation with the type of PIV measurements performed. This is verified by checking the responses of the PIV users separately who employ either planar (2D2C and 2D3C) measurement setups or volumetric 3D3C (tomographic PIV and 3D PTV/LPT) measurement setups. Figure 4.6 shows the division of the error sources based on the kind of PIV users i.e. the users who perform only planar measurements (2D users), the users who perform only volumetric

measurements (3D users) and the users who perform both planar and volumetric measurements (2D and 3D users).

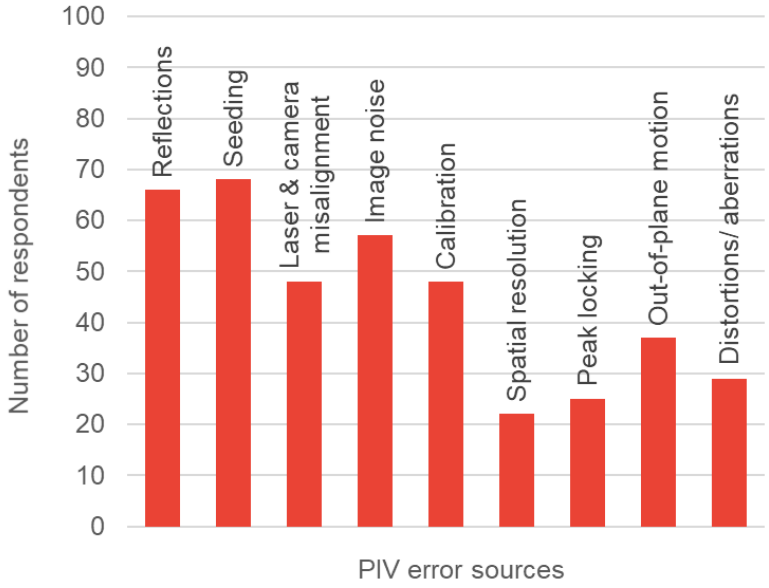


Figure 4.5. Most relevant error sources in PIV measurements

It is found that around 14%, 20% and 12% of the planar setup users (only 2D users) mentioned the reflections, seeding and image noise as the significant error sources, respectively. Similarly, the reflections, seeding and image noise are reported as the significant error sources by around 22%, 22% and 11% of the volumetric setup users (only 3D users), respectively. The errors due to calibration are considered more significant by the volumetric setup group (44%) than the planar setup group (10%). It is to be noted that the percentages here are related to the main effects of the kind of measurement setup i.e. 2D or 3D. The interaction effects which are hidden in the answers of the users who perform both 2D and 3D measurements are not evaluated.

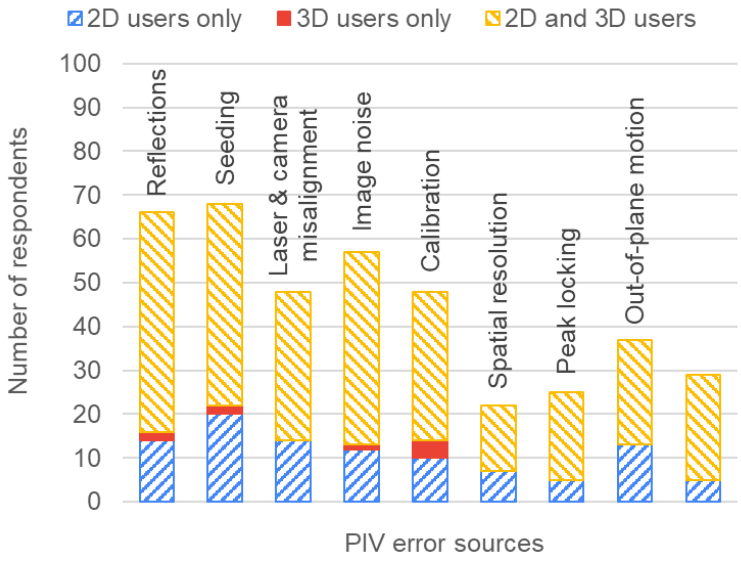


Figure 4.6. PIV error sources divided based on the kind of PIV users [2D users only: the users who employ only planar (2D2C and 2D3C) measurement setups, 3D users only: the users who employ only volumetric 3D3C (tomographic PIV and 3D PTV/LPT) measurement setups, 2D and 3D users: the users who employ both planar and volumetric setups]

### 4.3.3. PIV uncertainty quantification

Uncertainty quantification is of primary importance in any kind of measurements. The variety of error sources mentioned earlier makes UQ for PIV experiments as a challenging task (Sciacchitano 2019). While random error sources are promptly quantified by data statistics, the systematic effects of various error sources are often difficult to estimate (Smith and Oberkampf 2014). The survey reveals that the PIV users do not always quantify the uncertainty of their PIV measurements. In particular, it is found that only 49% of the PIV users always perform UQ, 41% perform it only sometimes, and 10% do not perform it at all [see figure 4.7(a)]. The major reasons for not always performing PIV-UQ are: limitation of the available PIV-UQ approaches to account for all the error sources; not well-defined approaches and hence difficulty to use them; unavailability of a standard and

recognized approach which can be used for all kinds of PIV measurements; requirement of extra efforts and resources. Moreover, for some of the PIV users, UQ is not necessary as they are interested in rough estimates of the flow or UQ is difficult due to the complexity of the measurements.

The users that perform PIV-UQ employ a wide variety of algorithms. Those include:

- Correlation Statistics (CS) method by Wieneke (2015);
- Data statistics (Coleman and Steele 2009, Benedict and Gould 1996);
- Cross-correlation Peak Ratio (PR) approach by Charonko and Vlachos (2013);
- Particle Disparity (PD) or Image Matching approach by Sciacchitano et al. (2013);
- Guide to Expression of Uncertainty in Measurement of the International Organization for Standardization (ISO-GUM 2018).

As demonstrated for the error sources, the choice of the PIV-UQ approach is also influenced by the kind of measurements employed by the PIV users. It is found that all the five approaches are mostly implemented by users of planar (2D2C and 2D3C) measurement setups. Instead, most of the users of volumetric 3D3C (tomographic PIV and 3D PTV/LPT) setups do not perform uncertainty quantification due to the complexity of the measurements and those who do perform uncertainty quantification make use of the statistics formulae to quantify the uncertainty. The other UQ approaches are found to be limited for volumetric measurements.

Figure 4.7(b) shows the pie chart of the percentages of the five major UQ strategies implemented by the planar setup users. It is clear that the CS method is the most used followed by the Statistics formulae, reported by 40% and 29% of the PIV users, respectively. Both of the approaches focus on random uncertainty. These methods are widely used because they are easy to implement, validated and found to be reliable by many users in the PIV community. The CS method has additional advantages in that it can provide the uncertainty of instantaneous data and the method is readily available in a commercial software. The other PIV-UQ approaches of PR, PD and ISO-GUM are also commonly used by around 10% of the PIV users each. The ISO-

GUM specifications for UQ are mostly of interest to the PIV users in the industry because they are standard and globally recognized.

While the PIV users can choose among many PIV-UQ algorithms, it is clear that none of them is universally considered the standard approach for PIV-UQ. Additionally, the approaches commonly used rely on data statistics and quantify the uncertainty stemming from random error sources, strongly underestimating the uncertainty due to systematic error sources. Hence, it is apparent that a comprehensive framework for PIV-UQ, universally acknowledged and accounting for both random and systematic errors, is still missing. Moreover, the survey reveals the need of a single PIV-UQ approach applicable to all kinds of measurements ranging from the planar (2D2C and 2D3C) to the volumetric 3D3C (tomographic PIV and 3D PTV/LPT) measurements.

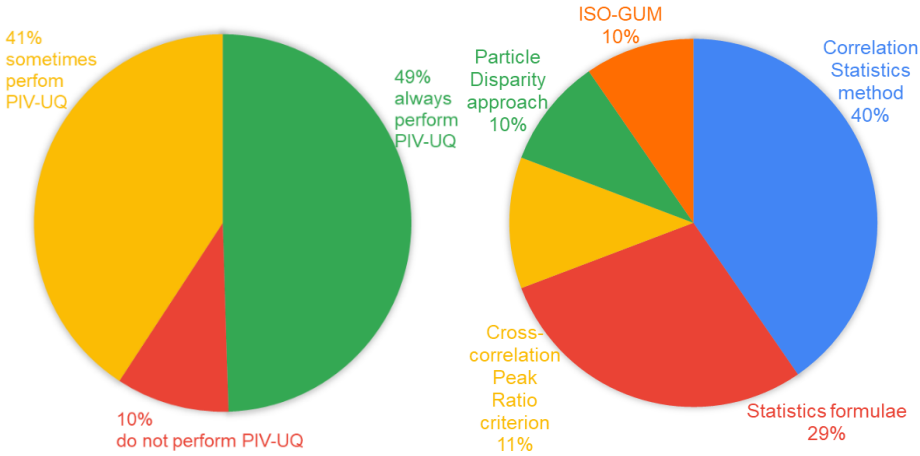


(a) (b)

Figure 4.7. Pie charts of (a) percentages of PIV users who perform or do not perform uncertainty quantification and (b) percentages of different UQ approaches used by the planar (2D2C and 2D3C) measurement setup users [Correlation Statistics method by Wieneke (2015); Statistics formulae (Coleman and Steele 2009, Benedict and Gould 1996); Cross-correlation Peak Ratio criterion by Charonko and Vlachos (2013); Particle Disparity or Image Matching approach by Sciacchitano et al. (2013); ISO-GUM: Guide to Expression of Uncertainty in Measurement of the International Organization for Standardization (ISO-GUM 2018)]

## 4.4. Conclusions

In this chapter, we performed a survey to determine how PIV users and researchers worldwide perceive the PIV error sources and the current approaches for uncertainty quantification. A questionnaire consisting of 11 questions has been formulated and sent to 475 researchers from both academia and industry. The total number of responses was 103, resulting in a response rate of 22%. The responses were analyzed quantitatively in pie charts, bar graphs and bubble plots, whereas the descriptive answers supported the analysis of the charts. Overall, it is found that the PIV community struggles more with the error sources associated with measurement setup and image acquisition, such as background image reflections, seeding density and its distribution, image calibration. Conversely, the image analysis step is perceived as easy and accurate, possibly because much work in the last three decades has been dedicated to optimize image interrogation algorithms to maximize the accuracy of the resulting velocity fields. Further detailed analysis was performed by separating the responses of two groups of PIV users, namely users who employ planar (2D2C and 2D3C) measurement setups and users who perform volumetric 3D3C (tomographic PIV and 3D PTV/LPT) measurements. It is found that the errors due to background image reflections, seeding and image noise are considered significant by both the groups. However, the errors due to the laser and camera misalignment and out-of-plane motion of particles are more relevant for the planar setup users. Contrary, the errors related to the calibration procedure are more problematic for the users of volumetric setups.

The PIV users are aware of the importance of uncertainty quantification (UQ). However, only 49% of the respondents always quantify the uncertainty of their PIV measurements. PIV users can choose among a wide range of UQ algorithms, some of which are also implemented in commercial software, thus making them easy to use. Nevertheless, given the wide variety of UQ approaches used, it is clear that no approach can be currently considered as the standard tool for PIV-UQ. Furthermore, the analysis of the two groups of PIV users employing either planar or volumetric setups shows

that the standard UQ approaches are limited for the uncertainty quantification in volumetric measurements. The need for a universally accepted PIV-UQ approach that can deal with random as well as systematic errors has emerged from this analysis.

# 4. Survey on PIV Errors and Uncertainty Quantification

# Chapter 5
# Multi-$\Delta t$ Approach for Peak-locking Uncertainty Quantification


## Abstract

A novel approach is devised for the quantification of systematic uncertainty due to peak locking in particle image velocimetry (PIV), which also leads to correction of the peak-locking errors. The approach, applicable to statistical flow properties such as time-averaged velocity and Reynolds stresses, relies on image recordings with multiple time separations $\Delta t$ and a least-squares regression of the measured quantities. In presence of peak locking, the measured particle image displacement is a non-linear function of $\Delta t$ due to the presence of measurement errors which vary non-linearly with the sub-pixel particle image displacement. Additionally, the measured displacement fluctuations are a combination of the actual flow fluctuations and the measurement error. When the image recordings are acquired with multiple $\Delta t$'s, a least-squares regression among the statistical results yields a correction where systematic errors due to peak locking are significantly diminished. The methodology is assessed for planar PIV measurements of the flow over a NACA0012 airfoil at 10 degrees angle of attack. Reference measurements with much larger $\Delta t$ than the $\Delta t$'s of the actual measurements,


---

The work in this chapter has been published in Adatrao S, Bertone M and Sciacchitano A (2021) Multi-$\Delta t$ approach for peak-locking error correction and uncertainty quantification in PIV. Meas. Sci. Technol. 32:054003.

The MATLAB scripts related to this work are available publicly on 4TU.ResearchData platform with DOI: https://doi.org/10.4121/13379120.v1.

The figures related to this work are available publicly on 4TU.ResearchData platform with DOI: https://doi.org/10.4121/13379174.v1.

such that relative peak-locking errors are negligible for the former, are used to assess the validity of the proposed approach.

## 5.1. Introduction

Several approaches have been proposed for quantification and correction of the peak-locking errors. A-priori estimations and correction of the peak-locking errors based on theoretical models were presented by Angele and Muhammad-Klingmann (2005) and Cholemari (2007). Both the models have showed the effect of peak locking on the turbulence statistics following the work of Christensen (2004). The peak-locking errors have been corrected by assuming Gaussian distribution for the displacement and velocity probability density functions in the former model (Angele and Muhammad-Klingmann 2005), whereas the correction has been achieved by assuming sinusoidal variation of the peak-locking error with respect to the sub-pixel displacement in the latter model (Cholemari 2007). A number of works on the peak-locking correction at the processing (i.e. velocity estimation) and post-processing stages have been devised in the literature. Roth and Katz (2001) have applied a histogram equalization to the sub-pixel particle image displacements for the correction. However, Hearst and Ganapathisubramani (2015) have demonstrated that pixel locking is non-uniform across an image. Therefore, identifying and adjusting for pixel locking with histograms computed based on the entire vector fields, as done by Roth and Katz (2001), may have been erroneous and the equalization process should be applied on a vector-by-vector basis (Hearst and Ganapathisubramani 2015). However, their approach is effective only in the absence of other error sources which might affect the histogram of the measured displacements and velocities. The peak-locking errors arising at the processing stage can be reduced by using state-of-the-art processing algorithms (Scarano 2002, Roesgen 2003, Chen and Katz 2005, Liao and Cowen 2005). However, the peak-locking errors due to small particle image diameters are difficult to quantify or correct for. The concept of defocusing to increase the particle image diameter has become a common practice: a slight defocusing has been shown effective in reducing the peak-locking

errors as reported by Overmars et al. (2010). However, the optimal amount of defocusing is not possible to estimate and the excessive defocusing increases random errors in the detection of the particle images (Kislaya and Sciacchitano 2018). Furthermore, defocusing cannot be applied in tomographic measurements, where the same amount of defocusing cannot be imposed to the particles of the entire measurement volume. Michaelis et al. (2016) proposed the use of optical diffusers to enlarge the particle image diameters by increasing the point spread function of the imaging system. A reduction of both systematic and random error components of the measured velocity by a factor of 3 was reported by Kislaya and Sciacchitano (2018). However, the effectiveness of the diffusers is limited for the CMOS cameras with large pixel size. Using the diffusers, a spread of about 10 μm for the incoming light can be achieved in the image plane (Michaelis et al. 2016). Nevertheless, several CMOS cameras feature pixel sizes exceeding 10 μm. For those cameras, as discussed by Kislaya and Sciacchitano (2018), peak-locking errors remain present even when using two optical diffusers as proposed by Michaelis et al. (2016); furthermore, the uncertainty associated with the peak locking errors remains unknown, as it cannot be easily evaluated via standard uncertainty quantification approaches (Sciacchitano et al. 2015).

The discussion above shows that the problem of peak-locking errors due to small particle image diameters, especially in the case of CMOS cameras for high-speed PIV measurements, is still unsolved. In such a situation, a continuous development in the approaches based on multiple $\Delta t$ image acquisition (Nogueira et al. 2009, Nogueira et al. 2011, Legrand et al. 2012, Legrand et al. 2018) has shown a high potential in peak-locking error quantification and correction, $\Delta t$ being a time separation between two frames in PIV. Using a set of different $\Delta t$'s for the same flow measurement allows for segregating the errors that scale with $\Delta t$ (e.g. peak-locking errors) from those that do not (Nogueira et al. 2011). The recent work of Legrand et al. (2018) has offered a 1-D analytical modeling of the peak-locking errors and has allowed for measurement correction. However, the method is iterative and computationally expensive to estimate the calibration coefficients mentioned in the algorithm. Also, selection of two $\Delta t$'s is not

trivial in presence of turbulence in the flow and the $\Delta t$ values should be adjusted for different levels of turbulence. In the present chapter, a simple approach based on a least-squares regression of the measured time-averaged displacements and Reynolds stresses from multiple $\Delta t$ acquisitions is proposed to correct the peak-locking errors and quantify the uncertainty. The proposed methodology and its validation are explained in sections 5.2 and 5.3, respectively. The approach is then assessed for planar PIV measurements of the flow over a NACA0012 airfoil in a wind tunnel; the experimental setup and the results of such assessment are presented in sections 5.4 and 5.5, respectively.

## 5.2. Proposed methodology

The peak-locking uncertainty in PIV measurements is proposed to be quantified and reduced using regression analysis from acquisitions with multiple $\Delta t$'s. The approach, applicable for stationary processes (whose statistics do not change in time), is devised for the uncertainty in the time-averaged displacements (and velocities) as well as Reynolds stresses.

### 5.2.1. Mean displacement and velocity

Consider a stationary process, where the local actual time-averaged flow velocity $\overline{u}_{true}$ is constant in time. When PIV measurements are conducted with inter-frame time separation $\Delta t$, the actual time-averaged particle image displacement in pixel units, not affected by any measurement error, is:

$$\overline{\Delta x}_{true} = \overline{u}_{true} \cdot \Delta t \cdot \frac{M}{s} \tag{5.1}$$

where, $M$ is the magnification factor relating the image plane to the object plane and $s$ is pixel size of the camera sensor.

From equation (5.1) it is evident that the actual particle image displacement increases linearly with the inter-frame time separation. In presence of the

peak-locking errors, the measured particle image displacement is the sum of the true displacement and the measurement error:

$$\overline{\Delta x} = \overline{u}_{true} \cdot \Delta t \cdot \frac{M}{s} + \varepsilon_{\overline{\Delta x}} = \overline{\Delta x}_{true} + \varepsilon_{\overline{\Delta x}} \tag{5.2}$$

The peak-locking errors are often modelled as a sinusoidal (or close-to-sinusoidal, Cholemari 2007) function of the sub-pixel particle image displacements, hence they vary non-linearly with $\overline{\Delta x}_{true}$. Therefore, the measured particle image displacement becomes a non-linear function of $\Delta t$, as illustrated in figure 5.1. In the proposed approach, the measurements are repeated with multiple $\Delta t$'s, provided that the $\Delta t$'s are selected such as to sample a sufficient portion of the peak-locking period (i.e. the variation of the time-averaged displacements is at least one pixel). Performing a linear regression of the measured displacements $\overline{\Delta x}(\Delta t)$ allows to average out the systematic errors $\varepsilon_{\overline{\Delta x}}$, thus yielding a regression displacement $\Delta x_{regr}(\Delta t)$ which is a better estimate of $\overline{\Delta x}_{true}$ (see figure 5.1).

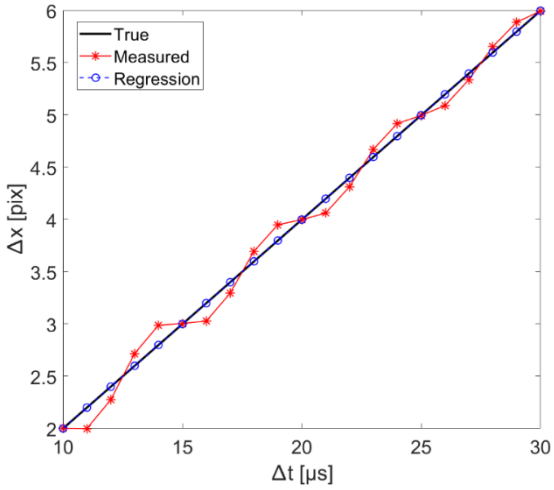


Figure 5.1. Graphical representation of measured displacements for multiple $\Delta t$ acquisitions and the displacements from least-squares regression of the measured displacements

#### 5.2.1.1. Quantification of peak-locking uncertainty

Following Coleman and Steele (2009), the uncertainty of the time-averaged displacement is divided into systematic uncertainty and random uncertainty:

$$U_{\overline{\Delta x}}(\Delta t) = \sqrt{U_{b,\overline{\Delta x}}^2 + U_{r,\overline{\Delta x}}^2(\Delta t)} \tag{5.3}$$

where, $U_{b,\overline{\Delta x}}$ and $U_{r,\overline{\Delta x}}(\Delta t)$ are the systematic and random uncertainties in the time-averaged displacement $\overline{\Delta x}$, respectively. In this work, we assume that the systematic uncertainty $U_{b,\overline{\Delta x}}$ is mainly ascribed to peak locking and not to the other bias error sources, such as modulation effects due to limited spatial resolution (Nogueira et al., 2005) or bias errors due to velocity gradients (Keane and Adrian, 1990; Cowen and Monismith, 1997). The random uncertainty $U_{r,\overline{\Delta x}}(\Delta t)$ can be attributed to several sources, including the actual flow fluctuations, noise in the recordings and out-of-plane particle motion (Raffel et al. 2018, Sciacchitano 2019).

Considering the regression displacement as the best estimate of the true displacement, the systematic uncertainty can be estimated based on the difference between the measured and regression displacements:

$$U_{b,\overline{\Delta x}} = t_{C.I.,\nu} \sqrt{\frac{1}{n-1}\sum_{i=1}^{n}\left[\overline{\Delta x}(\Delta t_i) - \Delta x_{regr}(\Delta t_i)\right]^2} \tag{5.4}$$

where, $t_{C.I.,\nu}$ is the *t*-statistic describing the desired confidence interval and $n$ is the number of $\Delta t$ acquisitions. In presence of severe peak locking, this systematic uncertainty constitutes a major part of the total uncertainty in the mean displacement, as can be seen in figure 5.1, where the measured time-averaged displacements are underestimated or overestimated producing large systematic error and leading to large systematic uncertainty.

The random uncertainty in the time-averaged displacement is due to the finite number of measurement samples (Coleman and Steele 2009) and is given by:

$$U_{r,\overline{\Delta x}}(\Delta t) = \frac{t_{C.I.,\nu}}{\sqrt{N}} \sqrt{\frac{1}{N-1}\sum_{i=1}^{N}\left[\Delta x_i(\Delta t) - \overline{\Delta x}(\Delta t)\right]^2} \tag{5.5}$$

where $N$ is the number of instantaneous measured displacements ($\Delta x$) at each $\Delta t$ acquisition. It is to be noted that the regression analysis does not affect the random uncertainty and random error in the measurements. The random uncertainty (and random error) in the time-averaged displacement at each $\Delta t$ acquisition can be reduced by acquiring large enough number of samples at that $\Delta t$ acquisition.

Moreover, when time-resolved PIV measurements are conducted, the instantaneous measured displacements are correlated. As a consequence, an additional term appears in the calculation of the total uncertainty, namely the correlated systematic uncertainty $U_{b,corr(\overline{\Delta x})}$ (Coleman and Steele 2009):

$$\begin{aligned} U^2_{b,corr(\overline{\Delta x})}(\Delta t) &= 2\sum_{i=1}^{N-1}\sum_{j=i+1}^{N}\left(\frac{\partial\overline{\Delta x}}{\partial\Delta x_i}\right)\left(\frac{\partial\overline{\Delta x}}{\partial\Delta x_j}\right)\sigma^2{}_{\varepsilon_b(\Delta x_i),\varepsilon_b(\Delta x_j)} \\ &= \frac{2}{N^2}\sum_{i=1}^{N-1}\sum_{j=i+1}^{N}\sigma^2{}_{\varepsilon_b(\Delta x_i),\varepsilon_b(\Delta x_j)} \end{aligned} \tag{5.6}$$

The value thus calculated in equation (5.6) should be added to the two terms under radical in equation (5.3) to calculate the total uncertainty in the time-averaged displacement.

The equation (5.6) can further be simplified considering that the covariance between the bias errors in the successive instantaneous displacements can be expressed as the product of the correlation coefficient (ρ) between them

and the individual standard deviations (σ) assuming normal distribution for the bias errors ($\varepsilon_b$).

$$U^2_{b,corr(\overline{\Delta x})}(\Delta t) = \frac{2}{N^2}\sum_{i=1}^{N-1}\sum_{j=i+1}^{N}\rho_{\varepsilon_b(\Delta x_i),\varepsilon_b(\Delta x_j)}\cdot\sigma_{\varepsilon_b(\Delta x_i)}\cdot\sigma_{\varepsilon_b(\Delta x_j)} \tag{5.7}$$

The estimation of the correlated systematic uncertainty $U_{b,corr(\overline{\Delta x})}$ is non-trivial as the bias errors in the instantaneous displacements are unknown and difficult to determine. Moreover, most of the measurements are followed by statistical analysis requiring uncorrelated samples in which case $U_{b,corr(\overline{\Delta x})}$ is negligible (or zero for completely uncorrelated samples). In this work, for sake of simplicity, only this case of uncorrelated samples is considered and the correlated systematic uncertainty is not included in the calculation of the total uncertainty. Finally, the total uncertainty in the measured time-averaged velocity $\overline{u}$ at each $\Delta t$ acquisition can be estimated using Taylor's approach from the uncertainty in the time-averaged displacement [calculated using equation (5.3)] at that particular $\Delta t$ acquisition:

$$U_{\overline{u}}(\Delta t) = \frac{U_{\overline{\Delta x}}(\Delta t)}{\Delta t}\cdot\frac{s}{M} \tag{5.8}$$

#### 5.2.1.2. Correction of peak-locking errors

The peak-locking errors in the time-averaged PIV measurements can be corrected for by removing the bias errors estimated via regression analysis. Thus, the measured displacements and velocities ($\overline{\Delta x}$ and $\overline{u}$) are replaced with the displacements and velocity from regression ($\Delta x_{regr}$ and $u_{regr}$), respectively. The total standard uncertainty in the corrected displacement at each $\Delta t$ acquisition is then given by the uncertainty of the regression model (Coleman and Steele 2009):

$$U_{\Delta x_{regr}}(\Delta t) = U_{b,\overline{\Delta x}}\sqrt{\frac{1}{n} + \frac{\left(\Delta t - \overline{\Delta t}\right)^2}{\sigma_{\Delta t,\Delta t}}} \tag{5.9}$$

where, $U_{b,\overline{\Delta x}}$ is the systematic peak-locking uncertainty in the measured mean displacement [calculated using equation (5.4)], $n$ is the number of $\Delta t$'s and $\sigma_{\Delta t,\Delta t}$ is the covariance in the $\Delta t$'s:

$$\sigma_{\Delta t,\Delta t} = \sum_{i=1}^{n} \Delta t_i^2 - \frac{(\sum_{i=1}^{n} \Delta t_i)^2}{n} \tag{5.10}$$

The uncertainty in the corrected velocity is then derived from the uncertainty in the corrected displacement using Taylor's approach. It is to be noted that the uncertainty in the velocity is calculated at the mean of the $\Delta t$'s, that is where the regression error is the minimum (Montgomery et al. 2011).

$$U_{u_{regr}} = \frac{U_{\Delta x_{regr}}\left(\overline{\Delta t}\right)}{\overline{\Delta t}} \cdot \frac{s}{M} = \frac{1}{\sqrt{n}}\left[\frac{U_{b,\overline{\Delta x}}}{\overline{\Delta t}}\right] \cdot \frac{s}{M} \tag{5.11}$$

### 5.2.2. Reynolds stress

When the flow is turbulent and the velocity fluctuations encompass at least one pixel, the mean velocity is usually unaffected by the peak-locking errors in the instantaneous velocities. In such cases, the peak-locking errors appear instead in the velocity fluctuations leading to inaccurate estimation of higher-order turbulent statistic, e.g. Reynolds stress (Christensen 2004).

The measured displacement fluctuations ($\Delta x'$) are a combination of the actual flow fluctuations ($\Delta x'_{true}$), the random error of the displacement measurement ($\varepsilon_{\Delta x}$) and the bias error fluctuations in the measured displacements ($b'_{\Delta x}$), as also explained by Wilson and Smith (2013a), Sciacchitano and Wieneke (2016) and Scharnowski et al. (2019a):

$$\Delta x' = \Delta x'_{true} + \varepsilon_{\Delta x} + b'_{\Delta x} \tag{5.12}$$

The equation (5.12) can be written in terms of total fluctuating measurement error ($\delta_{\Delta x} = \varepsilon_{\Delta x} + b'_{\Delta x}$) as:

$$\Delta x' = \Delta x'_{true} + \delta_{\Delta x} \tag{5.13}$$

and in terms of velocity fluctuations as:

$$u' = u'_{true} + \frac{\delta_{\Delta x}}{\Delta t} \cdot \frac{s}{M} \tag{5.14}$$

The equation (5.14) can also be written in terms of the total fluctuating error in physical units $\left(\delta_{\Delta X} = \frac{\delta_{\Delta x}}{\Delta t} \cdot \frac{s}{M}\right)$ as:

$$u' = u'_{true} + \delta_{\Delta X} \tag{5.15}$$

where, $\delta_{\Delta X}$ is the measured displacement in physical units (e.g. m or cm).

The measured variance of the velocity, or Reynolds stress, is then given by:

$$R_{uu} = R_{uu,true} + \frac{\sigma^2_{\delta,\Delta X}}{\Delta t^2} + \frac{2\, cov(u'_{true}, \delta_{\Delta X})}{\Delta t} \tag{5.16}$$

where, $R_{uu}$ (or $\sigma_u^2$) and $R_{uu,true}$ (or $\sigma_{u,true}^2$) are the measured and "true" Reynolds stresses, respectively.

The relative importance of the different terms in the right-hand-side of equation (5.16) is evaluated by means of Monte Carlo simulations. Two flow cases are considered, namely:

(i) mean velocity of 10 m/s (same as the free stream velocity) and low flow fluctuations with turbulence intensity of 4%;

(ii) mean velocity of 2.5 m/s and high flow fluctuations with turbulence intensity of 31%.

The two flow cases are representative of measurements in a potential-like flow region and turbulent region, respectively. The turbulence intensity is calculated as the ratio of RMS velocity fluctuations to the free stream velocity. The maximum absolute values of the peak-locking bias error and the measurement random error are 0.25 pixel and 0.05 pixel, respectively and are kept the same for the two cases for ease of comparison. It is to be noted that the peak-locking bias error is modelled as a sinusoidal function of the sub-pixel displacement following Cholemari (2007). Also, the camera pixel size ($s$) of 20 μm and magnification factor ($M$) of 0.4 are considered while generating the synthetic data for $\Delta t$'s = 10, 11, …, 30 μs; those values are representative of a typical high-speed PIV experiment conducted with CMOS camera sensors. The measured Reynolds stresses for these $\Delta t$'s along with the true Reynolds stress, error variance over $\Delta t^2$ and the covariance (between the velocity fluctuations and fluctuating error) over $\Delta t$ are plotted in figures 5.2(a) and (b) for the above mentioned synthetic data examples.

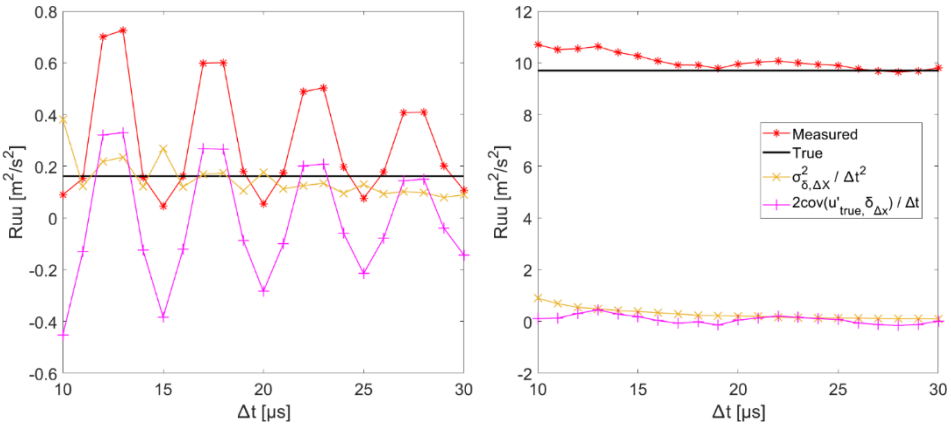


(a) (b)

Figure 5.2. Measured Reynolds stresses, true Reynolds stress ($R_{uu,true}$), error variance term ($\sigma^2_{\delta,\Delta X}/\Delta t^2$) and covariance term [$2\,cov(u'_{true}, \delta_{\Delta X})/\Delta t$], as mentioned in the equation (5.16) for the synthetic data- (a) in case (i) of potential flow region and (b) case (ii) of turbulent region

## 5. Multi-$\Delta t$ Approach for Peak-locking Uncertainty Quantification

When the flow fluctuations are low compared to the peak-locking bias error, as in the case (i) of potential flow, the effect of peak-locking errors is visible in terms of the non-linear (sine-like function) variation in the measured Reynolds stress with respect to $\Delta t$ or the sub-pixel displacement. This is due to the variation in the variance of total fluctuating error ($\sigma^2_{\delta,\Delta X}$) and the covariance of the true flow fluctuations and fluctuating errors in the measurements [$cov(u'_{true}, \delta_{\Delta X})$] with different $\Delta t$'s. It is to be noted that the covariance can be positive or negative based on the amount of flow fluctuations and the magnitude of peak-locking errors which in turn depends on the measured sub-pixel displacement at a particular $\Delta t$ acquisition. In particular, when the average fractional displacement is close to zero, as it occurs for $\Delta t$'s $= 10$, 11, 14, 15 and 16 μs, positive flow fluctuations will yield negative peak-locking errors (and vice-versa), thus resulting in negative values of the covariance terms at those $\Delta t$ acquisitions [figure 5.2(a)]. Instead, when the average fractional displacement is close to 0.5 pixels, positive (respectively negative) flow fluctuations will yield positive (negative) peak locking errors, thus resulting in positive values of the covariance terms [see for instance the results for $\Delta t$'s $= 12$ and 13 μs in figure 5.2(a)]. It is to be noted that this behavior of the covariance [$cov(u'_{true}, \delta_{\Delta X})$] with respect to $\Delta t$ in the case (i) of potential flow is due to the flow fluctuations being smaller than the magnitudes of peak-locking errors. When the flow fluctuations are higher than the magnitudes of peak-locking errors, the behavior of covariance is not trivial as can be seen in the case (ii) of turbulent region in figure 5.2(b). However, the covariance terms in the case (ii) also depend on the flow fluctuations, amount of peak locking and the measured sub-pixel displacements as in the case (i). Therefore, similar overall trends can be seen for the measured Reynolds stresses, error variances ($\sigma^2_{\delta,\Delta X}$) and covariances [$cov(u'_{true}, \delta_{\Delta X})$] in both the synthetic data cases of potential flow region and turbulent region in figures 5.2(a) and (b), respectively. However, the non-linear variation with respect to $\Delta t$ is smother in the case (ii) compared to that in the case (i). It is due to the flow fluctuations being higher than the magnitude of peak-locking error in this case. Thus, in presence of peak locking, the Reynolds stresses may be overestimated or underestimated depending on the inherent flow

fluctuations and the magnitude of peak-locking errors. In absence of peak locking, the Reynolds stresses are usually overestimated due to the random errors in the measurement as illustrated by Wilson and Smith (2013a) and also demonstrated by Scharnowski et al. (2019a) who estimated the turbulence levels of the flow facility using a multi-$\Delta t$ approach.

It is clear from equation (5.16) that the Reynolds stresses measured at a particular spatial location are different when the PIV measurements are carried out with different inter-frame time separations ($\Delta t$'s). Moreover, the error variance ($\sigma^2_{\delta,\Delta X}$) and the covariance [$cov(u'_{true}, \delta_{\Delta X})$] are functions of $\Delta t$ and in turn functions of sub-pixel displacement $\Delta x_{sub}$. Following Cholemari (2007), the fluctuating bias error due to peak locking is modelled as a sinusoidal function of measured sub-pixel displacement:

$$\delta_{\Delta X,i} = \left[\varepsilon_{\Delta x,i} + b'_{\Delta x,i}\right]\frac{s}{M} = \left[\varepsilon_{\Delta x,i} + A\,sin\left(2\pi\Delta x_{sub,i}\right)\right]\frac{s}{M} \tag{5.17}$$

where, $i$ represents the instantaneous measured values and $A$ is a constant.

Assuming that $\varepsilon_{\Delta x,i}$ and $b'_{\Delta x,i}$ are uncorrelated, the variance of the total errors in the displacement measurement at each $\Delta t$ acquisition is then given by:

$$\sigma^2_{\delta,\Delta X} = \left(\frac{s}{M}\right)^2 var\left(\varepsilon_{\Delta x,i}\right) + \left(\frac{A\cdot s}{M}\right)^2 var\left[sin\left(2\pi\Delta x_{sub,i}\right)\right] \tag{5.18}$$

Moreover, the synthetic data analysis shows that the covariance between the true velocity fluctuations and the fluctuating error varies non-linearly with $\Delta t$ or the sub-pixel displacement. Therefore, the covariance at each $\Delta t$ can be approximated as a cosine function of the mean measured sub-pixel displacement $\overline{\Delta x_{sub}}$ at that $\Delta t$ acquisition (figure 5.2):

$$cov(u'_{true}, \delta_{\Delta X}) = -B\,cos\left(2\pi\overline{\Delta x}_{sub}\right) \tag{5.19}$$

Substituting the equations (5.18) and (5.19) in the equation (5.16), the Reynolds stress is expressed as:

$$R_{uu} = R_{uu,true} + \frac{\left(\frac{s}{M}\right)^2 var\left(\varepsilon_{\Delta x,i}\right) + \left(\frac{A \cdot s}{M}\right)^2 var\left[sin\left(2\pi \Delta x_{sub,i}\right)\right]}{\Delta t^2} + \frac{-2B\, cos\left(2\pi \overline{\Delta x}_{sub}\right)}{\Delta t} \tag{5.20}$$

It is to be noted that the variance of the random errors $var\left(\varepsilon_{\Delta x,i}\right)$ in the equation (5.20) is constant for different $\Delta t$ acquisitions. Moreover, $s$, $M$, $A$ and $B$ are constants. Therefore, the equation (5.20) can also be written as:

$$R_{uu} = R_{uu,true} + \frac{\beta_1 + \beta_2\, var\left[sin\left(2\pi \Delta x_{sub,i}\right)\right]}{\Delta t^2} + \frac{\beta_3\, cos\left(2\pi \overline{\Delta x}_{sub}\right)}{\Delta t} \tag{5.21}$$

Thus, it is proposed to perform a least-squares non-linear regression of the form of equation (5.21) to estimate the "true" Reynolds stress from the measured Reynolds stresses at different $\Delta t$'s. The coefficients $\beta_1$ and $\beta_2$ are positive as they represent the variance and square of a constant, respectively. For the ease of processing, the non-linear regression model in the equation (5.21) can be transformed to a linear regression model (Montgomery et al. 2011) as:

$$R_{uu} = R_{uu,true} + \beta_1 p_1 + \beta_2 p_2 + \beta_3 p_3 \tag{5.22}$$

where,

$$p_1 = \frac{1}{\Delta t^2} \tag{5.23}$$

$$p_2 = \frac{var\left[sin\left(2\pi \Delta x_{sub,i}\right)\right]}{\Delta t^2} \tag{5.24}$$

$$p_3 = \frac{cos\left(2\pi \overline{\Delta x}_{sub}\right)}{\Delta t} \tag{5.25}$$

In principle, the accuracy of the measured Reynolds stresses is the maximum when a large $\Delta t$ is selected ($\Delta t \to \infty$). However, this condition cannot be met in practice due to limitations caused by the out-of-plane particle motion and by the increasing truncation errors (Raffel et al. 2018). Hence, the "true" Reynolds stress is estimated by conducting measurements with different $\Delta t$'s, and then fitting a curve of the type mentioned in equation (5.22) by least-squares regression, where $R_{uu,true}$ represents the best estimate of the "true" Reynolds stress.

The results of regression for the synthetic data can be seen in figures 5.3(a) and (b) for the potential flow region and turbulent region, respectively.

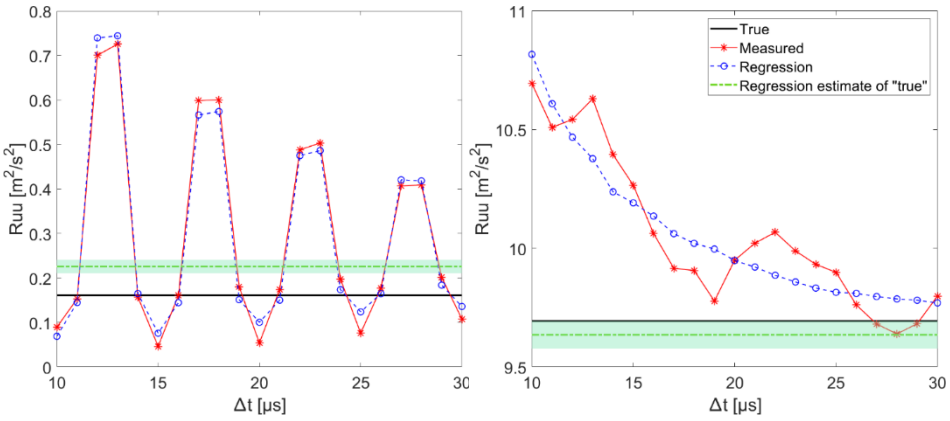


(a) (b)

Figure 5.3. Measured Reynolds stresses, true Reynolds stress, estimates of "true" Reynolds stress and the total Reynolds stress from the regression for the synthetic data- (a) in case (i) of potential flow region and (b) in case (ii) of turbulent region

It is clear that the total Reynolds stress from regression is comparable to the measured Reynolds stress at each $\Delta t$ in both the cases. Also, depending on the $\Delta t$, the measured Reynolds stress can differ significantly from the true Reynolds stress, as much as by 0.5 $m^2/s^2$ in the potential flow region and by 1 $m^2/s^2$ in the turbulent region. When the true Reynolds stress is estimated from the regression analysis, this difference is reduced to 0.07 $m^2/s^2$ and

0.05 $m^2/s^2$, respectively. The quantification of the uncertainty of the estimated "true" Reynolds stress is discussed in the following section 5.2.2.1.

### 5.2.2.1. Quantification of peak-locking uncertainty

The estimate of the "true" Reynolds stress obtained from regression $\hat{R}_{uu,true}$ represents a correction to the measured Reynolds stress, where the systematic error due to peak locking is removed, and can be used to quantify the systematic uncertainty in the measured Reynolds stress $R_{uu}$ at a given $\Delta t$:

$$U_{b,R_{uu}} = t_{C.I.,\nu}\sqrt{\frac{1}{n-4}\sum_{i=1}^{n}\left[R_{uu}(\Delta t_i) - \hat{R}_{uu,true}\right]^2} \tag{5.26}$$

where, $t_{C.I.,\nu}$ is the $t$-statistic describing the desired confidence interval and $n$ is the number of $\Delta t$ acquisitions.

Moreover, the random uncertainty in the measured Reynolds stress ($R_{uu}$) is given by (Sciacchitano and Wieneke 2016):

$$U_{r,R_{uu}}(\Delta t) = t_{C.I.,\nu}\sqrt{\frac{2}{N-1}}R_{uu}(\Delta t) \tag{5.27}$$

where, $N$ is the number of samples acquired at that $\Delta t$.

The random errors of the measured instantaneous velocity vectors are known to yield overestimated Reynolds stress values (Wilson and Smith, 2013b), consistently with the second term of the right-hand-side of equation (5.16). However, in presence of peak locking, the Reynolds stresses may be overestimated or underestimated depending on the covariance between the actual velocity fluctuations and the measurement error fluctuations. As a consequence, the uncertainty distribution of the Reynolds stresses is asymmetric:

$$U_{R_{uu},1}(\Delta t) = \sqrt{U_{b,R_{uu}}^2 + U_{r,R_{uu}}^2(\Delta t)} \tag{5.28}$$

$$U_{R_{uu},2}(\Delta t) = \sqrt{U_{r,R_{uu}}^2(\Delta t)} = U_{r,R_{uu}}(\Delta t) \tag{5.29}$$

where, $U_{R_{uu},1}$ and $U_{R_{uu},2}$ are the total uncertainties in the measured Reynolds stresses, either of them representing the upper or lower uncertainty bounds depending on the shape of error distribution (Wilson and Smith 2013a). Moreover, the shape of error distribution is influenced by the flow fluctuations, affected by the peak-locking errors, and it is different in the flow regions with low fluctuations than those with high fluctuations compared to the magnitude of the peak-locking errors. Therefore, in the case of overestimated Reynolds stresses $U_{R_{uu},1}$ and $U_{R_{uu},2}$ represent the lower and upper uncertainty bounds on the Reynolds stresses, respectively. Whereas, in the case of underestimated Reynolds stresses the lower and upper uncertainty bounds are given by $U_{R_{uu},2}$ and $U_{R_{uu},1}$, respectively.

The uncertainty of the estimated "true" Reynolds stress from regression $\hat{R}_{uu,true}$ can be expressed in terms of the uncertainty of the total Reynolds stress from regression $R_{uu,regr}$ (Montgomery et al. 2011):

$$U_{\hat{R}_{uu,true}}^2 = U_{R_{uu,regr}}^2 (P'P)^{-1} \tag{5.30}$$

where, $U_{R_{uu,regr}}$ is the uncertainty of the regression model and is calculated as:

$$U_{R_{uu,regr}} = t_{C.I.,\nu} \sqrt{\frac{1}{n-4} \sum_{i=1}^{n} \left[ R_{uu}(\Delta t_i) - R_{uu,regr}(\Delta t_i) \right]^2} \tag{5.31}$$

and $P$ is a $n \times 4$ matrix of regression variables $p_1$, $p_2$, $p_3$ (Montgomery et al. 2011):

$$P = \begin{bmatrix} 1 & p_{11} & p_{21} & p_{31} \\ 1 & p_{12} & p_{22} & p_{32} \\ \vdots & \vdots & \vdots & \vdots \\ 1 & p_{1n} & p_{2n} & p_{3n} \end{bmatrix} \tag{5.32}$$

where, $n$ is the number of $\Delta t$ acquisitions.

## 5.3. Validation of proposed methodology

It can be observed that the uncertainties in the measured mean velocity and Reynolds stress decrease with the increasing $\Delta t$ (or $\Delta x$) as the relative peak-locking errors for larger displacements (at larger $\Delta t$'s) are less than those for the smaller displacements (at smaller $\Delta t$'s), as also reported by Wilson and Smith (2013b). It is to be noted that the considered range of $\Delta t$'s should be sufficiently small such that the effect of other error sources such as velocity gradients and out-of-plane particle motion can be considered negligible. This fact is used for validation of the proposed uncertainty quantification approach where reference measurements are carried out with a much larger $\Delta t$ than the actual measurement $\Delta t$'s. The errors in the measured quantities can then be calculated with respect to the reference quantities. Comparing the errors with the uncertainties estimated using the proposed methodology (explained in Sections 5.2.1.1 and 5.2.2.1), it is possible to evaluate the effectiveness of the uncertainty quantification approach. Following Kislaya and Sciacchitano (2018), the reference measurements can be conducted with a time separation $\Delta t_{aux}$ which is much larger than the $\Delta t$'s used in the actual measurements. Due to the large displacement $\overline{\Delta x}_{aux}$ in the reference measurements, the relative peak-locking error in $\overline{\Delta x}_{aux}$ is negligible with respect to that in the measured displacements at $\Delta t$'s. The reference displacement $\overline{\Delta x}_{ref}$ at each $\Delta t$ is thus calculated from the auxiliary displacement $\overline{\Delta x}_{aux}$ measured at $\Delta t_{aux}$:

$$\overline{\Delta x}_{ref} = \overline{\Delta x}_{aux} \frac{\Delta t}{\Delta t_{aux}} \tag{5.33}$$

The reference velocity $\overline{u}_{ref}$ and Reynolds normal stress $R_{uu,ref}$ are equal to the auxiliary velocity $\overline{u}_{aux}$ and Reynolds normal stress $R_{uu,aux}$ respectively, from the auxiliary measurements:

$$\overline{u}_{ref} = \overline{u}_{aux} \tag{5.34}$$

$$R_{uu,ref} = R_{uu,aux} = \frac{1}{N-1}\sum_{i=1}^{N}\left(u_{aux,i} - \overline{u}_{aux}\right)^2 \tag{5.35}$$

where, $N$ is the number of instantaneous measured displacements (or velocities) in the reference measurements.

The errors in the measured quantities at each $\Delta t$ can then be calculated with respect to the reference quantities:

$$\varepsilon_{\overline{\Delta x}}(\Delta t) = \overline{\Delta x}(\Delta t) - \overline{\Delta x}_{ref}(\Delta t) \tag{5.36}$$

$$\varepsilon_{\overline{u}}(\Delta t) = \overline{u}(\Delta t) - \overline{u}_{ref} \tag{5.37}$$

$$\varepsilon_{R_{uu}}(\Delta t) = R_{uu}(\Delta t) - R_{uu,ref} \tag{5.38}$$

These errors in the measured displacements, velocities and Reynolds stresses are used to estimate the reliability of the uncertainty quantification approach by means of uncertainty coverages. An uncertainty coverage is the percentage of measurements for which the error magnitudes are contained within the uncertainty limits (Timmins et al. 2012):

$$|\varepsilon| \leq U \tag{5.39}$$

When $U$ represents the standard uncertainty, the uncertainty coverage ($C_U$) should be equal to the error standard deviation coverage ($C_{SD}$); the latter is calculated as the percentage of measurements for which the errors are within the standard deviation of the errors distributions:

$$|\varepsilon| \leq SD_{\varepsilon} \tag{5.40}$$

In case of Gaussian error distribution, the above is analogous to comparing the one-sigma uncertainty coverage to 68%, as done in Sciacchitano et al. (2015), among others. However, in the case of non-normal error distributions, it is necessary to first calculate the standard deviation of the errors and the corresponding standard deviation coverage to compare it with the uncertainty coverage. To assess the effectiveness of the uncertainty quantification approach, a term called relative coverage index (*RCI*) is proposed and is defined as the ratio between uncertainty coverage ($C_U$) and error standard deviation coverage ($C_{SD}$):

$$RCI = \frac{C_U}{C_{SD}} \tag{5.41}$$

Values of RCI close to one indicate accurate uncertainty estimations. Values of *RCI* less than one indicate that the uncertainty is underestimated, whereas values greater than one show that it is overestimated. Note that this parameter is applicable to any error distribution after estimation of the errors standard deviation.

## 5.4. Experimental setup

Planar PIV measurements of the flow over a NACA0012 airfoil at 10 degrees angle of attack were performed. Figure 5.4 illustrates a schematic of the experimental setup. The experiment was conducted in the W-tunnel of Delft University of Technology, which is an open-jet open-return wind tunnel with an exit cross section of 0.4 × 0.4 m² and an area contraction ratio of 9. The maximum achievable free-stream velocity is 30 m/s with 0.3% turbulence intensity (Tummers 1999). In this experiment, the free stream velocity was set to 10 m/s. The flow was seeded by a SAFEX seeding generator, which produces water-glycol droplets of 1 μm mean diameter. The particles were illuminated by a Quantronix Darwin-Duo laser (Nd:YLF, pulse energy of 25mJ at 1 kHz, wavelength of 527 nm) and images were recorded with a

LaVision High Speed Star 6 CMOS camera (12 bits, 20 μm pixel size, 1024 × 1024 pixels maximum resolution). The camera was equipped with a Nikon objective of 105 mm focal length and the optical aperture was set to $f_{\#} = 5.6$. A field of view (*FOV*) of 45 mm × 45 mm was imaged with optical magnification of 0.46, which resulted in a theoretical particle image diameter of 0.5 pixel, following Raffel et al. (2018). The small size of the particle image diameter caused peak locking in the measured displacements, influencing the estimation of mean velocity and Reynolds stresses.

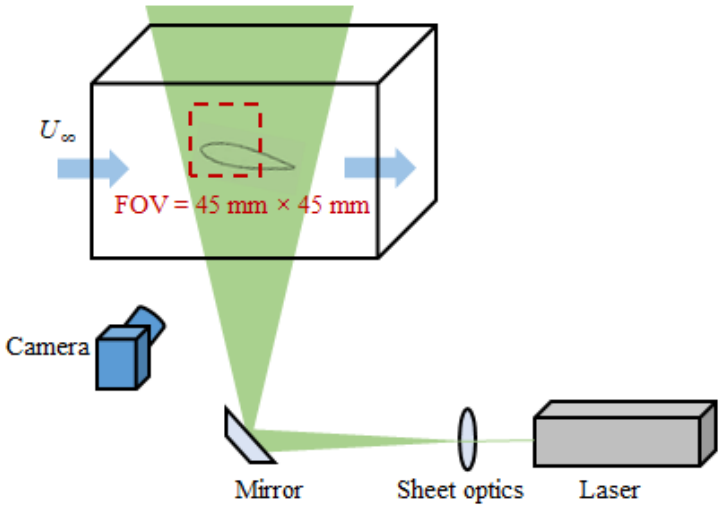


Figure 5.4. Schematic experimental setup of the planar PIV measurements of the flow over a NACA0012 airfoil at 10 degrees angle of attack

The image acquisition was conducted at a frequency of 200 Hz independently for multiple $\Delta t$'s from 10 μs to 24 μs in steps of 2 μs. The data sets at each $\Delta t$ consisted of 500 double-frame images. To validate the proposed multi-$\Delta t$ approach, reference measurements were conducted with optical aperture $f_{\#} = 11$ and the time separation $\Delta t$ of 50 μs, which is larger than the $\Delta t$'s used in the actual measurements, following Kislaya and Sciacchitano (2018). It is to be noted that the effect of out-of-plane motions and gradient bias errors is negligible in the measurements with $\Delta t$ of 50 μs, as the free-stream particle image displacement is equal to 11.5 pixels. The

processing was done via the LaVision DaVis 10 software, using Gaussian interrogation windows of 64 × 64 pixels with 75% overlap for the initial passes and 16 × 16 pixels with 75% overlap for the final passes.

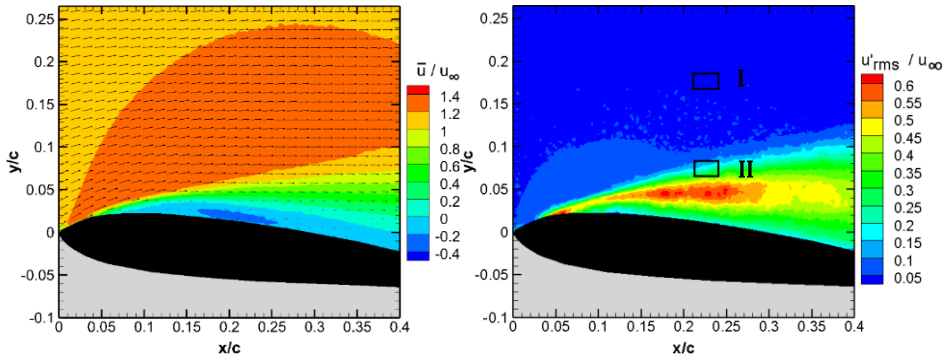


Figure 5.5. (a) Time-averaged velocities and (b) RMS of velocity fluctuations in the reference measurements, normalized with respect to the free stream velocity (Regions I and II are the areas where the proposed approach is applied and demonstrated in section 5.5)

The estimated time-averaged velocities ($\bar{u}$) and RMS of the velocity fluctuations ($u'_{rms}$) in the reference measurements, normalized with respect to the free stream velocity ($u_\infty$), are shown in figures 5.5(a) and (b), respectively. It is clear that the flow has varying degrees of fluctuations, e.g. low fluctuations in the potential flow region ($0 < u'_{rms}/u_\infty < 0.05$) and relatively high fluctuations in the turbulent region ($0.2 < u'_{rms}/u_\infty < 0.6$). As a consequence, the measured flow field is considered suitable to assess the effectiveness and limitations of the proposed approach in a range of flow conditions encountered in typical PIV measurements. A detailed analysis of the peak-locking errors correction and uncertainty quantification is conducted in regions I and II of figure 5.5(b), corresponding to the potential flow region and a turbulent region, respectively.

## 5.5. Results

The approach proposed in section 5.2.1 is applied to correct the peak-locking errors in the measured mean displacements and velocities, where the uncertainties in the corrected displacements and velocity obtained from regression are also provided. The analogous approach discussed in section 5.2.2 is then applied to correct the measured Reynolds stresses and quantify the uncertainty. The results are shown for the two selected regions in the flow as marked in figure 5.5(b).

### 5.5.1. Mean displacement and velocity

From the displacement plots of figure 5.6, it is evident that, while the reference displacement increases linearly with $\Delta t$, the measured mean displacement does not, consistently with the discussion of section 5.2.1. It is clear from figures 5.6(a) and (b) that the regression displacement is much closer to the reference displacement, indicating a significant reduction in the peak-locking errors.

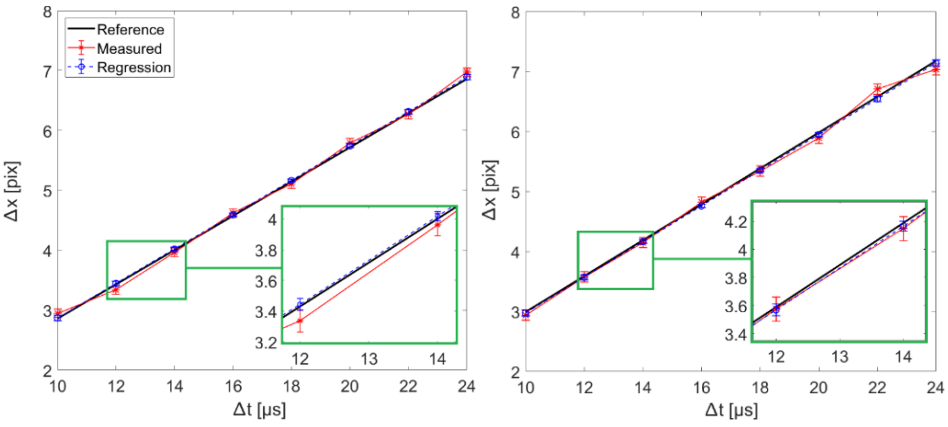


(a) (b)

Figure 5.6. Reference displacements, measured displacements and regression displacements with one standard deviation uncertainty bounds at (a) a point [$(x/c, y/c) = (0.23, 0.17)$] in the potential flow region I and (b) a point [$(x/c, y/c) = (0.23, 0.07)$] in the turbulent region II, the two regions being marked by rectangles in figure 5.5(b)

The reduction in the peak-locking errors can further be seen in figures 5.7(a) and (b), where the errors in the measured mean displacement and the regression displacements at each $\Delta t$, calculated with respect to the corresponding reference displacements, are shown. The maximum errors in the measured displacements are observed to be around $\pm 0.15$ pixels in both the regions I of potential flow [figure 5.7(a)] and II of high turbulence [figure 5.7(b)]. Whereas, the errors in the regression displacements are very close to zero in both the regions, being below 0.05 pixels. The peak-locking errors in the measured displacements are reduced up to 86% in the potential flow region I and up to 73% in the turbulent region II, when correcting the measured displacements by linear regression.

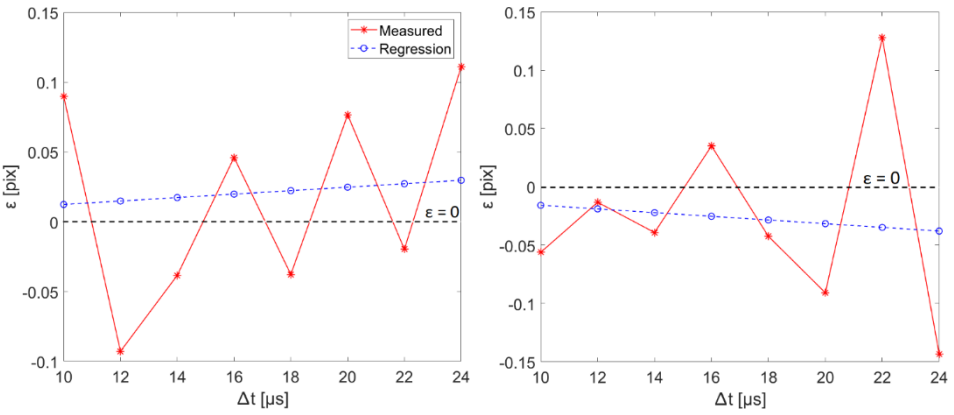


(a) (b)

Figure 5.7. Errors in measured displacements and regression displacements with respect to the reference displacements at (a) a point $[(x/c, y/c) = (0.23, 0.17)]$ in the potential flow region I and (b) a point $[(x/c, y/c) = (0.23, 0.07)]$ in the turbulent region II, the two regions being marked by rectangles in figure 5.5(b)

The uncertainty bounds are also shown for both the uncorrected (measured) and corrected displacements (from regression) in figure 5.6. In the potential flow region, as shown in figure 5.6(a), the uncertainties in the measured displacements are around 0.07 pixels at different $\Delta t$'s, whereas those on the regression displacements are around 0.03 to 0.05 pixels.

Similarly, in the turbulent region, shown in figure 5.6(b), the uncertainties in the measured displacements are around 0.09 pixels at different $\Delta t$'s, and those on the regression displacements are around 0.03 to 0.05 pixels.

Figures 5.8(a) and (b) show the distributions of the errors in the measured displacements and the regression displacements with respect to the reference displacements in the regions I and II, respectively. In the potential flow region [figure 5.8(a)], the pdfs of error distributions for different $\Delta t$ acquisitions are narrow and separated from each other and from the pdf of regression error distribution. Whereas, in the turbulent region [figure 5.8(b)], they are wide and close to each other and close to the regression one. The reason behind the pdfs being narrow in the potential flow region and wide in the turbulent region is the inherent fluctuations in the flow which are low in the potential flow region I and relatively high in the turbulent region II. Moreover, in the potential flow region, where the fluctuations are low, the peak-locking errors are significant and vary drastically (largely overestimated or underestimated) with varying $\Delta t$. As a consequence, the error pdfs exhibit different mean values, from -0.13 pixels at $\Delta t = 12$ µs to +0.16 pixels at $\Delta t = 10$ µs. Although the errors at most $\Delta t$'s exhibit an approximately normal distribution, at some $\Delta t$'s the distribution is skewed positively (e.g. $\Delta t = 12$ µs) or negatively (e.g. $\Delta t = 20$ µs). Conversely, the error distribution stemming from the linear regression has a Gaussian shape, with 0.02 pixels mean and 0.001 pixels standard deviation. In contrast, in the turbulent region, the large velocity fluctuations induce particle image displacement variations larger than the peak-locking errors; as a consequence, the errors pdfs exhibit lower variations with varying $\Delta t$. Nevertheless, the mean errors vary between -0.11 pixels and +0.08 pixels depending on the selected $\Delta t$. The application of the linear regression reduces the mean bias error to -0.04 pixels. It should be remarked that, as it is clear from figures 5.8(a) and (b), the pdfs of displacement error distribution in different $\Delta t$ acquisitions lie on either side of the pdf of regression displacement error distribution. This is due to the fact that the measured mean displacements are overestimated or underestimated depending on the sub-pixel displacement which in turn depends on $\Delta t$.

Analogous results in terms of time-averaged velocity are illustrated in figure 5.9. The errors in the measured velocities calculated with respect to the reference velocity are reduced up to 86% in the potential flow region I and up to 73% in the turbulent region II, after correcting the measured velocities by the regression analysis. In the potential flow region [figure 5.9(a)], the uncertainty in the corrected velocity estimated from the regression analysis is 0.07 m/s, which is much smaller than the uncertainties in the measured mean velocities (0.13 to 0.31 m/s) at different $\Delta t$'s. Similarly, in the turbulent region [figure 5.9(b)], the uncertainties of 0.17 to 0.36 m/s in the measured mean velocities are reduced to the uncertainty of 0.07 m/s in the corrected velocity obtained from regression. Thus, the overall reductions of the velocity uncertainties between 50% and 80% are achieved in both regions I and II.

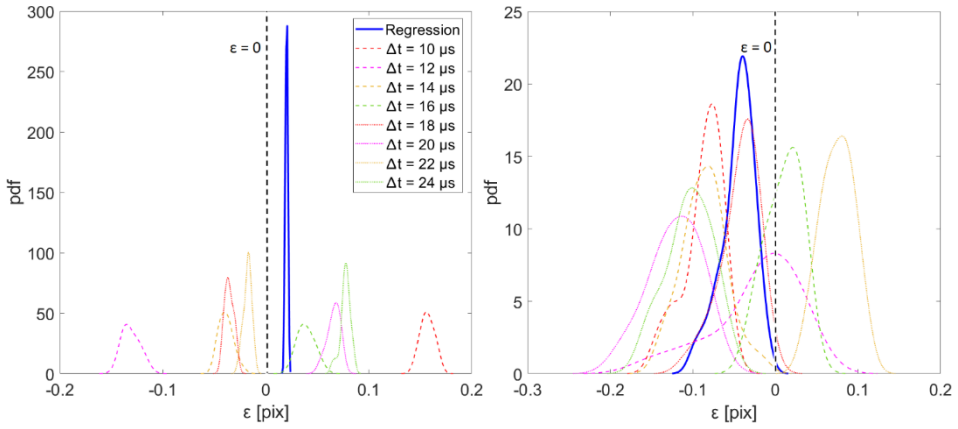


(a) (b)

Figure 5.8. Error distributions for the measured displacements and regression displacements from multiple $\Delta t$ acquisitions in (a) the potential flow region I and (b) the turbulent region II, the two regions being marked by rectangles in figure 5.5(b)

A visual comparison of the reference, measured and regression velocities is conducted in figure 5.10. A particular zoomed area in the flow field is selected to make the comparison vivid. It is clear that, the mean measured velocities at different $\Delta t$ acquisitions are either overestimated or

underestimated with respect to the velocities in the reference measurement depending on the sub-pixel displacement. For example, in the top region of the selected area, the measured velocities are overestimated at $\Delta t = 10$ µs and 24 µs, whereas, they are underestimated at $\Delta t = 12$ µs, consistent with figure 5.9(a) for the potential flow region. These measured velocities at different $\Delta t$ acquisitions are thus corrected by the regression analysis as can be seen in the third row of figure 5.10. It is clear that the corrected mean velocities from the regression are comparable to the corresponding mean velocities from the reference measurement.

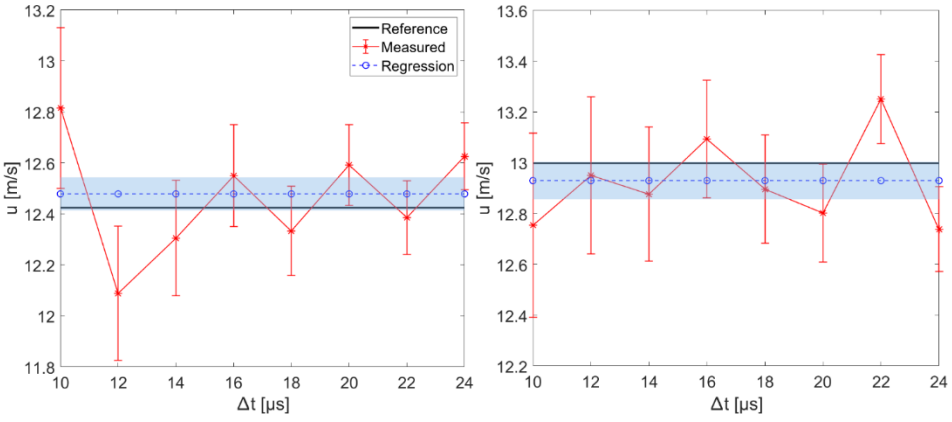


(a) (b)

Figure 5.9. Reference velocity, measured velocities and regression velocity with one standard deviation uncertainty bounds at (a) a point $[(x/c, y/c) = (0.23, 0.17)]$ in the potential flow region I and (b) a point $[(x/c, y/c) = (0.23, 0.07)]$ in the turbulent region II, the two regions being marked by rectangles in figure 5.5(b)

The uncertainty coverages ($C_U$) for the uncertainties in the measured displacements and velocities are calculated following equation (5.39). The uncertainties exhibit a coverage of 52% and 62% considering the measurements at different $\Delta t$ acquisitions in the potential flow region I and turbulent region II, respectively. Whereas, the standard deviation coverages ($C_{SD}$), calculated by the equation (5.40) are 61% and 70% in the regions I and II, respectively. Thus, the relative coverage indices ($RCI$) for the

uncertainty quantification in the measured displacements and velocities are 0.85 and 0.89 in the potential flow region I and turbulent region II, respectively. This analysis proves the validity of the proposed approach for uncertainty quantification as the *RCI*'s are close to one and the uncertainties are slightly underestimated in both the regions.

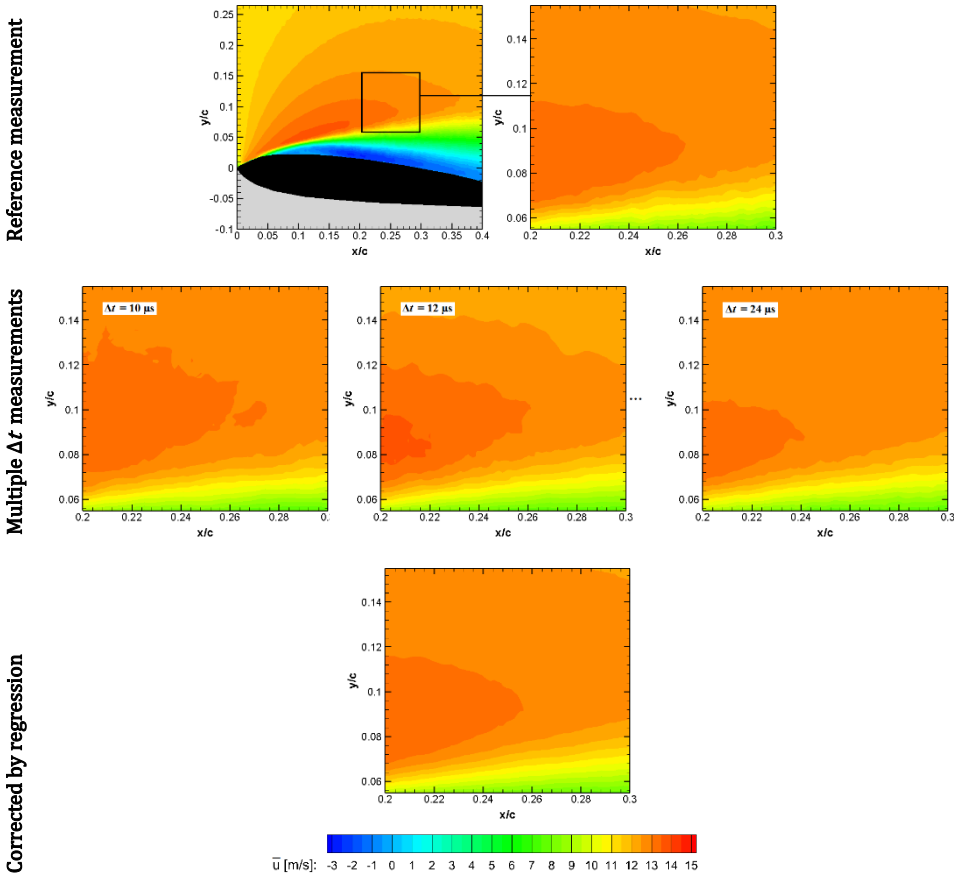


Figure 5.10. Measured time-averaged velocities in the reference measurement, in multiple $\Delta t$ acquisitions and after correcting by the regression analysis

### 5.5.2. Reynolds stress

The results of the proposed methodology for correcting the Reynolds stresses are summarized in figures 5.11(a) and (b) in the potential flow

region and turbulent region, respectively. It is clear from figure 5.11(a) that the effect of peak-locking errors is significant and can be seen by non-linear variation of the measured Reynolds stresses with respect to $\Delta t$. Such result is associated with the magnitude of flow fluctuations being lower than the magnitude of peak-locking errors in this region I of potential flow, consistent with the results of the Monte Carlo simulations described in section 5.2.2. Conversely, in the turbulent region II, the measured Reynolds stresses show smoother variation with respect to the changing $\Delta t$. In this region, the effect of the peak-locking errors is hidden due to the inherent flow fluctuations being higher.

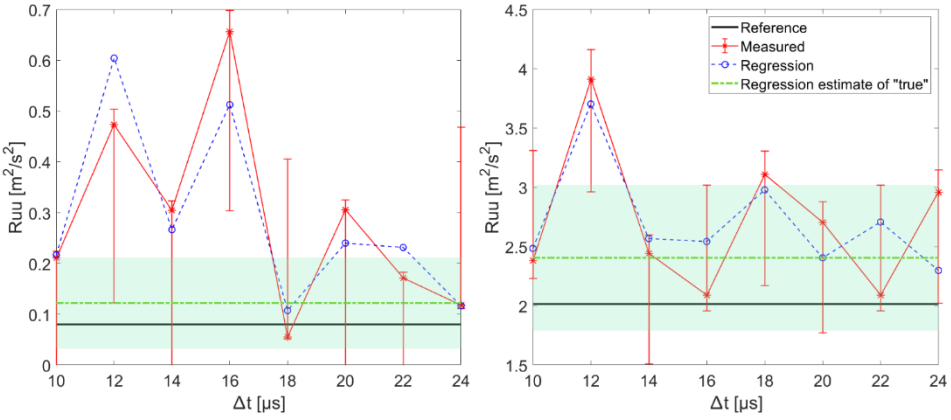


(a) (b)

Figure 5.11. Reference, measured and regression Reynolds stresses with the estimates of "true" Reynolds stress ($\hat{R}_{uu,true}$) at (a) a point [$(x/c, y/c) = (0.23, 0.17)$] in the potential flow region I and (b) a point [$(x/c,\ y/c) = (0.23,\ 0.07)$] in the turbulent region II, the two regions being marked by rectangles in figure 5.5(b). Red error bars and green shaded regions represent one standard deviation uncertainty in the measured and estimated "true" Reynolds stress, respectively

The reference Reynolds stress in the potential flow region is 0.08 $m^2/s^2$ which is comparatively low due to the low flow fluctuations in this region. However, the measured Reynolds stresses overestimate the reference value by up to 700%. The regression approach provides an estimate of the

Reynolds stress that agrees within 50% with the true value. Conversely, in the turbulent region, higher flow fluctuations are encountered and the reference Reynolds stress is 2.0 $m^2/s^2$. The measured Reynolds stresses in this region are overestimated by 4% to 95%. When the regression approach is employed, the estimated Reynolds stress is slightly overestimated by 19% with respect to the reference value.

The errors in the measured Reynolds stresses are calculated with respect to the reference one using the equation (5.38) and the pdfs of the error distributions are shown in figures 5.12(a) and (b) for the potential flow region I and the turbulent region II, respectively. It is clear that the pdfs are narrow in the region I and wider in the region II due to the inherent low flow fluctuations in the region I and high flow fluctuations in the region II, as also observed for the displacement error distributions. The errors in the regression Reynolds stress are comparatively lower than that in the measured Reynolds stresses at different $\Delta t$'s. Most of the errors in the potential flow region are positive, whereas those in the turbulent region are either positive or negative. Moreover, most of the pdfs for the measured Reynolds stresses lie on the positive side of the regression pdf in region I; in region II, instead, the pdfs of the measured Reynolds stresses lie on both positive and negative sides of the regression pdf. This fact is accounted for in the calculation of the total uncertainty in the Reynolds stresses at each $\Delta t$ using equations (5.28) and (5.29). For the Reynolds stresses overestimated with respect to the regression estimate, $U_{Ruu,1}$ represents the lower uncertainty bound and $U_{Ruu,2}$ is the upper uncertainty bound. Whereas, in case of the underestimated Reynolds stresses, $U_{Ruu,1}$ and $U_{Ruu,2}$ are the upper and lower uncertainty bounds, respectively, as can be seen in figures 5.11(a) and (b). In the potential flow region I, the largest uncertainty bound in the measured Reynolds stresses is 0.35 $m^2/s^2$, whereas the uncertainty in the corrected Reynolds stress (i.e. the estimate of the "true" Reynolds stress from regression) is 0.09 $m^2/s^2$. At the point in the turbulent region II, the bigger uncertainty bound in the measured Reynolds stresses is around 0.95 $m^2/s^2$, whereas the uncertainty in the corrected Reynolds stress is 0.61 $m^2/s^2$. The uncertainties in the measured Reynolds stresses are reduced by around 75% in the potential flow region, and by around 35% in the turbulent

region, after correction with the estimates of the "true" Reynolds stresses from regression.

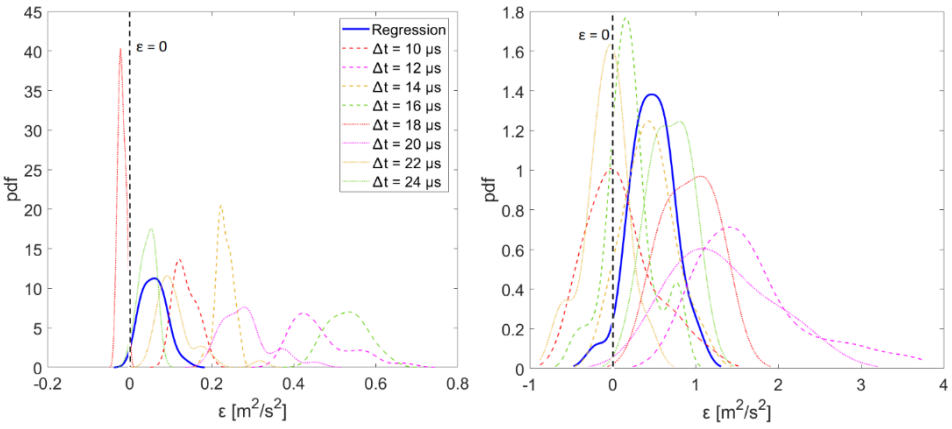


(a) (b)

Figure 5.12. Error distributions for the measured Reynolds stresses and the regression estimate of "true" Reynolds stress from multiple Δ*t* acquisitions in (a) the potential flow region I and (b) the turbulent region II, the two regions being marked by rectangles in figure 5.5(b)

The uncertainty coverages ($C_U$) are determined by comparing the calculated uncertainties with the errors (computed with respect to the reference measurements) in the measured Reynolds stresses as per the equation (5.39). The coverages for the errors standard deviation are also calculated using the equation (5.40). In the potential flow region I, the uncertainties exhibit a coverage ($C_U$) of 73% and the corresponding error standard deviation coverage ($C_{SD}$) is 61%. These values lead to the relative coverage index ($RCI$) of 1.2 indicating that the uncertainties in the measured Reynolds stresses are slightly overestimated in the potential flow region. In the turbulent region II, the uncertainty coverage is 64% and the error standard deviation coverage is 72%, resulting in $RCI = 0.89$. Thus the Reynolds stress uncertainties are slightly underestimated in the turbulent region.

The results of the regression analysis are also summarized in figure 5.13, where the reference Reynolds stresses and the corrected Reynolds stresses

are shown along with the measured Reynolds stresses at different $\Delta t$ acquisitions. It is to be noted that the measured values only at three $\Delta t$'s are plotted for sake of conciseness.

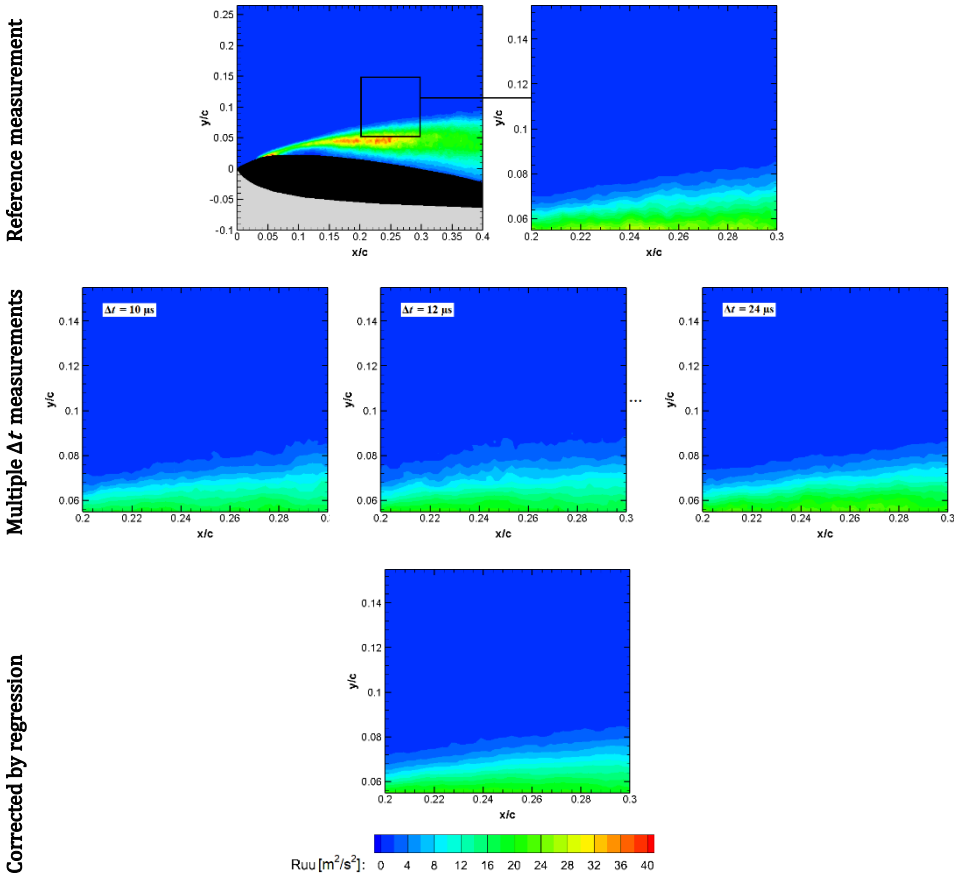


Figure 5.13. Measured Reynolds stresses in the reference measurement, in multiple $\Delta t$ acquisitions and after correcting by the regression analysis

Consistent with the findings of figure 5.11(b), the measured Reynolds stresses in the bottom region of the selected area are overestimated at $\Delta t$'s $= 12$ and 24 µs. The corrected Reynolds stresses by the regression analysis in this bottom region are slightly underestimated with respect to the reference values and are found to be comparable to the measured Reynolds

stresses at $\Delta t = 10$ µs acquisition. Similarly, in the potential flow region of this selected area in figure 5.13, the corrected Reynolds stresses are comparable to the reference ones, as also were seen in the figure 5.11(a). The results show that the peak-locking errors can be reduced by the regression analysis in the Reynolds stresses.

### 5.5.3. Selection of $\Delta t$'s

The proposed approach is based on the simple concept of least-squares regression of the measured quantities from multiple $\Delta t$ acquisitions. The selection of $\Delta t$'s is an important step in the methodology. The first requirement for the selection of the $\Delta t$'s is that a minimum number of four $\Delta t$'s is considered. This requirement is a direct consequence of the four-degree of freedom model ($\beta_0$, $\beta_1$, $\beta_2$ and $\beta_3$) employed for the Reynolds stress. Additionally, it is deemed likely that the accuracy of the regression result degrades when the range of the selected $\Delta t$'s covers a particle image displacement below one pixel, that is less than a period of the peak-locking error. Hence, the second requirement for selecting the $\Delta t$'s is that the particle image displacement range, defined as the difference between the largest time-averaged displacement (occurring in the acquisition with the largest $\Delta t$) and the smallest time-averaged displacement (for the smallest $\Delta t$), should be at least one pixel. In this section, the effect of the number of $\Delta t$'s selected for the regression analysis and the displacement range is investigated. Based on the two requirements, two sets of four values of $\Delta t$'s each are selected arbitrarily in the NACA0012 experiment. It is to be noted that, with four $\Delta t$ acquisitions, it is possible to perform the regression analysis for Reynolds stresses and to correct the peak-locking errors by the estimated "true" Reynolds stress from the regression. However, it is not feasible to compute the uncertainty in the estimate of "true" Reynolds stress, as the regression curve passes exactly through all the data points. The two sets of $\Delta t$'s are selected as follows: set I consists of measurements at $\Delta t$'s equal to 10, 12, 14, 16 µs, whereas in set II the measurements are performed at $\Delta t$'s of 10, 14, 18, 22 µs.

The proposed approach of regression is applied for both the cases of $\Delta t$'s to correct the measured mean displacements (and velocities) and Reynolds stresses. It can be seen in figure 5.14(a) that the measured displacements cover more than one pixel range in both cases of $\Delta t$'s. Hence, the corrected displacements in both the cases are comparable to the reference displacements, and to each other. However, when the measured displacements do not cover one pixel range, the regression is not effective. This result is due to the majority of the measured displacements lying on one side of the reference displacements, resulting in the regression displacements to be on the same side and away from the reference one. Thus, for the effective displacements regression, it is necessary to have both the overestimated and underestimated measured displacements, which is possible when the range is greater than or equal to one pixel.

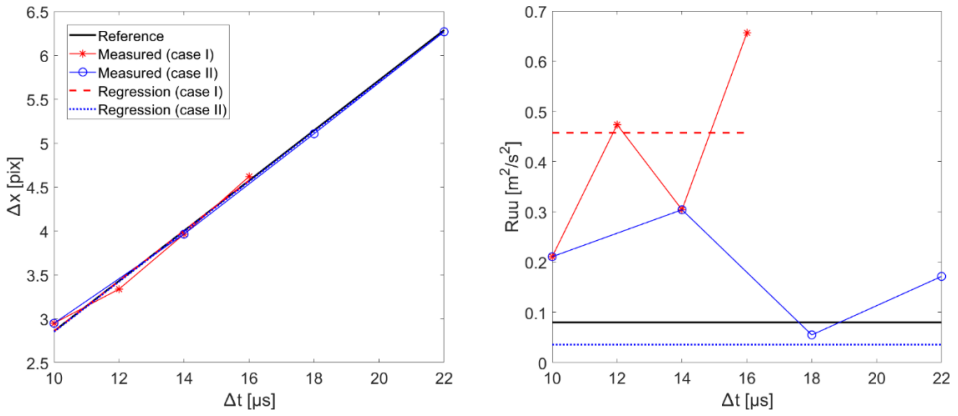


(a) (b)

Figure 5.14. Measured and corrected (a) displacements and (b) Reynolds stresses at a point $[(x/c, y/c) = (0.23, 0.17)]$ (case I: $\Delta t$'s = 10, 12, 14, 16 μs and case II: $\Delta t$'s = 10, 14, 18, 22 μs)

When analyzing the Reynolds stresses results [figure 5.14(b)], it is clear that the corrected Reynolds stress in the case II is closer to the reference one than that in the case I. This is because of the larger range of $\Delta t$'s in the case II. Thus the regression in the case II performs slightly better than that in the case I.

Nevertheless, the Reynolds stress estimated with the four $\Delta t$'s of set II is less accurate than the result obtained from the full set of eight $\Delta t$'s, which has been shown in figure 5.11(a). Hence, although four is the minimum number of time separations for the regression analysis, the use of more $\Delta t$'s can further increase the accuracy of the estimated Reynolds stresses.

Furthermore, to quantify the uncertainty in the estimate of "true" Reynolds stress from regression, more than four data points or measured Reynolds stresses are required. Therefore, in the present work, eight $\Delta t$'s were selected with the gap of 2 μs between the consecutive values while acquiring the measurements, the results of which were presented in the sections 5.5.1 and 5.5.2. As a guideline for future applications of the proposed methodology, it is suggested that more than four $\Delta t$'s are selected, and that the particle image displacement range covers at least one pixel in the regions of interest, to ensure an effective evaluation and correction of the peak-locking errors.

## 5.6. Conclusions

A novel approach is proposed for the quantification of the peak-locking systematic uncertainty in PIV, which in turn also corrects the measured particle image displacement (and velocity) and Reynolds stress for peak-locking errors. The approach is based on the assumption that local flow statistics are constant in time, according to which the particle image displacement should vary linearly with the time separation ($\Delta t$) between two frames. However, in the presence of peak locking, the measured particle image displacement is a non-linear function of $\Delta t$ as the measurement error in the displacement varies non-linearly with sub-pixel particle image displacement. Similarly, in presence of peak locking the Reynolds stress may vary significantly depending on the selected $\Delta t$. Hence, in the present approach, it is proposed to acquire the measurements at various $\Delta t$'s and perform a least-squares regression of the measured quantities (displacements and Reynolds stresses). The displacement (and velocity) and Reynolds stress from regression represent more accurate estimates of the "true" values and thus used to quantify systematic errors and

uncertainty due to peak locking in the measured displacement (and velocity) and Reynolds stresses, respectively. Guidelines for the selection of the $\Delta t$'s are also provided. The methodology is assessed for planar PIV measurements of the flow over a NACA0012 airfoil at 10 degrees angle of attack. The uncertainties in the measured velocity and Reynolds stresses are reduced by 50 to 80% and 35 to 75%, respectively, after correcting by the regression analysis. Relative coverage indices close to one are obtained for the mean velocity uncertainty and Reynolds stress uncertainty in both the potential and turbulent regions of the flow, indicating the ability of the methodology to quantify the uncertainty associated with peak-locking errors.

# Chapter 6
# Design of Experiments (DOE) for PIV Uncertainty Quantification

## Abstract

A statistical tool called Design of Experiments (DOE) is introduced for uncertainty quantification in particle image velocimetry (PIV). DOE allows to quantify the total uncertainty as well as the systematic uncertainties arising from various experimental factors. The approach is based on measuring a quantity (e.g. time-averaged velocity or Reynolds stresses) several times by varying the levels of the experimental factors which are known to affect the value of the measured quantity. Then, using Analysis of Variances (ANOVA), the total variance in the measured quantity is computed and hence the total uncertainty. Moreover, the analysis provides the individual variances for each of the experimental factors, leading to the estimation of the systematic uncertainties from each factor and their contributions to the total uncertainty. The methodology is assessed for planar PIV measurements of the flow over a NACA0012 airfoil at 15 degrees angle of attack considering five experimental factors, namely camera aperture, inter-frame time separation, interrogation window size, laser sheet thickness and seeding density. Additionally, the methodology is applied to the investigation by stereoscopic PIV of the flow at the outlet of a

---

The work in this chapter has been published in Adatrao S, van der Velden S, van der Meulen M-J, Cruellas Bordes M and Sciacchitano A (2022) Design of Experiments: a statistical tool for PIV uncertainty quantification. Meas. Sci. Technol. 34:015201.

The MATLAB scripts related to this work are available publicly on 4TU.ResearchData platform with DOI: https://doi.org/10.4121/20495787.v1.

The figures related to this work are available publicly on 4TU.ResearchData platform with DOI: https://doi.org/10.4121/20496108.v1.

ducted Boundary Layer Ingesting (BLI) propulsor. The total uncertainty in the time-averaged velocity as well as the constituent systematic uncertainties due to the experimental factors, namely camera aperture, inter-frame time separation, interrogation window size and stereoscopic camera angle, are quantified.

## 6.1. Introduction

Design of Experiments (DOE) is a statistical tool used in many fields of science and engineering to evaluate the systematic effect of input factors on the measurement output (Coleman and Montgomery 1993). The approach was first proposed for wind tunnel measurements by DeLoach (2000) at NASA Langely Research Center due to its various advantages over conventional One Factor At a Time (OFAT) wind tunnel testing. The chief advantage is that DOE focuses on the generation of adequate prediction models rather than high volume data collection (DeLoach 2000). In a comparison study between OFAT and DOE wind tunnel testing, DeLoach and Micol (2011) showed that the DOE method is more efficient in terms of both resources requirements and ease of data analysis. By using DOE, DeLoach et al. (2012) were able to quantify the total variance in their wind tunnel measurements and segregate the random and systematic components. The tests were performed in a transonic wind tunnel on a NACA0012 airfoil to compute lift and drag at various angles of attack. The authors found that the systematic component of the variance due to the time variations in sample means was as significant as the ordinary random error. Therefore, the authors concluded that it is important to identify any sources of systematic errors and eliminate them when possible. However, they also highlighted that a residual level of variance is unavoidable, whose systematic component is likely to exceed its random component. An accurate assessment of uncertainty requires that systematic variations be taken into account along with the random variations in the data (DeLoach et al. 2012).

Aeschliman and Oberkampf (1998) first demonstrated how DOE could be applied to measurement uncertainty quantification by choosing the bias error sources as factors of interest. Oberkampf and Roy (2010) reported the

use of DOE for wind tunnel validation experiments; additionally, they compared the DOE uncertainties with those from the ISO/ANSI method. The authors found that the random component of uncertainty, i.e. uncertainty computed by comparing a large number of replications of the experiment, compare well with the ISO/ANSI approach. However, the total estimated experimental uncertainty using the DOE technique was significantly greater than that estimated by the ISO/ANSI method. With the ISO/ANSI approach, the analyst must make assumptions about which individual uncertainty sources are present as well as the relative magnitudes of those uncertainties and their correlations and interactions. Conversely, in DOE the levels of the related experimental factors are varied to measure the response multiple times such that the main effects of the uncertainty sources as well as their correlations and interactions can be computed rather than assumed.

Smith and Oberkampf (2014) demonstrated that a simplified version of DOE, named Error Sampling Method (ESM), was an alternative tool to overcome the limitations of the traditional PIV-UQ methods. The ESM requires the repetition of an experiment after varying one or more possible sources of errors. In ESM, one seeks to replace as many aspects of the experiment as possible, starting with those that are likely to cause error and that can be varied. By doing so, one is sampling the experimental bias errors, making it possible to quantify the uncertainty due to these contributing error sources. The DOE and ESM techniques provide a means to determine the impact of any variable (i.e. a bias), as well as interaction between the variables (i.e. correlations). In order to do so, one needs to design an experiment in such a way that variations of systematic error sources can be sampled (Smith and Oberkampf 2014).

DeBonis et al. (2012) made use of a methodology based on DOE to quantify the uncertainty in PIV data for validation of Computational Fluid Dynamics (CFD) simulations. The uncertainties were estimated by comparing the measurements at the intersections of span-wise and stream-wise planes. These comparisons returned not only the uncertainty associated with the statistical convergence of the results, but also a wider range of systematic uncertainties, e.g. due to changes in the laser sheet thickness or

interrogation window size. The work showed that the total uncertainty of mean velocity measurements was much larger than that estimated by traditional methods. However, it is to be noticed that the PIV-UQ was conducted only at the intersection lines of the two measurement planes, whereas the uncertainty was not quantified in the rest of the fluid domain. A similar validation experiment using DOE was performed by Rhode and Oberkampf (2012) to assess the predictive accuracy of CFD models for a blunt-body supersonic retro-propulsion configuration at various Mach numbers. The total experimental uncertainty and the constituent uncertainties from a range of sources such as random measurement error, flow field non-uniformity and model/instrumentation asymmetries were successfully evaluated, which were necessary for the validation of the CFD models.

Similarly, Beresh (2009) performed a comparison among the PIV results from multiple experimental configurations and data processing techniques to quantify the uncertainties associated with the selection of the experimental setup and processing parameters. The data were acquired in the far-field of the interaction between a transverse supersonic jet and a transonic crossflow. The experimental configurations included two-component PIV in the centerline stream-wise plane at two overlapping stations, as well as stereoscopic PIV in both the same stream-wise plane and in the cross plane. Beresh (2009) demonstrated that the bias errors related to calibration and window deformation, which were nontrivial to predict beforehand, dominated the results in the turbulent flow region. This comparison between different PIV configurations and data reduction techniques thus suggests that state-of-the-art methods of uncertainty quantification may not fully capture all error sources in PIV measurements.

The discussion above shows that the DOE is a valuable tool for quantifying the complete uncertainty (both random and systematic components) of flow measurements, and the contribution of the experimental factors to the uncertainty. In PIV, UQ methods have been proposed that mainly focused on the random uncertainty, which can be retrieved from the data statistics. Approaches based on the error sampling method or comparisons of different

PIV measurements at the same locations showed that PIV uncertainties are potentially significantly larger than those predicted by conventional PIV-UQ approaches because of the presence of systematic error sources. Hence, in this paper, we propose a PIV-UQ approach based on DOE and Analysis of Variances (ANOVA) where the significant experimental factors can be identified along with the systematic uncertainties arising from them. The proposed approach does not aim to replace the established PIV-UQ methodologies such as correlation statistics approach (Wieneke 2015), particle disparity method (Sciacchitano et al. 2013), uncertainty surface method (Timmins et al. 2012), cross-correlation peak ratio criterion (Charonko and Vlachos 2013), etc. Rather, it is complementary to them. In fact, these established PIV-UQ methodologies quantify the uncertainty of instantaneous velocity fields, whereas the proposed DOE approach evaluates the uncertainty of statistical flow properties such as time-averaged velocity and Reynolds stresses. Although the DOE approach and the peak ratio and uncertainty surface methods all require the selection of relevant error sources or experimental factors, there is a fundamental difference among these methods: the latter two methods evaluate the uncertainty associated only with the selected error sources. Instead, in the DOE approach, the uncertainty that is not ascribed to the selected experimental factors is evaluated and appears in error term ε (effects of unknown factors) as explained in section 6.2. As the proposed approach allows to evaluate the uncertainty of systematic error sources and to quantify their contributions to the total uncertainty, it can be used to optimize experiments and minimize the overall uncertainty. Moreover, the approach is comprehensive in that it can be applied universally, irrespective of the kind of PIV setup, e.g. planar PIV, tomographic PTV, large scale PIV or microscopic PTV, for uncertainty quantification in any of the measured quantities, e.g. mean velocity or higher order statistics. The proposed methodology is described in section 6.2. The approach is experimentally assessed for planar PIV measurements of the flow over a NACA0012 airfoil in a wind tunnel. The experimental setup and results of the uncertainty quantification in mean velocity and Reynolds stress are presented in section 6.3. Moreover, the methodology is applied to a stereoscopic PIV experiment

dealing with the flow at the outlet of a ducted BLI propulsor. The results of this application are briefly shown in section 6.4.

## 6.2. Design of Experiments and Analysis of Variances

DOE refers to the process of planning the experiment in order to collect appropriate data that can be analyzed by statistical methods resulting in valid and objective conclusions (Montgomery 2013). In any experiment, some of the experimental parameters directly affect the output value and are called *design factors*; in PIV measurements, those are for instance the inter-frame time separation, interrogation window size, camera aperture, laser sheet thickness, etc. Additionally, some of the parameters, which affect the output directly or indirectly (in combination with the design factors) but are uncontrollable (or only partly controllable) during the measurements, are called *nuisance factors*; for PIV, those include variations of the fluid properties during a measurement, seeding density and its distribution, etc. Different measurements of an ideally constant quantity with varying levels of the design and/or nuisance factors show variations in the measured quantity. A proper data acquisition model and statistical analysis can be used to quantify the variance in the output quantity due to the variations in the levels of input factors (and their combinations).

The present work employs the statistical tools DOE and ANOVA to quantify the total uncertainty and the contribution of the design and nuisance factors to the total uncertainty. Following Montgomery (2013), a Randomized Complete Block Design (RCBD) is considered for data acquisition, as *blocking* is necessary for tackling the effect of the nuisance factors; in such experimental design, measurements are carried out in two or more blocks (or levels of the nuisance factor) and levels of the design factors are varied randomly in each block. The analysis can be performed by choosing as many factors as one is interested in. However, the number of measurement runs increases with the number of factors and their levels as $L^N$, being $N$ the number of experimental factors and $L$ the number of levels of each factor (assumed to be the same for all factors). Let us take an example of experiment with two design factors $A$ and $B$ with $a$ and $b$ number of levels,

respectively, and one blocking factor with $n$ number of levels. Following Montgomery (2013), a linear statistical model for this design is:

$$y_{ijk} = \mu + A_i + B_j + (AB)_{ij} + Block_k + \varepsilon_{ijk} \tag{6.1}$$

where, $y_{ijk}$ is the observed response at the $i^{th}$ level of factor $A$ and $j^{th}$ level of factor $B$ in $k^{th}$ block , $\mu$ is the overall mean effect, $A_i$ is the effect of the $i^{th}$ level of factor $A$, $B_j$ is the effect of the $j^{th}$ level of factor $B$, $(AB)_{ij}$ is the effect of the interaction between $A_i$ and $B_j$, $Block_k$ is the effect of the $k^{th}$ level of the blocking factor, and $\varepsilon_{ijk}$ is an error component consisting of random error and the effect of unknown factors in the measurements. For this model, we are interested in checking whether the effects $A_i$, $B_j$, $(AB)_{ij}$ and $Block_k$ are zero (null hypothesis) or non-zero (alternative hypothesis). This can be achieved by the factorial ANOVA (Montgomery 2013) as shown in table 6.1, where $y_{i..}$ denotes the total of all observations under the $i^{th}$ level of factor $A$, $y_{.j.}$ denotes the total of all observations under the $j^{th}$ level of factor $B$, $y_{ij.}$ denotes the total of all observations under the $i^{th}$ level of factor $A$ and $j^{th}$ level of factor $B$, $y_{..k}$ denotes the total of all observations under the $k^{th}$ level of blocking factor, and $y_{...}$ denotes the grand total of all the observations. These terms can be expressed mathematically as:

$$y_{i..} = \sum_{j=1}^{b}\sum_{k=1}^{n} y_{ijk}\,, \qquad y_{.j.} = \sum_{i=1}^{a}\sum_{k=1}^{n} y_{ijk}\,, \qquad y_{ij.} = \sum_{k=1}^{n} y_{ijk},$$

$$y_{..k} = \sum_{i=1}^{a}\sum_{j=1}^{b} y_{ijk}\,, \qquad y_{...} = \sum_{i=1}^{a}\sum_{j=1}^{b}\sum_{k=1}^{n} y_{ijk} \tag{6.2}$$

From ANOVA table 6.1, the significance of the factor effects is determined by performing $F$-test with desired confidence level, where the $F_0$ values are computed as the ratios of the mean squares ($MS$) of the effects to the error mean square ($MS_\varepsilon$). The $F_0$ values are then compared with a critical value $F_c$ based on the desired confidence level and degrees of freedom of the factors.

If the $F_0$ value is greater than $F_c$, then the corresponding effect is statistically significant with the desired level of confidence, and the null hypothesis shall be rejected. The reader is referred to any standard book on statistics for a detailed explanation of the *F*-test (for example, Montgomery 2013). It is thus possible to segregate the contribution of every factor in the total variance of the measurement.

Table 6.1. Analysis of Variances (ANOVA) table for Two-Factor Randomized Complete Block Design (RCBD)

| Source | Sum of Squares | Degrees of Freedom | Mean Squares | $F_0$ |
|---|---|---|---|---|
| $A$ | $SS_A = \frac{1}{bn}\sum_{i=1}^{a} y_{i..}^2 - \frac{y_{...}^2}{abn}$ | $a-1$ | $MS_A = \frac{SS_A}{a-1}$ | $F_0 = \frac{MS_A}{MS_\varepsilon}$ |
| $B$ | $SS_B = \frac{1}{an}\sum_{j=1}^{b} y_{.j.}^2 - \frac{y_{...}^2}{abn}$ | $b-1$ | $MS_B = \frac{SS_B}{b-1}$ | $F_0 = \frac{MS_B}{MS_\varepsilon}$ |
| $AB$ | $SS_{AB} = \frac{1}{n}\sum_{i=1}^{a}\sum_{j=1}^{b} y_{ij.}^2 - \frac{y_{...}^2}{abn} - SS_A - SS_B$ | $(a-1)(b-1)$ | $MS_{AB} = \frac{SS_{AB}}{(a-1)(b-1)}$ | $F_0 = \frac{MS_{AB}}{MS_\varepsilon}$ |
| Block | $SS_{Block} = \frac{1}{ab}\sum_{k=1}^{n} y_{..k}^2 - \frac{y_{...}^2}{abn}$ | $n-1$ | $MS_{Block} = \frac{SS_{Block}}{n-1}$ | $F_0 = \frac{MS_{Bloc}}{MS_\varepsilon}$ |
| ε | $SS_\varepsilon = SS_{Total} - SS_A - SS_B - SS_{AB} - SS_{Block}$ | $(ab-1)(n-1)$ | $MS_\varepsilon = \frac{SS_\varepsilon}{(ab-1)(n-1)}$ | |
| Total | $SS_{Total} = \sum_{i=1}^{a}\sum_{j=1}^{b}\sum_{k=1}^{n} y_{ijk}^2 - \frac{y_{...}^2}{abn}$ | $abn-1$ | $MS_{Total} = \frac{SS_{Total}}{abn-1}$ | |

The total uncertainty ($U_{Total}$) and constituent systematic uncertainties ($U_X$) in the response variable are calculated as:

$$U_{Total} = \sqrt{\frac{SS_{Total}}{abn-1}} = \sqrt{U_A^2 + U_B^2 + U_{AB}^2 + U_{Block}^2 + U_\varepsilon^2} \tag{6.3}$$

$$U_X = \sqrt{\frac{SS_X}{abn-1}} \quad and \quad X = A, B, AB, Block, \varepsilon \tag{6.4}$$

where *SS* is the sum of squares and represents the variability in the response variable as shown in the table 6.1.

## 6.3. Experimental assessment

The proposed methodology was assessed for planar PIV measurements of the flow over a NACA0012 airfoil at 15 degrees angle of attack. For sake of limiting the times for data acquisition and processing, we considered only four design factors, namely camera aperture, inter-frame time separation, interrogation window size, laser sheet thickness and one blocking factor of seeding density. The total uncertainties as well as the constituent systematic uncertainties due to the five factors were quantified for the measured time-averaged velocity and Reynolds stress.

### 6.3.1. Experimental setup

The planar PIV measurements were performed for the flow over a NACA0012 airfoil where the experimental setup was similar to that of the measurements conducted in section 5.4 of this thesis. Figure 6.1 illustrates a schematic of the experimental setup. The seeding particles were illuminated by a Quantel Evergreen 200 laser (Nd:YAG, pulse energy of 200 mJ per pulse, wavelength of 532 nm) and images were recorded with a LaVision Imager sCMOS camera (12 bits, 6.5 µm pixel size, 2560 × 2160 pixels maximum resolution) with image sensor cropped to 2240 ×1622 pixels. The camera

was equipped with a Nikon objective of 105 mm focal length and a field of view (*FOV*) of 135 mm × 98 mm was imaged with optical magnification of 0.11.

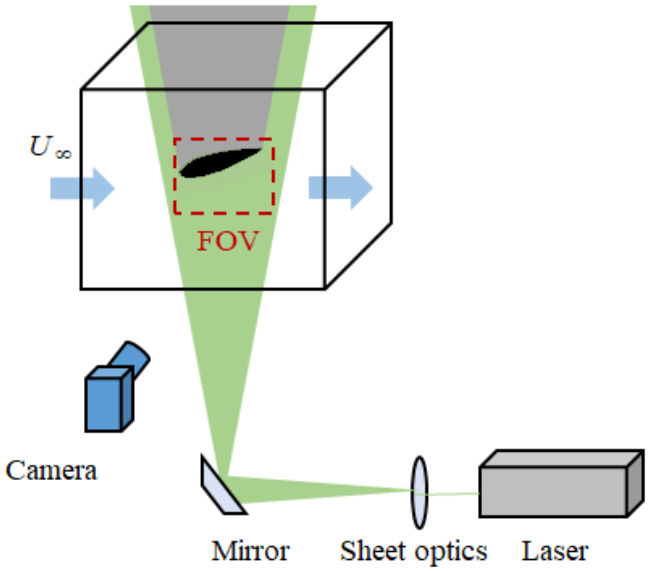


Figure 6.1. Schematic experimental setup of the planar PIV measurements of the flow over a NACA0012 airfoil at 15 degrees angle of attack

The aim of this experimental assessment was to employ the statistical tools DOE and ANOVA to quantify the total uncertainty in time-averaged PIV measurements and the contribution of the design and nuisance factors to the total uncertainty. Various factors during the acquisition and processing stages contribute to the total uncertainty. However, only some of the most important ones are considered for the analysis. Following Scharnowski et al. (2019b), five factors, namely camera aperture (*f#*), inter-frame time separation ($\Delta t$), interrogation window size ($D_I$), laser sheet thickness ($\Delta z$) and seeding density were considered to be the most relevant. Therefore, for the analysis four design factors *f#*, $\Delta t$, $D_I$, $\Delta z$ (assigned with *A*, *B*, *C*, *D*, respectively) and a blocking factor (seeding density) with two levels of each were selected. The two levels of the factors are: *f#* = 4 and 8, $\Delta t$ = 50 and 70 µs [resulting displacements in the free stream ($U_\infty$ = 10 m/s) are 8.5 and

11.8 pixels, respectively], $D_I = 16 \times 16$ and $64 \times 64$ pixels ($0.95 \times 0.95$ and $3.78 \times 3.78$ mm in physical units), $\Delta z = 1$ and 3 mm, and seeding density = 0.01-0.02 and 0.08-0.09 ppp (resulting in mean particle distances of 0.2 and 0.5 mm, respectively), as summarised in table 6.2.

Table 6.2. Factors and their levels in the planar PIV measurements of the flow over a NACA0012 airfoil

| Factor | Parameter | Levels |
|---|---|---|
| A | $f\#$ | 4, 8 |
| B | $\Delta t$ | 50, 70 μs |
| C | $D_I$ | $16 \times 16$, $64 \times 64$ pixels ($0.95 \times 0.95$, $3.78 \times 3.78$ mm) |
| D | $\Delta z$ | 1, 3 mm |
| Block | seeding density | 0.01-0.02, 0.08-0.09 ppp (mean particle distances of 0.2 and 0.5 mm) |

Following the $2^N$ rule, $N$ being the number of design factors, a total of 32 measurements were performed ($2^4 = 16$ in each block). The images were recorded and processed using LaVision Davis10 software. The data set at each run consisted of 1000 double-frame images and a total of 16 runs per block were performed in a random order. Each measurement run was unique corresponding to the combination of one of the two levels of the four design factors. The processing was done using Gaussian interrogation windows of $128 \times 128$ pixels with 75% overlap for the initial passes and $16 \times 16$ pixels or $64 \times 64$ pixels with 75% overlap for the final passes.

The estimated time-averaged stream-wise velocity component $u$ and in-plane velocity vectors are shown in figure 6.2; the measured Reynolds

normal stresses $R_{uu}$ are shown in figure 6.3. It is to be noted that figures 6.2 and 6.3 show the values averaged over all 32 measurement runs.

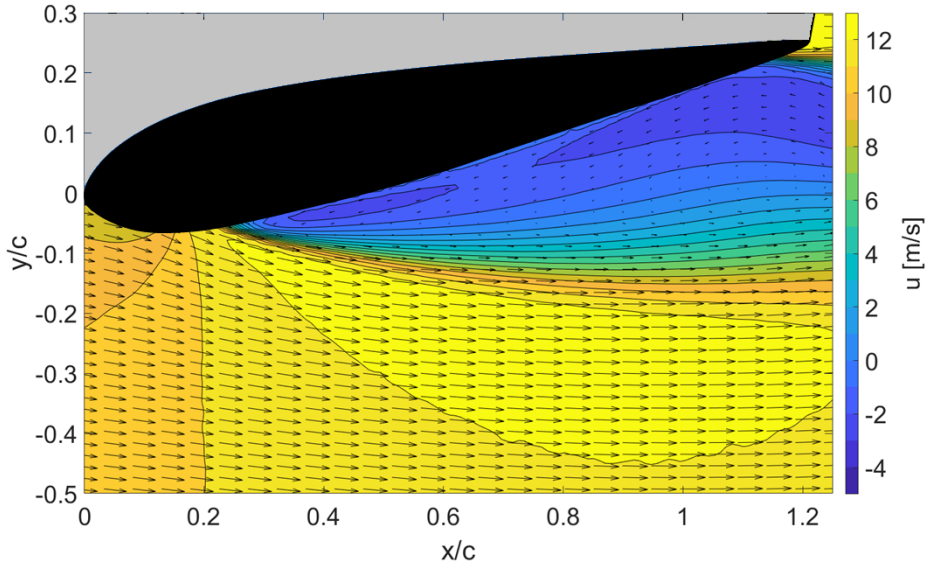


Figure 6.2. Measured time-averaged stream-wise velocity component $u$ and in-plane velocity vectors (averaged over 32 measurement runs)

It is clear that the flow has varying degrees of fluctuations, e.g. low fluctuations in the potential flow region ($0.01 < R_{uu} < 0.1$ m²/s²) and relatively high fluctuations in the separated shear layer and the turbulent wake ($5 < R_{uu} < 8$ m²/s²). Therefore, the measured flow field is a suitable case to implement and assess the feasibility of the proposed approach in a range of flow conditions encountered in typical PIV measurements. The analysis was performed for the whole *FOV* to quantify the total uncertainties in the time-averaged velocities and Reynold stresses and the contribution of the individual factors to the total uncertainties. However, for simplicity, two points were chosen in two different regions based on the amount of flow fluctuations, as shown in figure 6.3, to explain the contribution of the factors to the total uncertainties. The results at these two points are explained in detail in section 6.3.2.

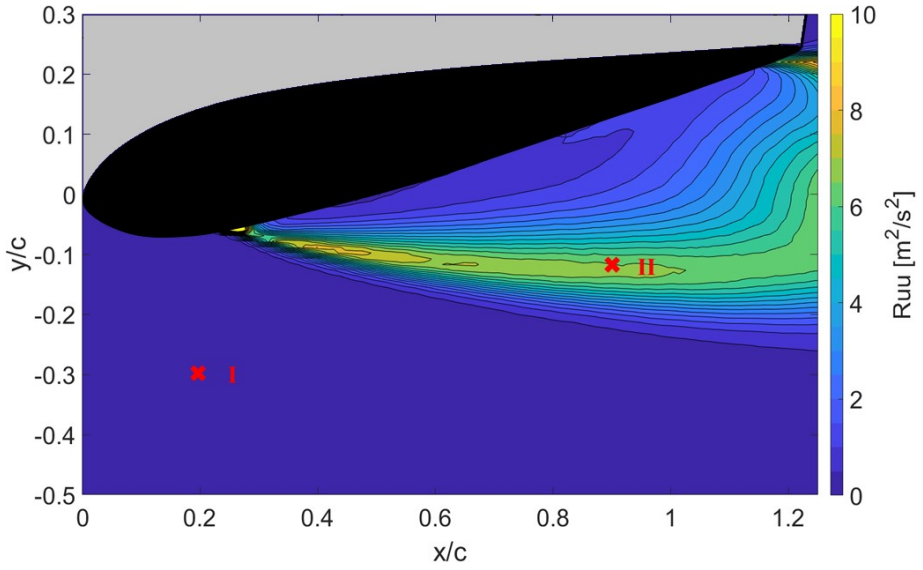


Figure 6.3. Reynolds normal stresses averaged over 32 measurement runs (The results of application of the proposed approach are shown in detail in section 6.3.2 at points I and II)

### 6.3.2. Results

#### 6.3.2.1. Uncertainty of mean velocity

The total uncertainties of the mean or time-averaged stream-wise velocities were calculated following equation (6.3) and are shown in figure 6.4(a). As expected, the uncertainties estimated by the DOE approach are higher than the random uncertainties calculated from data statistics for a specific run (the considered case is: $f\# = 8$, $\Delta t = 50$ µs, $D_I = 16 \times 16$ pixels, $\Delta z = 1$ mm and seeding density = 0.08-0.09 ppp) as $\sigma/\sqrt{N_s}$ [see figure 6.4(b)], with $\sigma$ the standard deviation and $N_s$ the number of samples (Sciacchitano and Wieneke, 2016). It is clear that the random uncertainties from data statistics are underestimated as the systematic effects of the experimental factors are not taken into consideration. The methodology based on DOE, on the other hand, is able to compute the systematic contributions of the factors considered in the analysis to the total uncertainty. Nevertheless, the random

uncertainty of the mean velocity is proportional to the flow fluctuations or Reynolds stress values. Moreover, larger total uncertainty is retrieved in the regions of high velocity gradients, as reported by Scarano (2002), which are mainly encountered in the shear layer. Following these observations, a detailed analysis of the constituent systematic uncertainties is made at points I and II, located in the potential flow region and turbulent region, respectively (see figure 6.3).

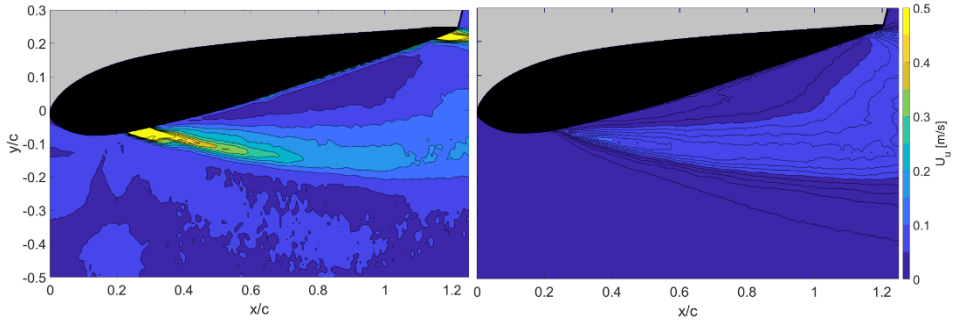


(a) total uncertainty by proposed methodology based on DOE

(b) random uncertainty from data statistics ($\sigma/\sqrt{N_s}$)

Figure 6.4. Uncertainty in time-averaged stream-wise velocity $u$

The ANOVA results at the two selected points were obtained in the form of table 6.3, where the $F_0$ values corresponding to the main and interaction effects of the design and blocking factors are calculated as shown in the last column in table 6.1. The $F$-test is then performed to estimate whether the effects are statistically significant or not, which is done by comparing the $F_0$ values with the critical value $F_c$ that, in the present case (for 1 degree of freedom of numerator and 20 degrees of freedom of denominator), is 4.35 for 95% confidence level (Montgomery 2013). If the $F_0$ value is greater than $F_c$, then the corresponding effect is statistically significant with the desired level of confidence. For example, for the point I, the main effect of factor $B$ (i.e. $\Delta t$) is statistically significant as it yields an $F_0$ value of 40.17. Instead, at point II, where the flow fluctuations are larger, factor $D$ (i.e. the laser sheet

thickness $\Delta z$) has a statistically significant effect, leading to an $F_0$ value of 6.81.

Table 6.3. Analysis of Variances (ANOVA) results in the uncertainty quantification of mean stream-wise velocity $u$ where $A$, $B$, $C$, $D$ and Block correspond to the factors: camera aperture $f\#$, inter-frame time separation $\Delta t$, interrogation window size $D_I$, laser sheet thickness $\Delta z$ and seeding density, respectively [The critical value $F_c = 4.35$ for 1 degree of freedom of numerator and 20 degrees of freedom of denominator at 95% confidence level (Montgomery 2013)]

| Source | DOF | Point I | | | | Point II | | | |
|---|---|---|---|---|---|---|---|---|---|
| | | SS ($m^2/s^2$) | MS ($m^2/s^2$) | $F_0$ | $U_X$ (m/s) | SS ($m^2/s^2$) | MS ($m^2/s^2$) | $F_0$ | $U_X$ (m/s) |
| $A$ ($f\#$) | 1 | 0.0026 | 0.0026 | 3.98 | 0.0092 | 0.0000 | 0.0000 | 0.00 | 0.0008 |
| $B$ ($\Delta t$) | 1 | 0.0264 | 0.0264 | **40.17** | 0.0292 | 0.0006 | 0.0006 | 0.04 | 0.0042 |
| $C$ ($D_I$) | 1 | 0.0000 | 0.0000 | 0.06 | 0.0011 | 0.0099 | 0.0099 | 0.68 | 0.0178 |
| $D$ ($\Delta z$) | 1 | 0.0003 | 0.0003 | 0.40 | 0.0029 | 0.0995 | 0.0995 | **6.81** | 0.0566 |
| $AB$ | 1 | 0.0028 | 0.0028 | 4.27 | 0.0095 | 0.0017 | 0.0017 | 0.12 | 0.0074 |
| $AC$ | 1 | 0.0000 | 0.0000 | 0.00 | 0.0002 | 0.0034 | 0.0034 | 0.23 | 0.0104 |
| $AD$ | 1 | 0.0000 | 0.0000 | 0.01 | 0.0004 | 0.0241 | 0.0241 | 1.65 | 0.0279 |
| $BC$ | 1 | 0.0000 | 0.0000 | 0.01 | 0.0005 | 0.0016 | 0.0016 | 0.11 | 0.0071 |
| $BD$ | 1 | 0.0002 | 0.0002 | 0.34 | 0.0027 | 0.0000 | 0.0000 | 0.00 | 0.0005 |
| $CD$ | 1 | 0.0000 | 0.0000 | 0.01 | 0.0005 | 0.0039 | 0.0039 | 0.27 | 0.0112 |
| Block | 1 | 0.0246 | 0.0246 | **37.38** | 0.0282 | 0.1896 | 0.1896 | **12.99** | 0.0782 |
| ε | 20 | 0.0131 | 0.0007 | - | 0.0206 | 0.2921 | 0.0146 | - | 0.0971 |
| Total | 31 | 0.0701 | 0.0023 | - | 0.0476 | 0.6262 | 0.0202 | - | 0.1421 |

At both points I and II, as in most of the measurement domain, the effect of the seeding density (block) is statistically significant, because it directly affects the valid detection probability as reported by Scharnowski et al. (2019b). Instead, the other experimental factors (factors A, C and D at point I; factors A, B, C at point II) as well as the interaction effects between the factors do not have a statistically significant effect on the total uncertainty.

The constituent uncertainties due to the main and interaction effects of the factors were calculated by equation (6.4) and are reported in the last column of table 6.3. Their contributions to the total uncertainty in the stream-wise velocity $u$ are shown in the form of pie charts in figure 6.5. It is to be noted that the percentage contributions were calculated for the squares of the individual uncertainties as they add to the square of the total uncertainty [see equation (6.3)]. The sub-figures (a) and (b) are for the points I and II, respectively, which are marked in figure 6.3. The mean stream-wise velocity ($u$) components at these points are 11.02 m/s and 4.58 m/s, respectively. The corresponding total uncertainties are 0.05 m/s and 0.14 m/s, which are shown in the centre of the pie charts in figure 6.5.

It is clear that the total uncertainty increases with increase in the velocity gradient and the flow fluctuations, which agrees with the observation in the contour plot of total uncertainty in figure 6.4. The seeding density (block) contributes to around 35% and 30% to the total uncertainty in the time-averaged stream-wise velocity at the points I and II, respectively. The factor $B$, i.e. inter-frame time separation $\Delta t$, is the most significant factor at point I and contributes to 38% of the total uncertainty. At this point, where the flow fluctuations are very low and the mean velocity is largely affected by peak-locking errors, the factor $\Delta t$ influences directly the magnitude of peak-locking errors the most, as observed by Legrand et al. (2012).

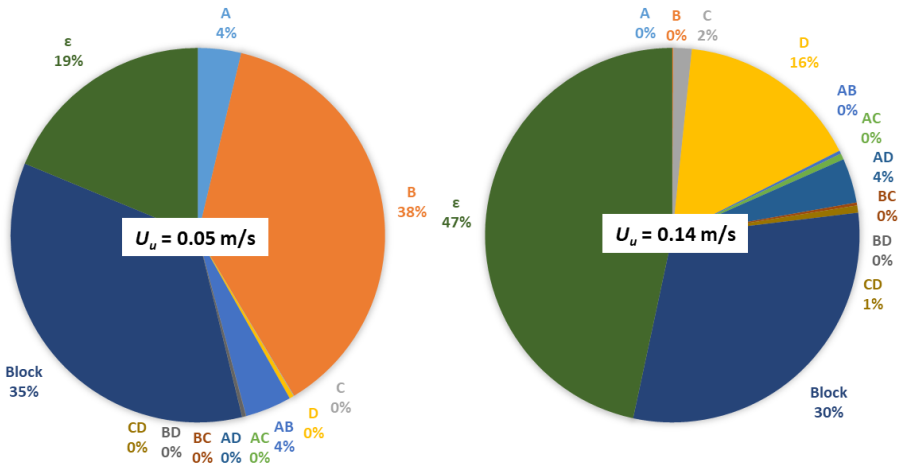


(a) Point I (potential flow region) (b) Point II (turbulent region)

Figure 6.5. Contribution of systematic uncertainties to the total uncertainty in time-averaged stream-wise velocity at the two points marked in the figure 6.3, due to main and interaction effects of the factors: $A$ (camera aperture $f\#$), $B$ (inter-frame time separation $\Delta t$), $C$ (interrogation window size $D_I$), $D$ (laser sheet thickness $\Delta z$) and block of seeding density

At the point II, i.e. in the flow region of high flow fluctuations, apart from the seeding density, the factor $D$ i.e. laser sheet thickness $\Delta z$ is statistically significant and contributes to 16% of the total uncertainty of the time-averaged stream-wise velocity as shown in the pie chart in figure 6.5(b). This is due to the three-dimensional nature of the flow in the turbulent region of the flow, thus the larger value of $\Delta z$ may cause a larger dispersion of the particles displacements within the interrogation window. Moreover, the random error (factors not directly considered in the analysis, e.g. limited statistical convergence, image noise, etc.) shows significant contribution of 47% to the total uncertainty. This is due to the flow fluctuations in these regions being high which, owed to the limited statistical convergence of the measurements, makes it difficult to segregate the contribution of individual systematic uncertainties. It is to be noted that the "*error uncertainty* ε" from the ANOVA represents the random uncertainty in the measurements plus the uncertainty due to the unknown experimental factors (i.e. the factors not

considered as design or blocking factors). The effect of the factor $C$ (interrogation window size $D_I$) is not statistically significant at the points I and II. However, in high-shear regions of the flow, it contributes significantly to the total uncertainty of the mean stream-wise velocity (the results are not shown for conciseness).

### 6.3.2.2. Uncertainty of Reynolds stress

The proposed methodology was also applied for uncertainty quantification of the higher order statistics such as the Reynolds stresses. The equations (6.3) and (6.4) were used to calculate the total uncertainty and the constituent systematic uncertainties, respectively. The estimated total uncertainties of the Reynolds normal stresses are shown in figure 6.6(a).

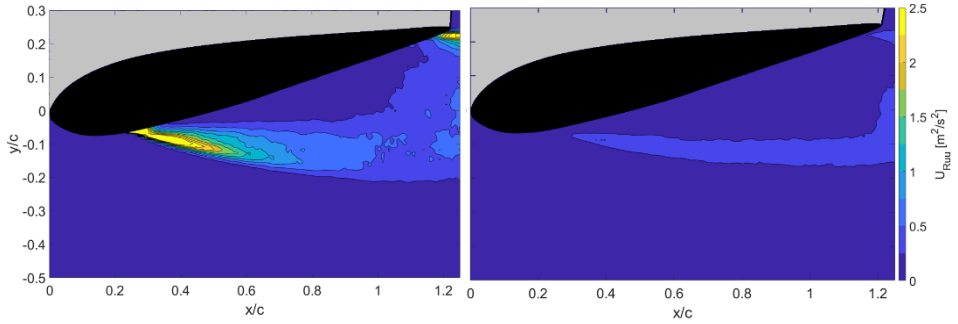


(a) total uncertainty by proposed methodology based on DOE

(b) random uncertainty from data statistics ($R_{uu}\sqrt{\frac{2}{N_s-1}}$)

Figure 6.6. Uncertainty in Reynolds normal stress $R_{uu}$

As seen for the total uncertainty of the mean stream-wise velocity, also the total uncertainties of the Reynolds normal stresses are the highest in the regions of high flow fluctuations. These total uncertainties estimated by the proposed DOE approach are compared to random uncertainties calculated from data statistics. Figure 6.6(b) shows the random uncertainties in a single run ($f\# = 8$, $\Delta t = 50$ µs, $D_I = 16 \times 16$ pixels, $\Delta z = 1$ mm and seeding density

= 0.08-0.09 ppp) calculated as $R_{uu}\sqrt{\frac{2}{N_s-1}}$, with $R_{uu}$ the Reynolds normal stress and $N_s$ the number of samples (Sciacchitano and Wieneke, 2016). It is clear that the random uncertainties are highly underestimated as the systematic effects of the experimental factors are not taken into consideration, as was also shown for the uncertainty of mean velocity in section 6.3.2.1.

Two points in two flow regions were selected as marked in figure 6.3 to evaluate the results for the constituent systematic uncertainties based on the amount of flow fluctuations. The results of ANOVA tests for these two points can be seen in table 6.4, and the pie charts in figure 6.7 show the contribution of the main and interaction effects of the design and blocking factors to the total uncertainty.

The average Reynolds normal stresses at the points I and II are 0.01 and 5.99 $m^2/s^2$, respectively, and the corresponding total uncertainties are 0.008 and 0.65 $m^2/s^2$, which are shown in the centre of pie charts in figure 6.7. It is clear that the total uncertainty increases with increase in the flow fluctuations, which agrees with the observation in the contour plot of total uncertainty in figure 6.6. In most of the measurement domain, the main effects of the factor $C$ (interrogation window size $D_I$) and the seeding density (block) are statistically significant, whereas all the two-way interaction effects are found to be insignificant, as also observed in the measurement of the mean stream-wise velocities. The seeding density directly affects the valid detection probability (Scharnowski et al. 2019b) and thus has a significant effect on the measurement uncertainty. It contributes to around 7% and 11% of the total uncertainty in the Reynolds normal stress at the points I and II, respectively. As shown in table 6.4 and figure 6.7, the factor $C$ interrogation window size $D_I$ is the most significant at both the points and contributes to 53% and 78% of the total uncertainty at the points I and II, respectively. Moreover, the factors $B$ and $D$, i.e. inter-frame time separation $\Delta t$ and laser sheet thickness $\Delta z$, are also statistically significant at the point I in the potential flow region. They contribute to 8% and 9% of the total uncertainty, respectively.

Table 6.4. Analysis of Variances (ANOVA) results in the uncertainty quantification of Reynolds normal stress $R_{uu}$ where $A$, $B$, $C$, $D$ and Block correspond to the factors: camera aperture $f\#$, inter-frame time separation $\Delta t$, interrogation window size $D_I$, laser sheet thickness $\Delta z$ and seeding density, respectively [The critical value $F_c = 4.35$ for 1 degree of freedom of numerator and 20 degrees of freedom of denominator at 95% confidence level (Montgomery 2013)]

| Source | DOF | Point I | | | | Point II | | | |
|---|---|---|---|---|---|---|---|---|---|
| | | SS ($m^4/s^4$) | MS ($m^4/s^4$) | $F_0$ | $U_X$ ($m^2/s^2$) | SS ($m^4/s^4$) | MS ($m^4/s^4$) | $F_0$ | $U_X$ ($m^2/s^2$) |
| $A$ ($f\#$) | 1 | 0.0000 | 0.0000 | 1.26 | 0.0008 | 0.0038 | 0.0038 | 0.07 | 0.0111 |
| $B$ ($\Delta t$) | 1 | 0.0002 | 0.0002 | **8.62** | 0.0022 | 0.1849 | 0.1849 | 3.57 | 0.0772 |
| $C$ ($D_I$) | 1 | 0.0010 | 0.0010 | **58.20** | 0.0057 | 9.9625 | 9.9625 | **192.17** | 0.5669 |
| $D$ ($\Delta z$) | 1 | 0.0002 | 0.0002 | **9.60** | 0.0023 | 0.1418 | 0.1418 | 2.73 | 0.0676 |
| $AB$ | 1 | 0.0000 | 0.0000 | 0.37 | 0.0005 | 0.0002 | 0.0002 | 0.00 | 0.0026 |
| $AC$ | 1 | 0.0000 | 0.0000 | 0.90 | 0.0007 | 0.0069 | 0.0069 | 0.13 | 0.0149 |
| $AD$ | 1 | 0.0000 | 0.0000 | 0.49 | 0.0005 | 0.0000 | 0.0000 | 0.00 | 0.0004 |
| $BC$ | 1 | 0.0000 | 0.0000 | 0.67 | 0.0006 | 0.0339 | 0.3394 | 0.65 | 0.0331 |
| $BD$ | 1 | 0.0000 | 0.0000 | 0.75 | 0.0006 | 0.0442 | 0.0442 | 0.85 | 0.0378 |
| $CD$ | 1 | 0.0000 | 0.0000 | 0.74 | 0.0007 | 0.0178 | 0.0178 | 0.34 | 0.0240 |
| Block | 1 | 0.0001 | 0.0001 | **8.04** | 0.0021 | 1.3195 | 1.3195 | **25.45** | 0.2063 |
| ε | 20 | 0.0003 | 0.0000 | - | 0.0034 | 1.0368 | 0.0518 | - | 0.1829 |
| Total | 31 | 0.0021 | 0.0001 | - | 0.0083 | 13.0577 | 0.4212 | - | 0.6490 |

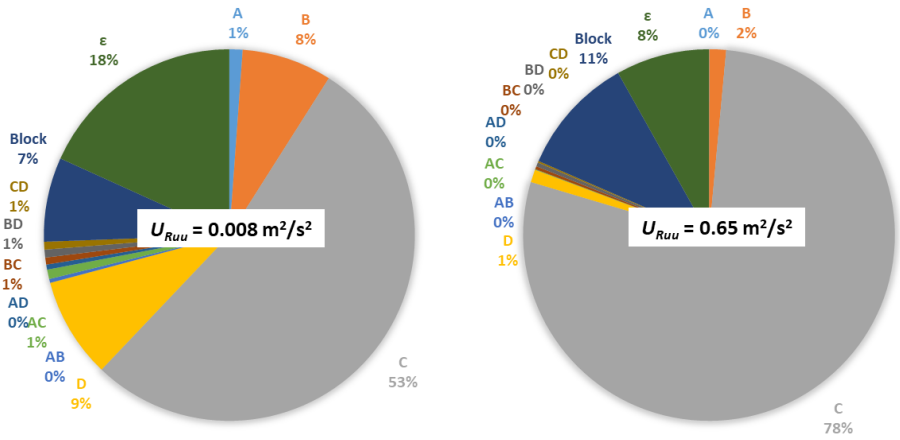


(a) Point I (potential flow region) (b) Point II (turbulent region)

Figure 6.7. Contribution of systematic uncertainties to the total uncertainty in Reynolds normal stress at the two points marked in the figure 6.3, due to main and interaction effects of the factors- $A$ (camera aperture $f\#$), $B$ (inter-frame time separation $\Delta t$), $C$ (interrogation window size $D_i$), $D$ (laser sheet thickness $\Delta z$) and block of seeding density

## 6.4. Application to boundary layer ingesting propulsor flow

The proposed methodology was applied on a wind tunnel experiment of a ducted Boundary Layer Ingesting (BLI) propulsor.

### 6.4.1. Experimental setup

The experiment was conducted in the Low-Speed Tunnel (LST) operated by the German-Dutch Wind Tunnels (DNW). The measurements were performed at a Mach number of 0.174 and a body length-based Reynolds number of $6\times10^6$ corresponding to a freestream velocity ($U_\infty$) of 60 m/s. The test case consisted of an axisymmetric body placed upstream of the propulsor as shown in figure 6.8, where stereoscopic PIV measurements were performed in a cross plane at the outlet of the propulsor.

## 6. Design of Experiments (DOE) for PIV Uncertainty Quantification

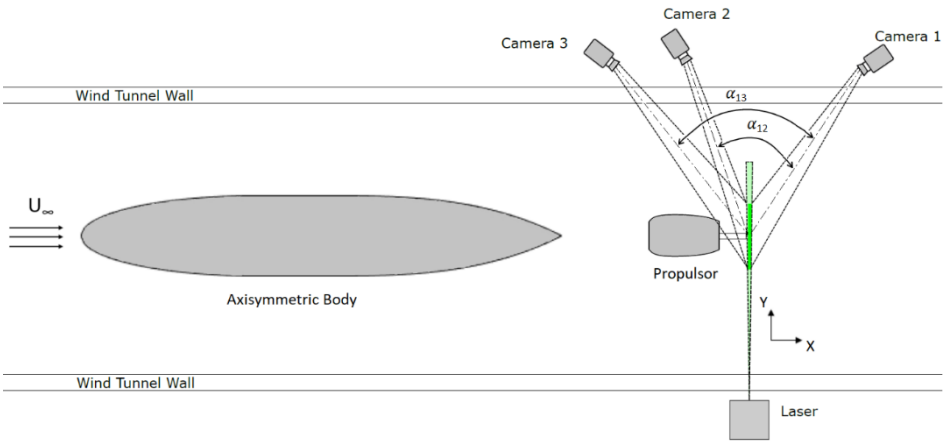


Figure 6.8. Schematic experimental setup of stereoscopic PIV measurements at the outlet of the ducted Boundary Layer Ingesting (BLI) propulsor

In this experimental campaign, we employed the statistical tools DOE and ANOVA to quantify the total uncertainty in time-averaged velocities and the contribution of the design and nuisance factors to the total uncertainty. Following Sciacchitano (2019) and Bhattacharya et al (2016), among others, three design factors, namely camera aperture ($f\#$), inter-frame time separation ($\Delta t$) and interrogation window size ($D_I$), assigned with $A$, $B$, $C$, respectively, and one blocking factor of stereoscopic camera angle ($\alpha$) were selected for the analysis. Two measurement levels were considered for each factor, which are reported in table 6.5. Following the $2^N$ rule, $N$ being the number of design factors, a total of 16 measurements were performed ($2^3 = 8$ in each block).

Three LaVision Imager sCMOS cameras were used to perform the measurements with two different stereoscopic angles (i.e. in two blocks). The cameras 1 and 2 formed the stereoscopic angle ($\alpha_{12}$) of 44° and were considered to be the block I, whereas the cameras 1 and 3 formed the stereoscopic angle ($\alpha_{13}$) of 54° and were considered to be the block II. It is to be noted that stereoscopic angles larger than 60° are often employed in stereo-PIV measurements. However, in the present experiments, the camera angles were limited by limitations on the optical access. The cameras were

mounted with objective lenses of 135 mm focal length and Scheimpflug adapter. The field of view (*FOV*) obtained was 260 mm × 220 mm and the values of magnification factors averaged over the entire *FOV* for the cameras 1, 2 and 3 were 0.067, 0.073 and 0.069, respectively. The flow was seeded by an aerosol seeding generator, which produces DEHS droplets of 1 μm median diameter. The particles were illuminated by a Quantel Evergreen 200 laser (Nd:YAG, pulse energy of 200 mJ per pulse, wavelength of 532 nm) forming a sheet of 4 mm thickness. The images were recorded and processed using the LaVision Davis10 software. The data set at each run consisted of 2000 double-frame images and a total of 8 runs per block (stereoscopic camera angle) were performed in a random order. The geometric stereoscopic calibration via the pinhole model (Prasad, 2000) was followed by the self-calibration based on particle images (Wieneke 2005). The processing was done using Gaussian interrogation windows of 64 × 64 pixels with 50% overlap for the initial passes and 16 × 16 pixels or 32 × 32 pixels with 50% overlap for the final passes.

Table 6.5. Factors and their levels in the stereoscopic PIV measurements at the outlet of the ducted Boundary Layer Ingesting (BLI) propulsor

| Factor | Parameter | Levels |
|---|---|---|
| A | $f\#$ | 4, 5.6 |
| B | $\Delta t$ | 16, 20 μs |
| C | $D_I$ | 16 × 16, 32 × 32 pixels |
| Block | $\alpha$ | 44, 54 degrees |

### 6.4.2. Results

The estimated time-averaged stream-wise velocity component $u$ and in-plane (*Y-Z* plane) velocity vectors are shown in figure 6.9.

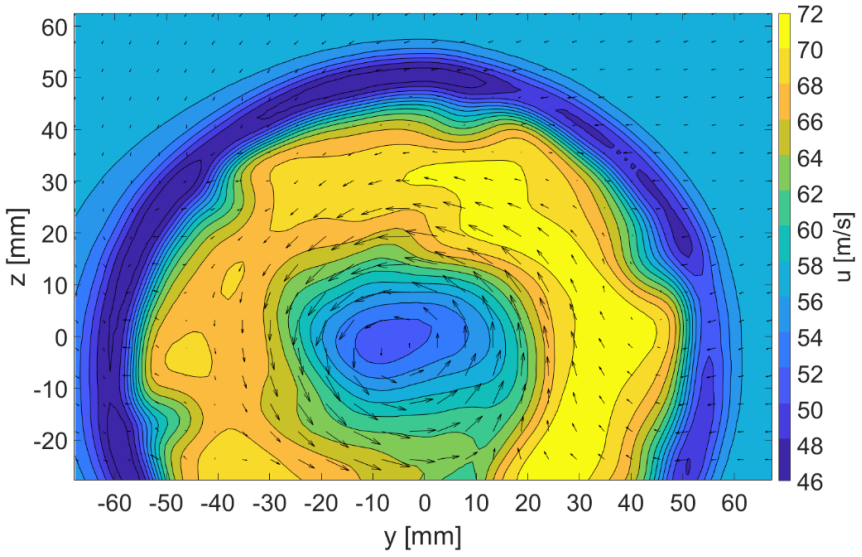


Figure 6.9. Time-averaged contour plots of the stream-wise velocity $u$ and vector plots of the in-plane ($Y$-$Z$ plane) velocity of the stereoscopic PIV measurements

The wake region can be seen in the centre of the measurement domain, whereas the outer region represents potential flow with stream-wise velocity of 60 m/s. The flow is retarded at the periphery of the propulsor and the discontinuities in the mean stream-wise velocity field due to the stator ring can be seen at the periphery. Moreover, the in-plane velocity vectors are shown in figure 6.9 illustrating the magnitude and direction of $Y$ and $Z$-velocity components $v$ and $w$, respectively. The counter-clockwise rotation of the flow in the wake of the propulsor can be easily seen due to the direction of the vectors, where the magnitudes of $v$ and $w$ velocity components are larger than those in the outer potential flow region. The contour plot of the total uncertainty ($U_u$) of the mean stream-wise velocity component $u$ is shown in figure 6.10. The total uncertainty of the mean velocity closely resembles the fluctuations root-mean-square, as was also observed in the experimental assessment with NACA0012 airfoil. Moreover, the outer edge of the propulsor slipstream exhibits larger total uncertainty due to high velocity gradients in this region.

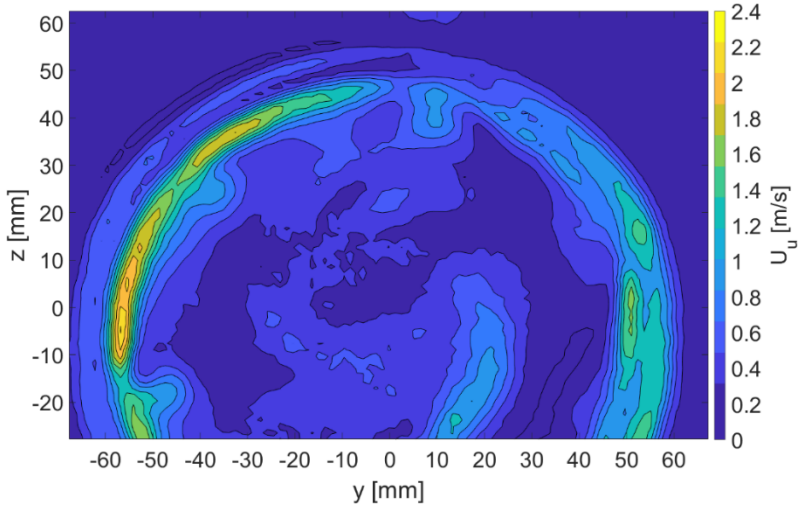


Figure 6.10. Total uncertainty in time-averaged stream-wise velocity *u* calculated by the proposed methodology

To explain the contribution of the individual factors to the total uncertainty, three points in three different flow regions were chosen based on the amount of flow fluctuations and velocity gradients, as marked in figure 6.11.

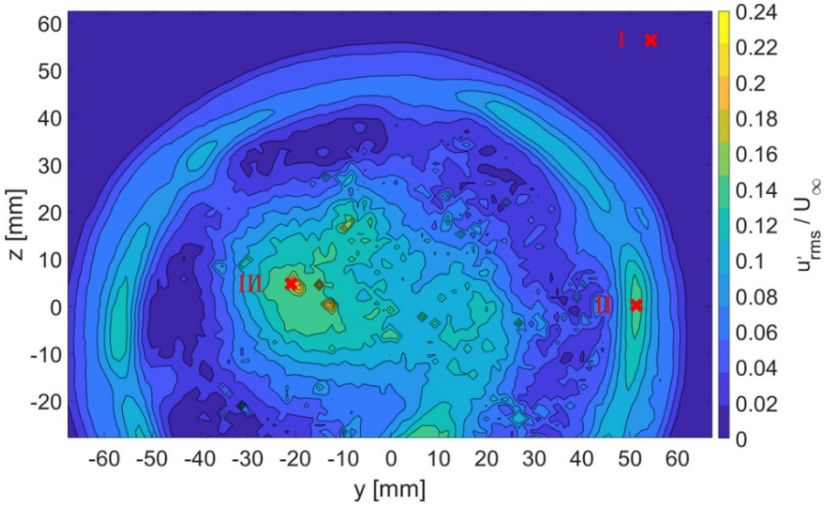


Figure 6.11. RMS of velocity fluctuations in stream-wise velocity normalized by freestream velocity

The points I, II and III correspond to the potential flow region, shear layer and jet region, respectively. The mean stream-wise velocity ($u$) components at these points are 59.20 m/s, 64.17 m/s and 59.75 m/s, respectively and the corresponding total uncertainties are 0.37 m/s, 1.60 m/s and 0.51 m/s. It is clear that the total uncertainty increases with increase in the velocity gradient and the flow fluctuations, which agrees with the observation in the contour plot of total uncertainty in figure 6.10. The ANOVA results at the three selected points can be seen in table 6.6.

Table 6.6. Analysis of Variances (ANOVA) results in the uncertainty quantification of time-averaged stream-wise velocity in the BLI propulsor experiment, where $A$, $B$, $C$ and Block correspond to the factors: camera aperture $f\#$, inter-frame time separation $\Delta t$, interrogation window size $D_I$ and stereoscopic camera angle $\alpha$, respectively [The critical value $F_c = 5.3$ for 1 degree of freedom of numerator and 8 degrees of freedom of denominator at 95% confidence level (Montgomery 2013)]

| Source | DoF | Point I | | | | Point II | | | | Point III | | | |
|---|---|---|---|---|---|---|---|---|---|---|---|---|---|
| | | SS | MS | $F_0$ | $U_X$ | SS | MS | $F_0$ | $U_X$ | SS | MS | $F_0$ | $U_X$ |
| $A$ ($f\#$) | 1 | 0.00 | 0.00 | 0.60 | 0.02 | 1.25 | 1.25 | 0.46 | 0.29 | 0.17 | 0.17 | 0.48 | 0.11 |
| $B$ ($\Delta t$) | 1 | 0.00 | 0.00 | 0.01 | 0.00 | 8.77 | 8.77 | 3.23 | 0.76 | 0.24 | 0.24 | 0.69 | 0.13 |
| $C$ ($D_I$) | 1 | 0.00 | 0.00 | 0.05 | 0.00 | 0.01 | 0.01 | 0.00 | 0.02 | 0.00 | 0.00 | 0.01 | 0.01 |
| $AB$ | 1 | 0.01 | 0.01 | 1.40 | 0.02 | 0.55 | 0.55 | 0.20 | 0.19 | 0.02 | 0.02 | 0.07 | 0.04 |
| $AC$ | 1 | 0.00 | 0.00 | 0.04 | 0.00 | 0.01 | 0.01 | 0.00 | 0.02 | 0.06 | 0.06 | 0.16 | 0.06 |
| $BC$ | 1 | 0.00 | 0.00 | 0.21 | 0.01 | 0.10 | 0.10 | 0.04 | 0.08 | 0.25 | 0.25 | 0.72 | 0.13 |
| Block | 1 | 1.95 | 1.95 | **301.65** | 0.36 | 5.86 | 5.86 | 2.16 | 0.63 | 0.39 | 0.39 | 1.14 | 0.16 |
| ε | 8 | 0.05 | 0.01 | - | 0.06 | 21.73 | 2.72 | - | 1.20 | 2.76 | 0.34 | - | 0.43 |
| Total | 15 | 2.01 | 0.13 | - | 0.37 | 38.27 | 2.55 | - | 1.60 | 3.89 | 0.26 | - | 0.51 |

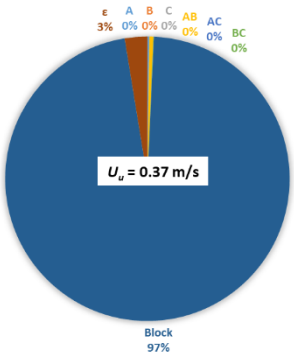


(a) Point I (potential flow region)

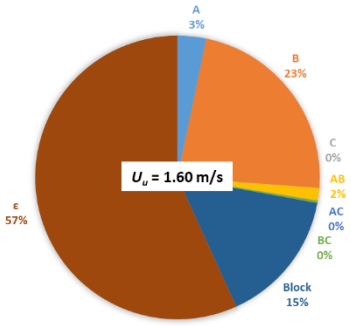


(b) Point II (shear layer)

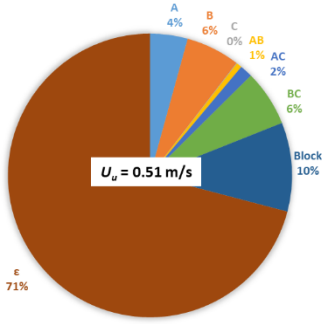


(c) Point III (wake region)

Figure 6.12. Contribution of systematic uncertainties to the total uncertainty in time-averaged stream-wise velocity at the three points marked in the figure 6.11, due to main and interaction effects of the factors- $A$ (camera aperture $f\#$), $B$ (inter-frame time separation $\Delta t$), $C$ (interrogation window size $D_I$) and block of stereoscopic camera angle $\alpha$

Moreover, the pie charts in figure 6.12 show the contributions of the main and interaction effects of the factors in the total uncertainty. It is clear from table 6.6 that the blocking factor - stereoscopic camera angle - is the most significant factor ($F_0 = 301.65$, higher than $F_c = 5.3$ with 95% confidence level) at the point I, as was also discussed by Prasad (2000) for stereoscopic PIV measurements. It is therefore important to select it optimally to minimize the related errors. The factor $\Delta t$ directly affects the out-of-plane displacement of the particles and it has relatively high contribution (23%) to the total uncertainty of the time-averaged velocity at the point II as shown in figure 6.12(b). However, its effect is not statistically significant for the stream-wise velocity component at 95% confidence level. It is to be noted that, high contribution of a factor to the total uncertainty does not guarantee the factor to be statistically significant at a certain confidence level. The statistical significance of a factor is estimated by comparing its mean square ($MS_{factor}$) with the error mean square $MS_\varepsilon$ computing the $F_0$ value (shown in table 1) as: $F_0 = MS_{factor} / MS_\varepsilon$. The $F_0$ value is then compared to the critical value $F_c$. Even for the same value of the $MS_{factor}$, the factor is statistically significant if $MS_{factor} \geq F_c\, MS_\varepsilon$, and statistically insignificant if $MS_{factor} < F_c\, MS_\varepsilon$. Therefore, the percentage contribution of a factor alone does not reveal its statistical significance. Nevertheless, the analysis for $Y$ and $Z$ velocity components shows that the factor $\Delta t$ is significant in the regions of low flow fluctuations (the results are not shown for conciseness). In that case, the factor $\Delta t$ influences the magnitude of the peak-locking error and, as observed by Legrand et al. (2012), the regions of low flow fluctuations are those where the mean velocity is affected by peak-locking errors the most.

The pie chart from figure 6.12(a) shows that, for the point I i.e. the flow region of low flow fluctuations, the blocking factor (i.e. the stereoscopic camera angle) contributes the most (97%) to the total uncertainty in the time-averaged stream-wise velocity. However, for the flow regions of high flow fluctuations i.e. the points II and III, the random error (due to the factors not directly considered in the analysis) has the biggest contribution of 57% and 71% to the total uncertainty in the mean stream-wise velocity, as shown in figure 6.12(b) and 6.12(c), respectively. This is due to the flow fluctuations in these regions being high which makes it difficult to segregate

the contribution of individual systematic uncertainties. It is evident that in regions where the flow fluctuations are large, the random uncertainty of the mean velocity is also large due to the limited number of samples and therefore the limited statistical convergence. In these regions, the random errors dominate over the systematic error sources, as shown in figure 6.12 for points II and III. In contrast, in regions of low flow fluctuations (e.g. point I of figure 6.12), the systematic error sources are expected to dominate.

## 6.5. Conclusions

A PIV uncertainty quantification (UQ) approach is proposed based on a statistical tool called Design of Experiments (DOE). The basic principle of the approach is to measure a statistical quantity, ideally constant in time, for the different levels of experimental factors and to compute total variance and individual variances arising from the different levels of each of the factors. The proposed methodology is assessed for planar PIV measurements of the flow over a NACA0012 airfoil at 15 degrees angle of attack to quantify the uncertainty of the time-averaged velocity and Reynolds stress. Four design factors, namely camera aperture ($f\#$), inter-frame time separation ($\Delta t$), interrogation window size ($D_I$), laser sheet thickness ($\Delta z$), and a blocking factor of seeding density are considered for the analysis. It is found that the uncertainty of the mean velocity quantified by the DOE approach is significantly larger than random uncertainty estimated for one individual measurement from data statistics, which is ascribed to the capability of the DOE approach to account also for the systematic uncertainties. Additionally, the effect of the seeding density (block) has large contribution to the total uncertainty in the time-averaged stream-wise velocity everywhere in the flow domain. On the contrary, the factors $\Delta t$ and $\Delta z$ show significant contributions to the total uncertainty in the flow regions of low fluctuations and high fluctuations, respectively. In the case of Reynolds normal stress, it is found that the interrogation window size $D_I$ and seeding density are the major contributors to the total uncertainty. The proposed methodology is also applied to the investigation by stereoscopic PIV of the flow at the outlet of a ducted Boundary Layer Ingesting (BLI) propulsor. The total

uncertainties in time-averaged stream-wise velocities are computed along with the analysis of the effects of the experimental factors, namely camera aperture, inter-frame time separation, interrogation window size and stereoscopic camera angle. It is clear from the results that the stereoscopic camera angle has very significant contribution to the total uncertainty. Additionally, $\Delta t$ is found to affect the total uncertainty in the flow regions of high fluctuations. The present work thus provides the ability to segregate the systematic uncertainties due to the experimental factors considered for the analysis. Knowing these constituent uncertainties, it will be possible to optimize the experiment in order to reduce the total uncertainty. The proposed methodology has been successfully used for planar (both 2C and 3C) PIV measurements. However, the approach is general and can be applied universally, irrespective of the kind of PIV setup for uncertainty quantification in any of the measured quantities.

# Chapter 7
# Elimination of Background Reflections by Anisotropic Diffusion

## Abstract

A novel approach is introduced that allows the elimination of undesired laser light reflections from PIV images. The approach relies upon anisotropic diffusion of the light intensity, which is used to generate a background image to be subtracted from the original image. The intensity is diffused only along the edges and not across the edges, thus allowing to preserve in the background image the shape of boundaries as laser light reflections on solid surfaces. Due to its ability of producing a background image from a single snapshot, opposed to most methods that make use of intensity information in time, the technique is particularly suitable for elimination of reflections in PIV images of unsteady models, such as transiting objects, propellers, flapping and pitching wings. The technique is assessed on an experimental test case which considers the flow in front of a propeller, where the laser light reflections on the model's surface preclude accurate determination of the flow velocity. Comparison of the anisotropic diffusion approach with conventional techniques for suppression of light reflections show the advantages of the former method especially when reflections need to be removed from individual images.

---

The work in this chapter has been published in Adatrao S and Sciacchitano A (2019) Elimination of unsteady background reflections in PIV images by anisotropic diffusion. Meas. Sci. Technol. 30:035204.

The MATLAB scripts related to this work are available publicly on 4TU.ResearchData platform with DOI: https://doi.org/10.4121/uuid:9a6639f7-4ade-40a4-915c-fed1414b1251

The figures related to this work are available publicly on 4TU.ResearchData platform with DOI: https://doi.org/10.4121/uuid:24193f84-4ade-43f7-423c-9875-9a9d2292bcc1.

## 7.1. Introduction

PIV images are often affected by unwanted light reflections occurring when the laser light impinges on a solid surface. The intensity of those reflections can be one order of magnitude larger than that of the particle images, causing a high auto-correlation peak in the correlation function. Such peak can be much higher than the particle images displacement cross-correlation peak, thus precluding accurate determination of the flow velocity in proximity of a solid surface.

Several approaches have been devised to avoid laser light reflections when conducting the measurements. Whenever possible, it is good practice to cover the model with mat black paint, so that most of the laser light impinging on a surface is absorbed instead of being reflected (Gui et al., 2001). Fluorescent paint (e.g. rhodamine) can be applied to the model surface in order to change the wavelength of the reflected light from green to red (Depardon et al., 2005). A bandpass filter mounted on the camera lens allows to reject the red light from the surface, thus retaining only the green light scattered from the particles. However, in many cases the model cannot be painted, either because of the presence of wall tapping for pressure measurements, or in order not to alter the surface roughness and consequently the boundary layer properties. For flat surfaces, Kähler et al. (2006) report that tangential model illumination allows a dramatic suppression of undesired wall reflections. Nevertheless, in presence of more complex model geometries where the model surface presents a curvature, tangential illumination cannot be achieved on the entire surface, but only at one specific location of the surface. The influence of the imaging angle was investigated by Lin and Perlin (1998). The authors report that, for measurements in water flows with free surface, tilting the camera to the air-water Brewster angle has the effect of removing most of the reflections from the water free surface. More recently, Kähler (2009) investigated the effect of the model material and surface treatment on the intensity of light reflections; the author found that aluminum models with highly polished surface has the minimum diffusive reflectivity among the tested materials (steel, carbon fiber reinforced plastic, glass, PMMA).

Despite the efforts above, in many cases laser light reflections are still present in the PIV recordings and need to be treated in the pre-processing phase (image restoration). The objective of image restoration is to remove the unwanted background from the images while keeping the particle images signal. In some cases, the background removal is simply achieved by recording a background image without tracer particles, and then removing it from the PIV recordings. Even if the background image has not been acquired, in stationary problems (no moving interfaces or pulse-to-pulse light intensity variation) it is possible to generate such background image by image statistics, computing the minimum or the average of the light intensity at each pixel location (Adrian and Westerweel, 2011). However, it is well known that the subtraction of time-average intensity may lead to removal of particle images from the recordings, especially in the low-velocity regions where the particles displacement is the minimum. For slowly moving light reflections or light intensity variations at frequency much lower than the acquisition frequency, subtraction of a time-varying background, generated by sliding-average or sliding-minimum light intensity over a short kernel, can be employed. Theunissen et al. (2008) assessed by Monte Carlo simulations different pre-processing techniques for background reflection removal. The authors report that a combination of local minimum intensity subtraction and equalization of mean intensity is effective in removing reflections that are constant in time. Alternatively, Sciacchitano and Scarano (2014) proposed the use of a temporal high-pass filter to remove unsteady background reflections while retaining the particle image intensity. The approach is based on the decomposition of the signal in the frequency domain and the removal of the low-frequency content, representative of the unwanted light reflections. The underlying assumption of the approach is that the contribution of the reflection (low-frequency) is well separated in the frequency domain from the contribution of the particle images (high-frequency), meaning that the reflection must reside for a few time instants in a pixel location. Recently, Mendez et al. (2017) proposed a POD-based background removal, which can in principle eliminate reflections also on moving surfaces, provided that a sufficiently large ensemble of images is available for convergence of the POD modes. However, even this approach

requires that the reflection resides for several recordings in the same pixel locations, which is often not the case in presence of towed or moving models, flapping or rotating wings. In the latter cases, background removal cannot rely upon image statistics, but must be conducted on individual raw images. Most approaches rely on the consideration that the particle images have shorter length scale (typically 1 to 5 pixels) than the background reflection, which may cover tens of pixels. Hence, the contribution of the particle images can be isolated from that of the background by applying a spatial high-pass filter, where the filter kernel should have a linear size at least as large as the particle image diameter. Several filters have been proposed in the past, including the top-hat sliding-average filter, the Gaussian filter, the median filter (Adrian and Westerweel, 2011) and the min/max filter (Westerweel, 1993). Nevertheless, the use of an isotropic filter, which has the same effects in all directions, typically yields low performance in proximity of sharp reflections, causing reduction of the signal level.

Honkanen and Nobach (2005) proposed a simple background extraction approach for double-frame PIV images, where the second frame of the image pair is subtracted from the first frame. The idea is that everything that stays stationary in the image pair, namely the background, is removed from the first image. However, this approach may lead to particles cancellation in cases of high source density or in regions where the flow velocity is the lowest. Another approach proposed by Deen et al. (2010) to eliminate moving reflections relies upon the combination of several image processing techniques, such as intensity normalization, background subtraction and masking. The approach was successfully employed by the authors to remove the undesired correlation peak due to non-stationary bubbles in a two-phase flow. However, the requirement to use several techniques makes this approach computationally expensive for most practical applications. Mejia-Alvarez and Christensen (2013) modified the algorithm proposed by Honkanen and Nobach (2005) by computing the normalized local intensity with respect to the difference between sliding median and minimum intensities. Although this algorithm is able to suppress the residual background reflections which are not eliminated by Honkanen and Nobach's approach, its performances have been demonstrated only for diffused

reflections due to an irregular rough wall, and not in presence of sharp reflections occurring e.g. when the laser sheet impinges on a solid surface.

The discussion above shows that an effective methodology for the removal of the unwanted laser light reflections from individual PIV images, thus without making use of image statistics, is currently missing. Such an approach would find its application in PIV measurements where the laser light reflection is unsteady e.g. due to the presence of transiting objects, propellers, flapping or pitching wings.

In the image processing community, approaches for edge detection based on anisotropic diffusion have been widely used in the last three decades since the seminal paper of Perona and Malik (1990). The idea is to compute a sliding-average of the intensity of an image on an anisotropic kernel which accounts for the intensity gradient. The approach has been successfully employed to enhance edges with respect to background noise. Further improvements to the technique have been proposed by Chao and Tsai (2006) for restoration of astronomical images. In their case, the image of the Henize 70 nebula was obscured by sparking stars. The approach was employed to segregate the stars, which had low length scale of the order of a few pixels, from the nebula characterized by large length scale and low intensity gradient. In PIV images, the light reflections are sharp and usually have higher intensity levels than the particle images, as opposed to the case of the nebula images. Hence, in this chapter, we further develop the approach of Perona and Malik (1990) and Chao and Tsai (2006) for isolating the contribution of the particle images from that of unwanted light reflections.

## 7.2. Proposed methodology

To explain the technique, consider a raw image $I_R(x,y)$ where both unwanted laser light reflections and tracer particle images are present. A background image $I_{BG}(x,y)$, ideally containing only the unwanted laser light reflections and no tracer particle image, is often computed via sliding-average of the intensity of $I_R$ (Adrian and Westerweel, 2011). The latter operation is

typically conducted by convolution of $I_R$ with a kernel $G$, which is usually top-hat or Gaussian. As pointed out by Koenderink (1984) and Hummel (1987), $I_{BG}$ can be also interpreted as the solution $I(x,y,t)$ of the diffusion equation:

$$\frac{\partial I}{\partial t} = \Delta I = \frac{\partial^2 I}{\partial x^2} + \frac{\partial^2 I}{\partial y^2} \tag{7.1}$$

with the initial condition $I(x,y,t=0) = I_R(x,y)$. Notice that in equation (7.1) the intensity is diffused isotropically, with no preferential direction (i.e. diffusion occurs at the same speed in all directions). Also, equation (7.1) treats in the same way particle images, which cover only a few pixels, and reflections, which typically affect several pixels. When equation (7.1) is applied to typical PIV images with reflections [figure 7.1(a)], a clear smoothing of the unwanted laser light reflection is noticed [figure 7.1(b)]. As a consequence, the solution of equation (7.1) is not a good estimate of the true background image.

Following Perona and Malik (1990), equation (7.1) can be rewritten into the anisotropic diffusion equation, so that diffusion occurs *along* the edges and not *across* the edges:

$$\frac{\partial I}{\partial t} = \nabla \cdot [c(x,y,t)\nabla I] = c(x,y,t)\Delta I + \nabla c \cdot \nabla I \tag{7.2}$$

Perona and Malik (1990) proposed to choose the diffusion coefficient $c$ as a function of the magnitude of the intensity gradient:

$$c(x,y,t) = g[\nabla I(x,y,t)] \tag{7.3}$$

being $g$ a suitable monotonic function. The authors used the following expression for $g$:

$$g(x,y,t) = \frac{1}{1 + \left(\frac{|\nabla I|}{K}\right)^2} \tag{7.4}$$

where $K$ is a positive constant termed as threshold parameter.

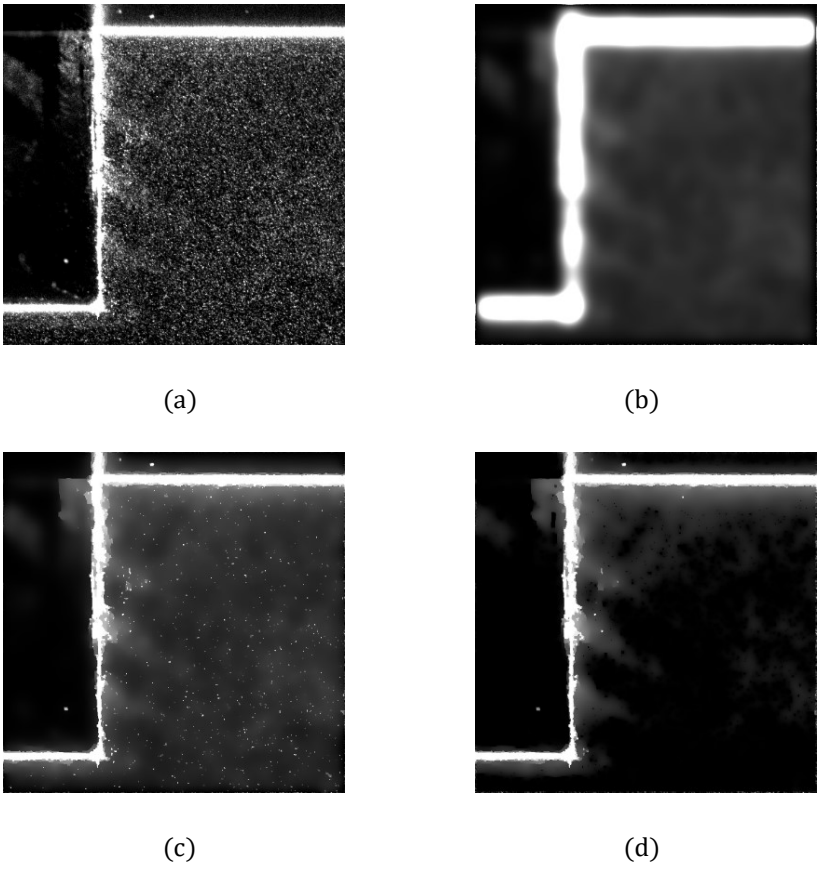

(a) (b)

(c) (d)

Figure 7.1. Comparison of different approaches for retrieving the background image. (a) raw image of a cavity flow measurement (Iannetta et al. 2016); (b) background image by isotropic diffusion (sliding-average intensity); (c) background image by Perona and Malik (1990) approach; (d) background image by the proposed approach. The following parameter values are used for the evaluation of the background image: $K = 10$ and $t_f = 300$, $t_f$ being the number of iterations.

When $g$ is chosen as a monotonically decreasing function, little diffusion occurs in the direction of high intensity gradient, e.g. at the interface between the laser reflection and the fluid region. Conversely, the diffusion mainly occurs in the direction of low intensity gradients, i.e. along the light

reflection. The approach proposed by Perona and Malik (1990) is very effective in avoiding smoothing of the edges, but it considers only the magnitude of the intensity gradient, and not the local intensity. As a consequence, it does not cause diffusion of small intense particle images, which remain in the estimated background image [figure 7.1(c)].

Modifications to equation (7.4) have been proposed by Chao and Tsai (2006, 2010) to account not only for the intensity gradient, but also to the local intensity variance. In the present work, the diffusion coefficient is computed also as a function of the local normalized intensity $I_n$ to enable the distinction between reflections, which cover several pixels in an image, and pointwise bright spots such as the particle images. $I_n$ is evaluated as the local intensity normalized with respect to the local mean of the intensities [computed with respect to 12 neighbors in a diamond shaped kernel; the neighbors are defined by $D_8$ distance $= 1$ and $D_4$ distance $= 2$, as described in Gonzalez and Woods (2002)]:

$$c(x, y, t) = g[\nabla I(x, y, t), I_n] \tag{7.5}$$

$$g(x, y, t) = \frac{1}{1 + \left(\frac{|\nabla I|}{K \cdot I_n}\right)^2} \tag{7.6}$$

The particle images are typically characterized by large values of the normalized local intensity $I_n$ compared to the magnitude of the intensity gradient $|\nabla I|$, whereas the reflections feature small values of $I_n$ with respect to the corresponding $|\nabla I|$. It is to be noted that the normalized local intensity $I_n$ and the magnitude of the intensity gradient $|\nabla I|$ can be compared directly since $|\nabla I|$ is defined in the discretized form as the difference between the intensities of the neighboring pixels. Thus, the diffusion coefficient is large for the particle images and small for the reflections, as shown in figure 7.2. This choice enables high diffusion for the particle images, and as a result, the particle images are not present anymore in the background image [figure 7.1(d)].

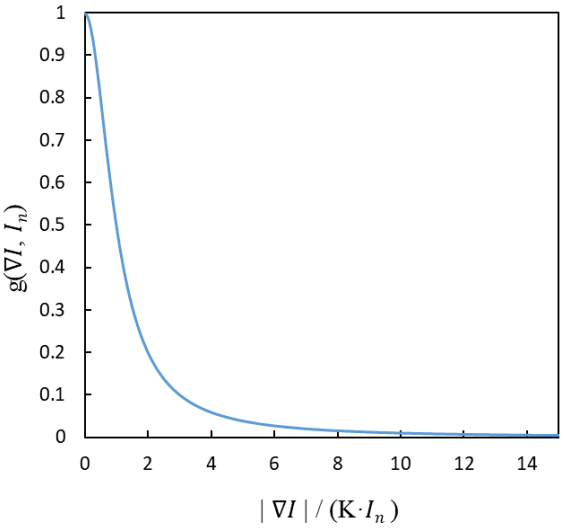


Figure 7.2. Plot of the diffusion coefficient function given by equation (7.6)

### 7.2.1. Numerical implementation

Following Perona and Malik (1990), equation (7.2) is discretized as follows:

$$I_{i,j}^{t+1} = I_{i,j}^{t} + \lambda[c_N \nabla_N I + c_S \nabla_S I + c_E \nabla_E I + c_W \nabla_W I]_{i,j}^{t} \tag{7.7}$$

where $(i, j)$ are the pixels locations along $y$ and $x$ directions, respectively, $0 \leq \lambda \leq 0.25$ for numerical stability, the subscript $N$, $S$, $E$ and $W$ represent North, South, East and West, and $\nabla$ indicates the nearest-neighbor differences:

$$\begin{aligned} \nabla_N I &= I_{i-1,j} - I_{i,j} \\ \nabla_S I &= I_{i+1,j} - I_{i,j} \\ \nabla_E I &= I_{i,j+1} - I_{i,j} \\ \nabla_W I &= I_{i,j-1} - I_{i,j} \end{aligned} \tag{7.8}$$

In this work, $\lambda = 0.2$ is used in all analyses. The diffusion coefficients are updated at each time instant as a function of the local intensity gradient and normalized intensity level:

$$c_N = g(\nabla_N I, I_n)$$
$$c_S = g(\nabla_S I, I_n)$$
$$c_E = g(\nabla_E I, I_n)$$
$$c_W = g(\nabla_W I, I_n) \tag{7.9}$$

### 7.2.2. Selection of threshold parameter and number of iterations

To solve the anisotropic diffusion equation (7.2), the value of two relevant parameters must be selected: the threshold parameter $K$ and the number of iterations $t_f$. A parametric study is conducted to determine which combination of $K$ and $t_f$ is the most effective for background removal in PIV images.

First, the effect of threshold parameter is studied by considering different values of $K$ for the same number of iterations. Background and pre-processed images of a typical PIV raw image are illustrated in figure 7.3 for $t_f = 300$ iterations and $K$ equal to 5, 10 and 50, respectively. It is observed that for small values of the threshold parameter ($K = 5$), the particle images are not diffused sufficiently and therefore are still present in the background image (first column in figure 7.3). Conversely, a large value of $K$ ($K = 50$ in the example), causes diffusion of the sharp reflection along with the particle images. Hence, the reflection is not eliminated sufficiently in the pre-processed image obtained by subtracting the background image from the original raw image (last column in figure 7.3). The results can be explained based on the definition of the diffusion coefficient [equation (7.6)], where the large value of $K$ makes the diffusion coefficient approach unity. In the latter case, the diffusion process becomes isotropic as expressed in equation (7.1). It is observed that an intermediate value of $K$ ($K = 10$) yields better results than those for $K = 5$ and $K = 50$, by diffusing the particles sufficiently and by retaining the sharp reflection in the background image (middle column in figure 7.3). The results in figure 7.3, thus, suggest to use an intermediate value ($K = 10$) for the threshold parameter in the proposed anisotropic diffusion approach.

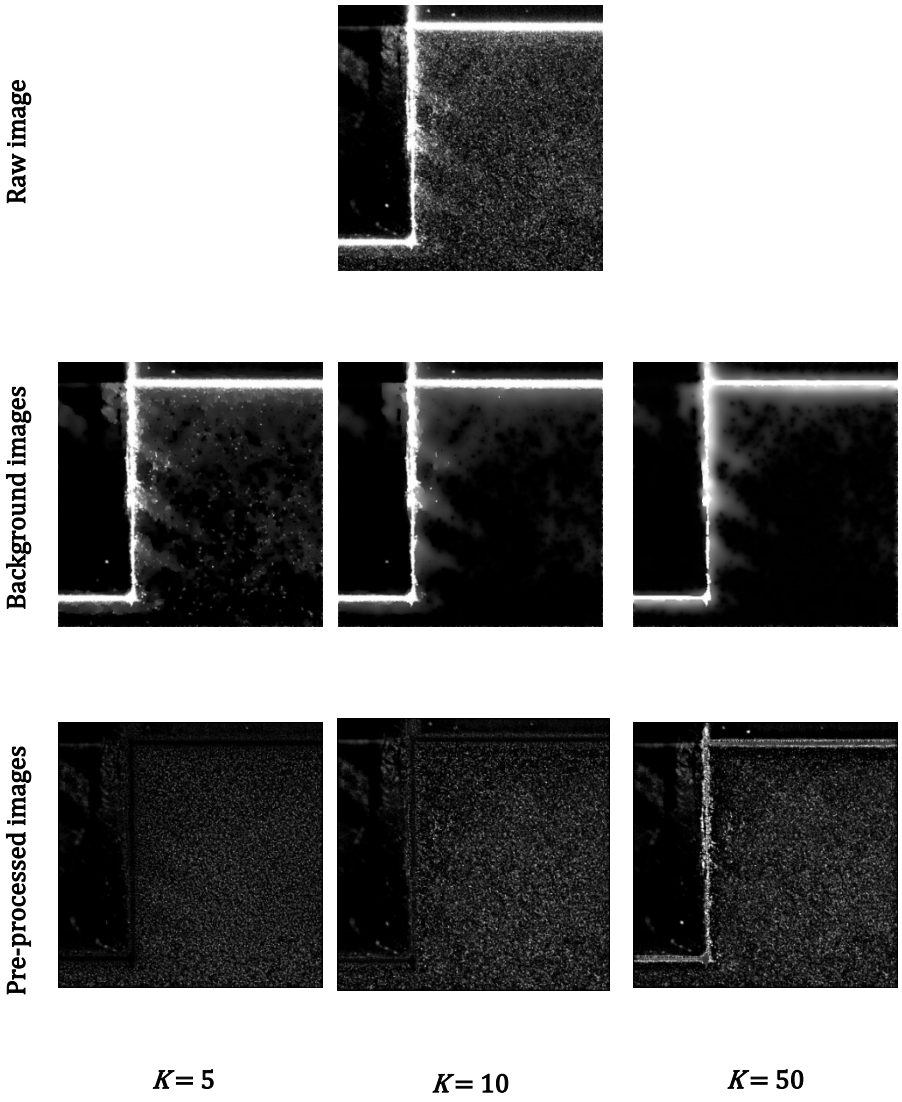


Figure 7.3. Comparison of raw image (top row), background images obtained using the proposed anisotropic diffusion approach after 300 iterations (middle row) and the pre-processed images for different values of threshold parameter ($K = 5, 10, 50$; bottom row)

To investigate the effect of the number of iterations, different values of $t_f$ are considered, keeping the threshold parameter constant ($K = 10$). The background and pre-processed images are shown in figure 7.4 for the three cases of $t_f$ equal to 10, 300 and 1000.

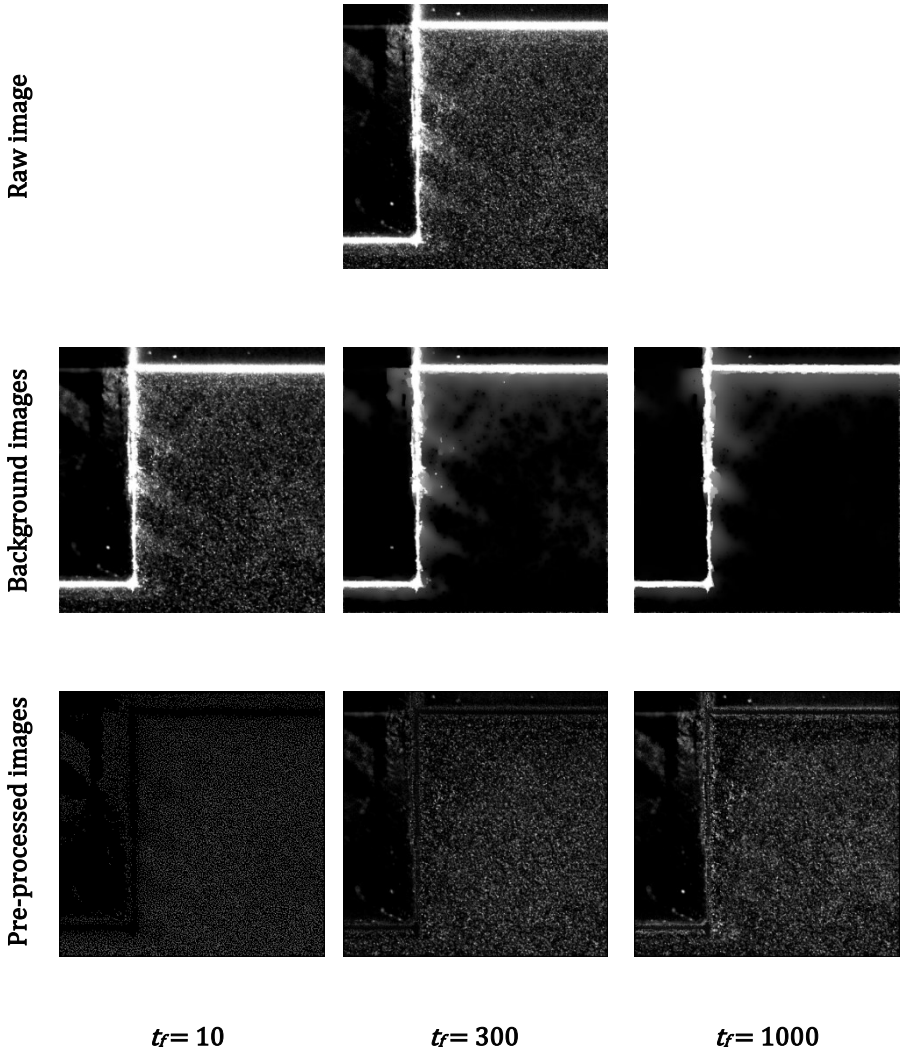


Figure 7.4. Comparison of background and pre-processed images obtained using the proposed anisotropic diffusion approach with $K = 10$ after different number of iterations ($t_f = 10, 300, 1000$)

It is observed that for small number of iterations ($t_f = 10$), the particle images are not diffused completely in the background image (first column in figure 7.4), yielding a pre-processed image where the signal is strongly attenuated. Conversely, for large number of iterations ($t_f = 1000$), the reflection is diffused in the background image (last column in figure 7.4), and therefore remains partly present in the pre-processed image. When $t_f = 300$ iterations are employed, the reflection remains sharp in the background image, whereas the particle images are diffused, yielding better background removal without loss of signal from the tracer particles (middle column in figure 7.4). Based on the above, the combination ($K$, $t_f$) = (10, 300) is more suitable than the other combinations in removing the background of the sharp reflections.

The effect of the number of iterations on the intensity levels of particle images and reflections is further illustrated in figure 7.5 for different values of $K$. Two windows of 10×10 pixels are considered representative of the reflections region and of the particle images region, respectively, as illustrated in figure 7.5 (left). After each iteration of the anisotropic diffusion algorithm, the intensity in each of the two windows is computed and plotted in figure 7.5 (right). The intensity of the reflection is calculated as the mean intensity in window 1, whereas the particles' intensity is calculated as the maximum intensity in the window 2, since the maximum intensity level represents the particle image peak intensity. Figure 7.5 (right) shows that the rate of diffusion is high for $K = 50$, causing the reflection to diffuse along with the particle images, which is not desirable. Instead, for $K = 5$ the diffusion is very slow and it takes more iterations to attenuate the particle images intensity compared to the other two values of $K$. Thus, $K = 10$ is found to be a good choice for the threshold parameter. The plots for $K = 10$ show that the particles are removed sufficiently after about 300 iterations; further increasing the number of iterations does not produce any improvement in the background image. In contrast, the reflection intensity reduces slightly with increasing number of iterations. Hence, a larger number of iterations has the effect of causing diffusion of the laser light reflections, returning an output image that is not representative of the actual background. For this reason, the number of 300 iterations in combination with a threshold

parameter $K = 10$ is considered a good choice to generate the background image. It is to be noted that the values are not the optimum values although they are shown to be effective. The reader is advised to plot curves as those of figure 7.5-right for a pair of PIV images to find out the suitable values of $K$ and $t_f$. Then the same values could be used for pre-processing all the images of a set. A rule of thumb is to select the value of $K$ such that it provides high slope for the curve of the particles intensities and low slope for that of the reflections intensities; the number of iterations is selected as the minimum value of $t_f$ for which the particles intensities are below a certain threshold (e.g. 5 counts).

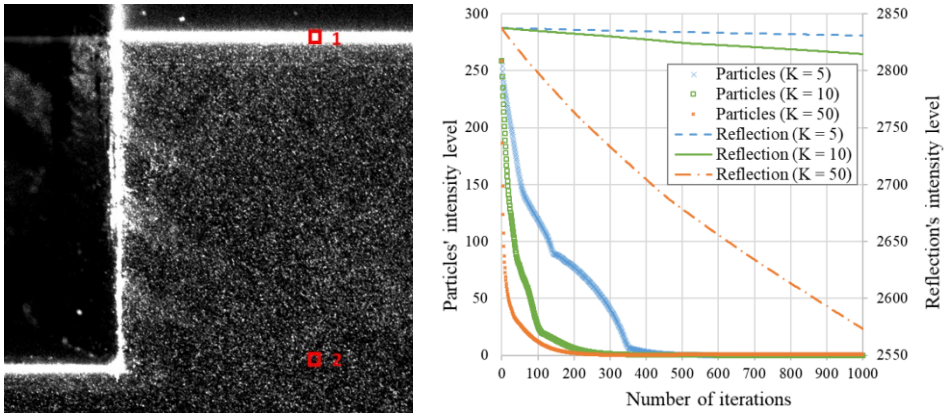


Figure 7.5. Plot of the intensity levels of particle images and reflection in the background image versus the number of iterations in the proposed anisotropic diffusion approach with different values of $K$ (the areas where the reflections and particle images intensities are analyzed are the red squares 1 and 2 in the figure on the left, respectively)

It should be noticed that the algorithm is not very sensitive to the choice of the processing parameters $K$ and $t_f$, in the sense that a variation of these parameters by 10-20% would in practice yield the same background image. The computational time is proportional to $t_f$ and is comparable to that of other standard filters.

## 7.3. Experimental assessment

The performance of the proposed anisotropic diffusion approach is assessed via PIV images acquired for the investigation of the propeller blade vortex interaction (Yang, 2017 and Yang et al., 2016). This particular experimental test case is chosen due to the presence of sharp and unsteady reflections of the propeller blade in the images. The experimental setup is shown in figure 7.6; the tests are carried out in the Open-Jet Facility (OJF) at Delft University of Technology. The propeller has eight blades with 0.304 m diameter and a blade angle of 41° is set up at ¾ of the blade radius to reproduce take-off conditions. A truncated two-dimensional DU96-W-180 airfoil is used as vortex generator (span of 1 m and chord length of 0.25 m) and is placed at 3.2 chord lengths upstream the propeller. Stereoscopic PIV measurements are performed in an upstream plane (positioned at $X/R$ = -0.20) perpendicular to the propeller axis as shown in figure 7.6 (right). Two LaVision Imager Pro LX 16M cameras (CCD sensor of 4870×3246 pixels, 12 bit resolution, 7.4 m pixel pitch) and a Quantel Evergreen 200 laser (dual pulsed Nd:YAG laser, 200 mJ energy per pulse) are used for the measurements. The flow is seeded with micron-sized water-glycol particles produced by a SAFEX Twin Fog Double Power smoke generator. The detailed description of the experimental setup can be found in Yang (2017).

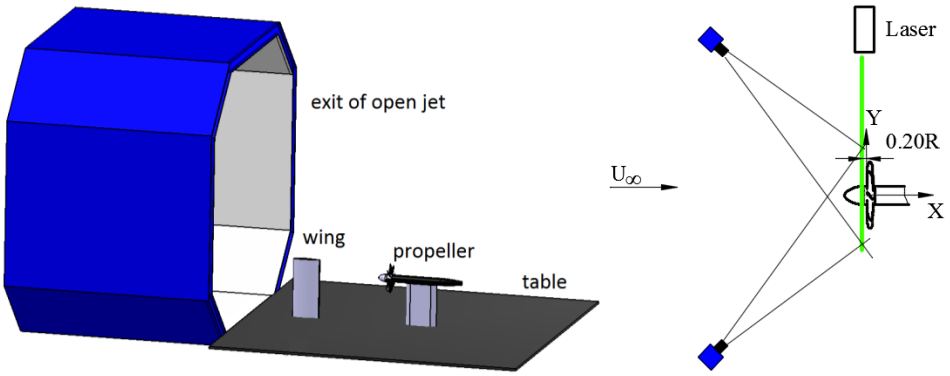


Figure 7.6. Experimental setup of the propeller blade vortex interaction (left) and top view of PIV setup in the upstream plane perpendicular to the propeller axis (right). Figure reproduced from Yang (2017)

Figure 7.7 shows a raw image pair and the corresponding displacement field (from a single camera) obtained in this experiment. As it can be seen in figure 7.7-left, the raw images are affected by strong laser light reflections, especially at the leading edge of the propeller blade. Since the propeller is spinning at 2,500 rpm, the propeller tip moves of about 2 mm between the two image frames. Notice that the measurement plane is located about 12 mm upstream of the blade leading edge; as a consequence, the fluid displacement in the measurement plane differs from the blade displacement. The cross-correlation analysis on the raw images returns a displacement field (figure 7.7-right) that is highly affected by the laser light reflections. The flow displacement in front of the propeller blade is highly over-estimated due to the presence of the blade reflection, which moves between the two frames.

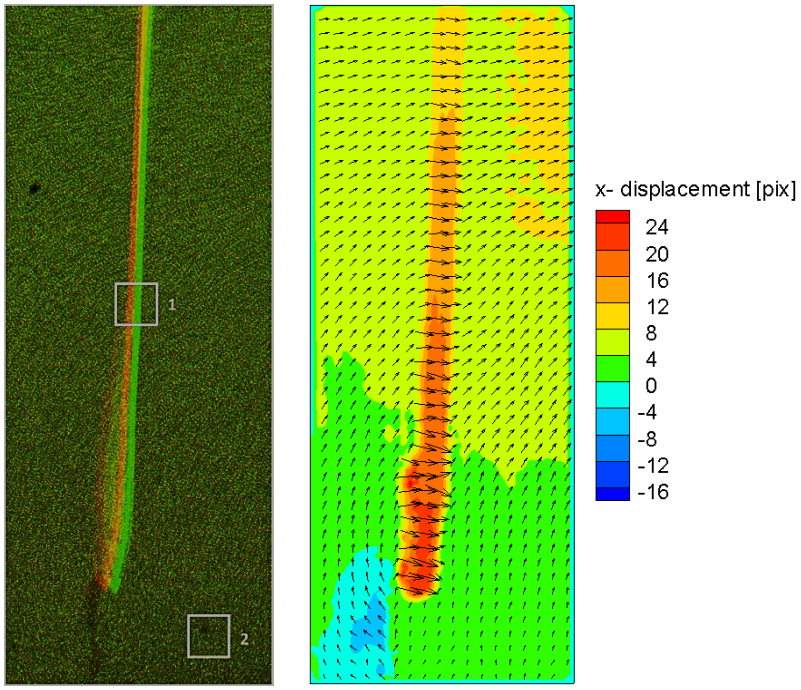


Figure 7.7. Raw image pair (left; red: first recording and green: second recording) and corresponding displacement field (right). The interrogation windows where the cross-correlation analysis is conducted are shown in the raw image pair

It should be noticed that, since the PIV acquisition was not synchronized with the rotation of the propeller blade, the position of the latter varies among different recordings (see figure 7.8). As a consequence, standard background removal approaches based on the statistical analysis of the sequence of images (e.g. subtraction of the time-average or time-minimum intensity) fail in removing the background reflection. Furthermore, even more advanced approaches based on image statistics such as the POD filter (Mendez et al., 2017) are not effective in this specific case, due to the limited number of recordings (250) per set of images, which causes the POD modes not to reach statistical convergence.

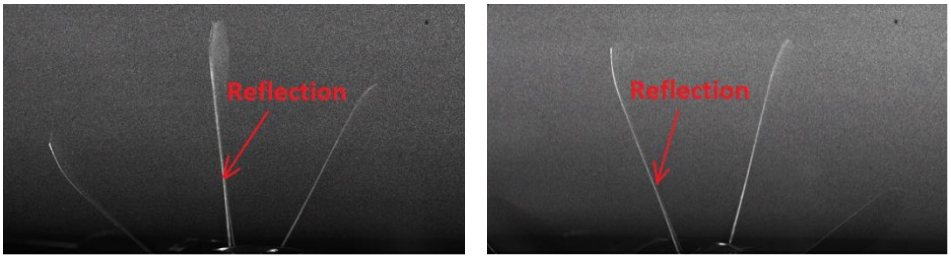


Figure 7.8. Examples of instantaneous PIV recordings showing the blades reflections, phase angle $\Psi = 6.0°$ (left) and $\Psi = 34.5°$ (right). Figure reproduced from Yang (2017)

When image pre-processing is performed, the relative intensity of the particle images with respect to the laser reflection can be highly enhanced. Figure 7.9 shows a comparison among the image pre-processing by sliding-average subtraction, median filter subtraction, median-based-normalization subtraction and the proposed anisotropic diffusion approach. In the first method, the background image (figure 7.9- first row- first column) is built as sliding-average (viz. isotropic diffusion) of the image intensity in a kernel of 3×3 pixels in 30 iterations. A Gaussian weighting is applied to the intensity within the kernel. In the second method, a median filter of kernel of 5×5 pixels is applied to the raw image to generate the background image (figure 7.9- second row- first column), which is then subtracted from the raw image to get the pre-processed image (figure 7.9- second row- second column). The next method is based on Mejia-Alvarez and Christensen's (2013) approach,

where normalization is performed with respect to the local median and minimum intensities in a kernel of 9×9 pixels. The two frames are then subtracted from each other to eliminate the background and further normalization is applied with respect to local maximum and minimum intensities. Finally, the intensity values are stretched according to the global maximum and minimum intensities in the original raw images. The background and pre-processed images obtained with this median-based-normalization algorithm are shown in figure 7.9 in the third row, first and second columns, respectively. As it can be seen in figure 7.9 (rows- 1, 2, 3), these three methods (viz. pre-processing by sliding-average subtraction, median filter subtraction and median-based-normalization subtraction) yield background images where the particle image intensity is highly reduced. However, also the light reflection on the propeller blade is diffused with respect to the raw images. As a consequence, when the pre-processed images are evaluated from the difference between raw images and background, they still feature laser light reflections which yield erroneous vectors in the displacement field (figure 7.9- rows- 1, 2, 3- last column). Instead, when the background image is built with the proposed anisotropic diffusion approach, the particle image intensity is strongly diffused, whereas no significant diffusion occurs on the light reflections on the propeller blade (figure 7.9- last row- first column). As a result, the background image by anisotropic diffusion is much more representative of the true background. In the pre-processed image, the intensity of the laser light reflections on the propeller blade becomes lower than that of the particle images (figure 7.9- last row- second column). Hence, the computed displacement field does not feature any erroneous vector associated with unwanted laser light reflections on the solid surface (figure 7.9- last row- last column).

For a quantitative assessment of the performance of the anisotropic diffusion filter, the cross-correlation analysis is conducted in two interrogation windows of 65×65 pixels, shown in figure 7.7 (left). The interrogation window 1 is located in front of the blade and features strong laser light reflections, whereas interrogation window 2 is in a region free of any unwanted reflections. The results of the cross-correlation analysis are illustrated in figures 7.10 and 7.11 and the corresponding pixel

displacements and cross-correlation signal-to-noise ratios (SNR) are reported in table 7.1.

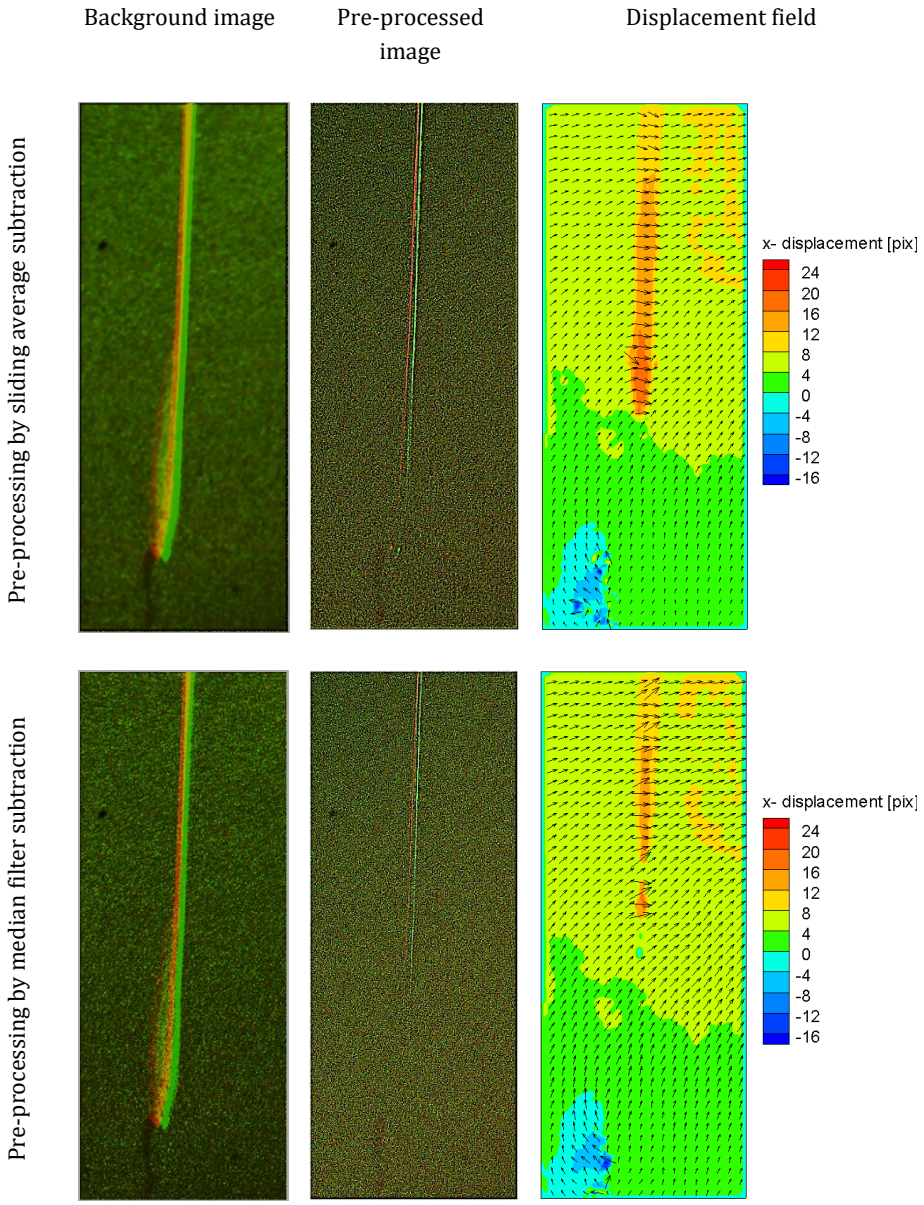

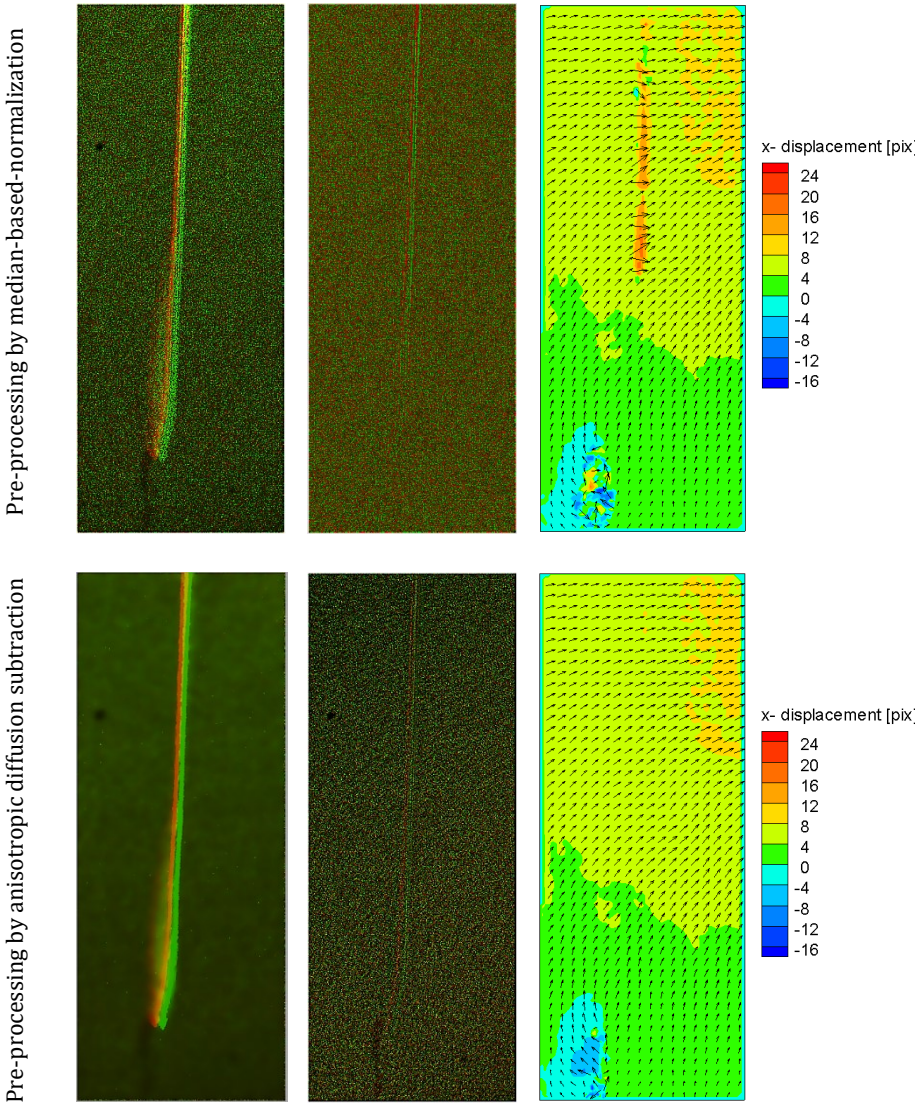


Figure 7.9. Comparison among image pre-processing by sliding average subtraction (kernel of 3×3 pixels and 30 iterations), median filter subtraction (kernel of 5×5 pixels), median-based-normalization subtraction (kernel of 9×9 pixels) and the proposed anisotropic diffusion approach (diamond shaped kernel, $K = 10$ and 300 iterations). Background images (first column; red: first recording and green: second recording), pre-processed images (second column) and corresponding displacement fields (third column).

Table 7.1. Particle image displacement and correlation signal-to-noise ratio (SNR) in the two interrogation windows for different image pre-processing methods.

| Image | Interrogation Window 1 | | | Interrogation Window 2 | | |
|---|---|---|---|---|---|---|
| | Δx [pix] | Δy [pix] | SNR | Δx [pix] | Δy [pix] | SNR |
| Original | 16.0 | -0.6 | 0.1 | 0.9 | 3.9 | 9.3 |
| Sliding average subtraction | 16.1 | -2.1 | 0.2 | 0.9 | 3.8 | 7.2 |
| Median filter subtraction | 16.1 | -2.2 | 0.9 | 0.9 | 3.8 | 7.1 |
| Median-based-normalization subtraction | 6.2 | 4.3 | 1.5 | 1.0 | 3.7 | 3.0 |
| Anisotropic diffusion subtraction | 6.3 | 4.4 | 4.0 | 0.9 | 3.9 | 7.9 |

In interrogation window 1, the strong reflection on the propeller blade yields a high peak in the cross-correlation functions obtained from raw images and pre-processing by sliding-average subtraction or median filter subtraction [figure 7.10(a), (b), (c)]. The position of the peak corresponds to the displacement of the propeller blade between frame 1 and frame 2. As mentioned before, such displacement is not the same as the fluid displacement, because the plane of the propeller does not coincide with the measurement plane. Such peak is much larger than the true particle displacement peak (which can be seen around $\Delta x = 6$ pix, $\Delta y = 4$ pix) yielding a correlation signal-to-noise ratio (SNR) smaller than one. As a consequence, an erroneous displacement vector is estimated. Conversely, in the case of pre-processing by median-based-normalization or anisotropic diffusion, the correlation peak due to the blade movement is much attenuated or not even visible [figure 7.10(d) and (e)]. Hence, the particle images displacement peak is correctly identified, yielding a valid vector estimation. However, the comparison of the correlation SNR's from table 7.1

shows that the particles signal is attenuated more with the median-based-normalization algorithm (SNR = 1.5) than with the anisotropic diffusion approach (SNR = 4.0).

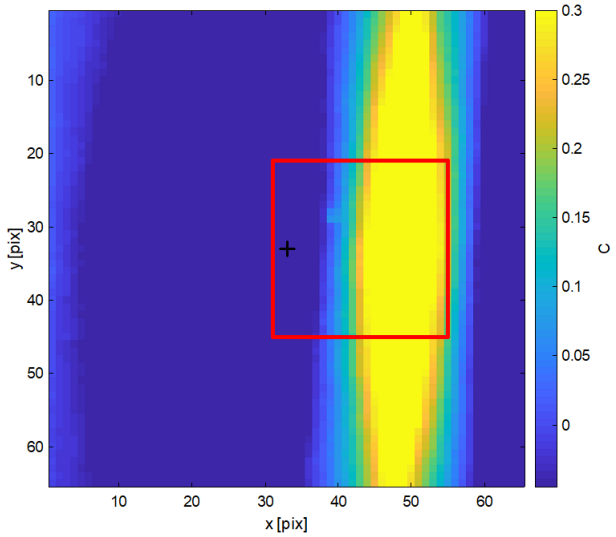


(a)

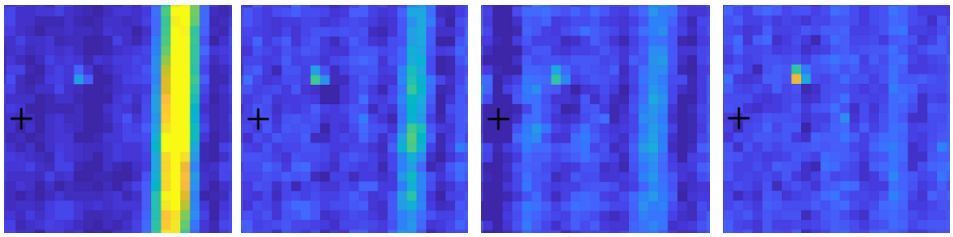

(b) (c) (d) (e)

Figure 7.10. Comparison among cross-correlation functions in the interrogation window 1 (with light reflections). (a) raw images; (b) image pre-processing by subtraction of sliding average intensity; (c) image pre-processing by subtraction of background by median filter; (d) image pre-processing by subtraction of background by median-based-normalization; (e) image pre-processing by subtraction of background by anisotropic diffusion. The black cross indicates the center of the cross-correlation window. For sake of clarity, figures (b) to (e) only show the smaller region represented by the red square in figure (a).

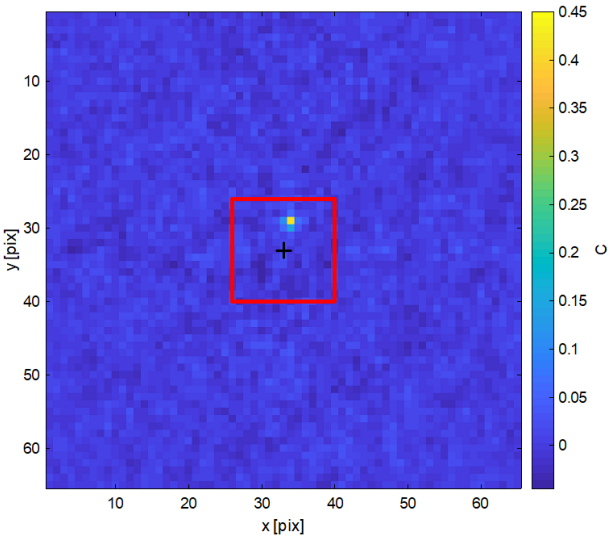


(a)

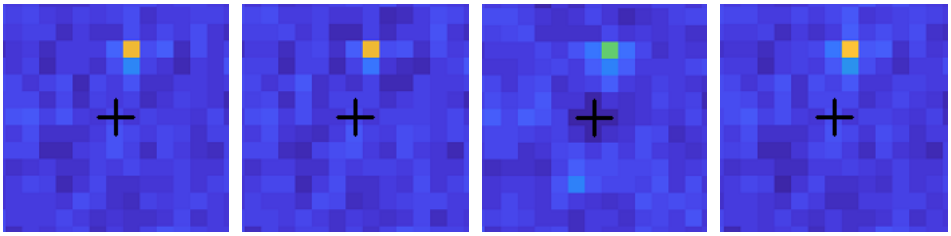

(b) (c) (d) (e)

Figure 7.11. Comparison among cross-correlation functions in the interrogation window 2 (without light reflections). (a) raw images; (b) image pre-processing by subtraction of sliding average intensity; (c) image pre-processing by subtraction of background by median filter; (d) image pre-processing by subtraction of background by median-based-normalization; (e) image pre-processing by subtraction of background by anisotropic diffusion. The black cross indicates the center of the cross-correlation window. For sake of clarity, figures (b) to (e) only show the smaller region represented by the red square in figure (a).

When the cross-correlation analysis is conducted in a region free of any reflections (viz. interrogation window 2), all pre-processing methods correctly identify the displacement peak (figure 7.11), leading to a displacement estimate accurate within 0.1 pixels. However, it is noticed that

the image pre-processing with the median-based-normalization algorithm strongly attenuates the particles signal, returning a relatively low SNR which results in slightly inaccurate displacement measurements. On the contrary, the SNR obtained with the anisotropic diffusion filter is approximately the same as that achieved with the raw images, which indicates that the approach has no detrimental effect in regions where no reflections are present.

## 7.4. Conclusions

A novel approach is proposed to suppress undesired light reflections from PIV images. The approach relies upon generating a background image by anisotropic diffusion of the intensity distribution of the raw image. The principle is that, by means of anisotropic diffusion, the image intensity is diffused only along the edges and not across the edges, maintaining sharp reflections in the background image. The latter is then subtracted from the original image, yielding a pre-processed image where no reflection is present and only the contribution of the particle images is retained. Contrary to most approaches for background removal that require the analysis of an image sequence (e.g. subtraction of time-average or time-minimum image intensity, POD filter, high-pass filter in the frequency domain), the proposed approach is applicable to individual images, and is therefore suitable for all the cases where the reflection is unsteady, or when a short image sequence has been acquired, yielding lack of convergence in the statistical analysis.

A parametric study has been conducted to evaluate the effect of two key parameters of the approach, namely the threshold parameter $K$ and the number of iterations $t_f$. The threshold parameter $K$ governs the rate of diffusion: high values of $K$ yield isotropic diffusion, typically over-smoothing the reflections; conversely, low values of $K$ slow down the diffusion process. The number of iterations $t_f$ determines the number of neighboring pixels involved in the diffusion process. It is found that values of $K = 10$ and $t_f = 300$ are effective for the PIV images used in this work. Readers are advised to perform the parametric study for a pair of images to determine the suitable values of $K$ and $t_f$.

The proposed approach is applied to real PIV images acquired for the study of the blade vortex interaction, characterized by sharp and unsteady reflections of the propeller blades. Due to the unsteady character of the reflections, background removal approaches based on the statistical analysis of the entire sequence of images are not effective. The results of the anisotropic diffusion background removal are compared with the conventional pre-processing methods of isotropic diffusion (sliding-average) filter, median filter subtraction and median-based-normalization filter. The comparison shows that the proposed approach is effective in removing the unsteady reflections, allowing the estimation of the particles displacement even in close proximity of the reflection region. In regions of the image not affected by reflections, the use of the anisotropic diffusion filter retains approximately the same image quality as in the raw images.

In the present chapter the performances of the method have been demonstrated for the case of sharp reflections, occurring e.g. when the laser light impinges on a solid surface. In presence of diffused reflections, the anisotropic diffusion coefficient assumes approximately the same value in all directions, and the anisotropic filter behaves in practice as isotropic filter (sliding-average).

# 7. Elimination of Background Reflections by Anisotropic Diffusion

# Chapter 8
# Conclusions and Outlook

## Abstract

The present chapter highlights the major results from the various chapters of the thesis. The principles of the proposed methodologies and approaches are also briefly stated here. The concluding remarks based on the findings in each of the works are presented. Finally, the outlook on these conclusions is also provided.

## 8.1. Survey on PIV errors and uncertainty quantification

In the chapter 4, we performed a survey to determine how PIV users and researchers worldwide perceive the PIV error sources and the current approaches for uncertainty quantification. A questionnaire consisting of 11 questions has been formulated and sent to 475 researchers from both academia and industry. The total number of responses was 103, resulting in a response rate of 22%. The responses were analyzed quantitatively in pie charts, bar graphs and bubble plots, whereas the descriptive answers supported the analysis of the charts. Overall, it is found that the PIV community struggles more with the error sources associated with measurement setup and image acquisition, such as background image reflections, seeding density and its distribution, image calibration. Conversely, the image analysis step is perceived as easy and accurate, possibly because much work in the last three decades has been dedicated to optimizing image interrogation algorithms to maximize the accuracy of the resulting velocity fields. Further detailed analysis was performed by separating the responses of two groups of PIV users, namely users who employ planar (2D2C and 2D3C) measurement setups and users who perform tomographic 3D3C (PIV and PTV/LPT) measurements. It is found

that the errors due to background image reflections, seeding and image noise are considered to be significant by both the groups. However, the errors due to the laser and camera misalignment and out-of-plane motion of particles are more common for the planar setup users. Contrary, the errors related to the calibration procedure are more problematic for the tomographic setup users.

The PIV users are aware of the importance of uncertainty quantification (UQ). However, only 49% of the respondents always quantify the uncertainty of their PIV measurements. PIV users can choose among a wide range of UQ algorithms, some of which are also implemented in commercial software, thus making them easy to use. Nevertheless, given the wide variety of UQ approaches used, it is clear that no approach can be currently considered as the standard tool for PIV-UQ. Furthermore, the analysis of the two groups of PIV users employing either planar or tomographic setups shows that the standard UQ approaches are limited to be used in the tomographic measurements for uncertainty quantification. The need of a universally accepted PIV-UQ approach which can deal with random as well as systematic errors has been emerged from this analysis.

## 8.2. Multi-$\Delta t$ approach for peak-locking uncertainty quantification

A novel approach is proposed in the chapter 5 for the quantification of the peak-locking systematic uncertainty in PIV, which in turn also corrects the measured particle image displacement (and velocity) and Reynolds stress for peak-locking errors. The approach is based on the assumption that local flow statistics are constant in time, according to which the particle image displacement should vary linearly with the time separation ($\Delta t$) between two frames. However, in presence of peak locking, the measured particle image displacement is a non-linear function of $\Delta t$ as the measurement error in the displacement varies non-linearly with sub-pixel particle image displacement. Similarly, in presence of peak locking the Reynolds stress may vary significantly depending on the selected $\Delta t$. Hence, in the present

approach, it is proposed to acquire the measurements at various $\Delta t$'s and perform a least-squares regression of the measured quantities (displacements and Reynolds stresses). The displacement (and velocity) and Reynolds stress from regression represent more accurate estimates of the "true" values and thus used to quantify systematic errors and uncertainty due to peak locking in the measured displacement (and velocity) and Reynolds stresses, respectively. Guidelines for the selection of the $\Delta t$'s are also provided. The methodology is assessed for planar PIV measurements of the flow over a NACA0012 airfoil at 10 degrees angle of attack. The uncertainties in the measured velocity and Reynolds stresses are reduced by 50 to 80% and 35 to 75%, respectively, after correcting by the regression analysis. Relative coverage indices close to one are obtained for the mean velocity uncertainty and Reynolds stress uncertainty in both the potential and turbulent regions of the flow, indicating the ability of the methodology to quantify the uncertainty associated with peak-locking errors.

## 8.3. Design of Experiments (DOE) for PIV uncertainty quantification

A PIV uncertainty quantification (UQ) approach is proposed in the chapter 6 based on a statistical tool called Design of Experiments (DOE). The basic principle of the approach is to measure a statistical quantity, ideally constant in time, for the different levels of experimental factors and to compute total variance and individual variances arising from the different levels of each of the factors. The statistical analysis is performed using Analysis of Variances (ANOVA). The proposed methodology is assessed for planar PIV measurements of the flow over a NACA0012 airfoil at 15 degrees angle of attack to quantify the uncertainty of the time-averaged velocity and Reynolds stress. Four design factors, namely camera aperture ($f\#$), inter-frame time separation ($\Delta t$), interrogation window size ($D_I$), laser sheet thickness ($\Delta z$), and one blocking factor of seeding density are considered for the analysis. The design factors and the blocking factor are set at two different levels (low and high) each, resulting in a total of 32 measurements

($2^4 = 16$ in each block, following the $2^N$ rule, $N$ being the number of design factors) that are performed in a random order. The analysis leads to the estimation of total uncertainty in the time-averaged velocity and Reynolds stress as well as constituent systematic uncertainties due to the design and blocking factors. It is found that the uncertainty of the mean velocity quantified by the DOE approach is significantly larger than that estimated for one individual measurement, which is ascribed to the capability of the DOE approach to account also for the systematic uncertainties. Additionally, the effect of the seeding density (block) has large contribution to the total uncertainty in the time-averaged stream-wise velocity everywhere in the flow domain. On the contrary, the factors $\Delta t$ and $\Delta z$ show significant contributions to the total uncertainty in the flow regions of low fluctuations and high fluctuations, respectively. In the case of Reynolds normal stress, it is found that the interrogation window size $D_I$ and seeding density are the major contributors to the total uncertainty. The proposed methodology is also applied to the investigation by stereoscopic PIV of the flow at the outlet of a ducted Boundary Layer Ingesting (BLI) propulsor. The total uncertainties in time-averaged stream-wise velocities are computed along with the analysis of the effects of the experimental factors, namely camera aperture, inter-frame time separation, interrogation window size and stereoscopic camera angle. It is clear from the results that the stereoscopic camera angle has very significant contribution to the total uncertainty. Additionally, $\Delta t$ is found to affect the total uncertainty in the flow regions of high fluctuations. The present work is thus able to segregate the systematic uncertainties due to the experimental factors considered for the analysis. Knowing these constituent uncertainties, it will be possible to optimize the experiment in order to reduce the total uncertainty. The proposed methodology has been successfully used for planar (both 2C and 3C) PIV measurements, but has the potential to be extended for three-dimensional flow measurements by tomographic PIV and Lagrangian Particle Tracking.

## 8.4. Elimination of background reflections by anisotropic diffusion

A novel approach is proposed to suppress undesired light reflections from PIV images. The approach relies upon generating a background image by anisotropic diffusion of the intensity distribution of the raw image. The principle is that, by means of anisotropic diffusion, the image intensity is diffused only *along* the edges and not *across* the edges, maintaining sharp reflections in the background image. The latter is then subtracted from the original image, yielding a pre-processed image where no reflection is present and only the contribution of the particle images is retained. Contrary to most approaches for background removal that require the analysis of an image sequence (e.g. subtraction of time-average or time-minimum image intensity, POD filter, high-pass filter in the frequency domain), the proposed approach is applicable to individual images, and is therefore suitable for all the cases where the reflection is unsteady, or when a short image sequence has been acquired, yielding lack of convergence in the statistical analysis.

A parametric study has been conducted to evaluate the effect of two key parameters of the approach, namely the threshold parameter $K$ and the number of iterations $t_f$. The threshold parameter $K$ governs the rate of diffusion: high values of $K$ yield isotropic diffusion, typically over-smoothing the reflections; conversely, low values of $K$ slow down the diffusion process. The number of iterations $t_f$ determines the number of neighboring pixels involved in the diffusion process. It is found that values of $K = 10$ and $t_f = 300$ are effective for the PIV images used in this work. Readers are advised to perform the parametric study for a pair of images to determine the suitable values of $K$ and $t_f$.

The proposed approach is applied to real PIV images acquired for the study of the blade vortex interaction, characterized by sharp and unsteady reflections of the propeller blades. Due to the unsteady character of the reflections, background removal approaches based on the statistical analysis of the entire sequence of images are not effective. The results of the anisotropic diffusion background removal are compared with the

conventional pre-processing methods of isotropic diffusion (sliding-average) filter, median filter subtraction and median-based-normalization filter. The comparison shows that the proposed approach is effective in removing the unsteady reflections, allowing the estimation of the particles displacement even in close proximity of the reflection region. In regions of the image not affected by reflections, the use of the anisotropic diffusion filter retains approximately the same image quality as in the raw images.

In the chapter 7, the performances of the method have been demonstrated for the case of sharp reflections, occurring e.g. when the laser light impinges on a solid surface. In presence of diffused reflections, the anisotropic diffusion coefficient assumes approximately the same value in all directions, and the anisotropic filter behaves in practice as an isotropic filter (sliding-average).

## 8.5. Outlook

The survey on PIV error sources and UQ was a successful attempt to collect the thoughts of the PIV users and researchers on the PIV technique. We believe that the outcomes will create awareness in the PIV community and foster further developments for uncertainty quantification of planar and three-dimensional PIV data.

The multi-$\Delta t$ approach, applicable to statistical flow properties such as time-averaged velocity and Reynolds stresses, relies on image recordings with multiple time separations $\Delta t$ and a least-squares regression of the measured quantities. The application of this approach was shown for the planar PIV measurements in the present work. However, its application is not restricted to 2D-2C measurement system and has the potential to be extended to stereoscopic (2D-3C) measurements.

Since the PIV measurements are affected not only by peak-locking errors but also other systematic errors, an UQ approach which can consider multiple error sources is necessary. Therefore, a comprehensive framework based on a statistical tool called Design of Experiments (DOE) was introduced which allows to quantify the total uncertainty as well as the systematic

uncertainties arising from various sources. The methodology was applied for planar and stereoscopic PIV measurements in the present work. However, the methodology is general in nature and can be used for any type of experimental setup (e.g. planar PIV, stereoscopic PIV, tomographic PIV/PTV or LPT, micro-PIV, etc.), any flow regime (e.g. high speed flow, multi-phase flow, etc.) and any flow property of interest (e.g. velocity, vorticity or pressure). Moreover, the proposed PIV-UQ approach is comprehensive as the uncertainties arising from both random (unknown factors) and systematic (known factors) error sources are estimated.

The anisotropic diffusion approach was successfully used for planar PIV images to eliminate unsteady background reflections in the present work. The approach can also be useful in stereoscopic PIV measurements for reflections removal. In case of volumetric measurements, the background reflections are not as prominent because the laser light is more diffused to achieve volume illumination. The anisotropic diffusion approach can still be used for diffused reflections. However, its behavior is expected to resamble that of an isotropic diffusion filter.

The prosed approaches in the present work are not only useful in academic and research PIV experiments but also in the industrial PIV measurements (e.g. automotive, aerospace, wind energy, among others). The comprehensive framework for PIV-UQ based on DOE will complement the measured data with the uncertainty values, thus making the measured data more trustworthy and suitable for validation of numerical simulations.

# 8. Conclusions and Outlook

# References

Adrian RJ (1983) Laser velocimetry, in: Fluid Mechanics Measurements, (ed. RJ Goldstein) Springer, Berlin

Adrian RJ (1986) Multi-point optical measurement of simultaneous vectors in unsteady flow – a review. Int. J. Heat and Fluid Flow 7(2): 127-145

Adrian RJ (1991) Particle-image techniques for experimental fluid mechanics. Annu. Rev. Fluid Mech. 23: 261-304

Adrian RJ and Westerweel J (2011) Particle Image Velocimetry. Cambridge University Press

Aeschliman D and Oberkampf W (1998) Experimental methodology for computational fluid dynamics code validation. AIAA Journal 36: 733-741

Anderson JD Jr (2011) Fundamentals of Aerodynamics. 5th edition, McGraw-Hill

Angele KP and Muhammad-Klingmann B (2005) A simple model for the effect of peak-locking on the accuracy of boundary layer turbulence statistics in digital PIV. Exp. Fluids 38: 341-347

Atkinson C, Coudert S, Foucaut JM, Stanislas M and Soria J (2011) The accuracy of tomographic particle image velocimetry for measurements of a turbulent boundary layer. Exp. Fluids 50: 1031-1056

Benedict LH and Gould RD (1996) Towards better uncertainty estimates for turbulence statistics. Exp. Fluids 22: 129-136

Beresh SJ (2009) Comparison of PIV data using multiple configurations and processing techniques. Exp. Fluids 47: 883-896

Bhattacharya S, Charonko JJ and Vlachos PP (2016) Stereoscopic-particle image velocimetry uncertainty quantification. Meas. Sci. Technol. 28: 015301

## References


Bhattacharya S, Charonko JJ and Vlachos PP (2018) Particle image velocimetry (PIV) uncertainty quantification using moment of correlation (MC) plane. Meas. Sci. Technol. 29: 115301

Bosbach J, Kühn M and Wagner C (2009) Large scale particle image velocimetry with helium filled soap bubbles. Exp. Fluids 46: 539-547

Campagnole dos Santos AA, Childs M, Nguyen TD and Hassan Y (2018) Convergence study and uncertainty quantification of average and statistical PIV measurements in a matched refractive index 5 × 5 rod bundle with mixing vane spacer grid. Exp. Therm. Fluid Sci. 102: 215–31

Chao SM and Tsai DM (2006) Astronomical image restoration using an improved anisotropic diffusion. Pattern Recognition Letters 27: 335-344

Chao SM and Tsai DM (2010) An improved anisotropic diffusion model for detail-and edge-preserving smoothing. Pattern Recognition Letters 31: 2012-2023

Charonko JJ and Vlachos PP (2013) Estimation of uncertainty bounds for individual particle image velocimetry measurements from cross correlation peak ratio. Meas. Sci. Technol. 24: 065301

Chen J and Katz J (2005) Elimination of peak-locking error in PIV analysis using the correlation mapping method. Meas. Sci. Technol. 16: 1605-18

Cholemari MR (2007) Modeling and correction of peak-locking in digital PIV. Exp. Fluids 42: 913-922

Christensen KT (2004) The influence of peak-locking errors on turbulence statistics computed from PIV ensembles. Exp. Fluids 36: 484-497

Coleman DE and Montgomery DC (1993) A systematic approach to planning for a designed industrial experiment. 36th Annual Fall Technical Conference, Philadelphia, Pennsylvania, USA, October 8-9

Coleman HW and Steele WG (2009) Experimentation, Validation, and Uncertainty Analysis for Engineers. 3rd edition, Hoboken, NJ: Wiley

Cowen EA and Monismith SG (1997) A hybrid digital particle tracking velocimetry technique. Exp. Fluids 22: 199-211

De Groot MH (1989) Probability and Statistics. 2nd edition, Addison-Wesley publishing company

DeBonis JR, Oberkampf WL, Wolf RT, Orkwis PD, Turner MGBH and Benek JA (2012) Assessment of computational fluid dynamics and experimental data for shock boundary-layer interactions. AIAA Journal 50: 891–903

Deen NG, Willems P, Annaland MVS, Kuipers JAM, Lammertink RGH, Kemperman AJB, Wessling M, Meer WGJ (2010) On image pre-processing for PIV of single- and two-phase flows over reflecting objects. Exp. Fluids 49: 525-530

DeLoach R (2000) The modern design of experiments: a technical and marketing framework. 21st AIAA Advanced Measurement Technology and Ground Testing Conference, Denver, CO, USA, June 19-22

DeLoach R and Micol JR (2011) Comparison of resource requirements for a wind tunnel test designed with conventional vs. modern design of experiments method. 49th AIAA Aerospace Sciences Meeting, Orlando, Florida, USA, January 4-7

DeLoach R, Obara CJ and Goodman W (2012) A practical methodology for quantifying the random and systematic components of unexplained variance in a wind tunnel. 50th AIAA Aerospace Sciences Meeting and Exhibit, Nashville, Tennessee, USA, January 9-12

Depardon S, Lasserre JJ, Boueilh JC, Brizzi LE and Borée J (2005) Skin friction pattern analysis using near-wall PIV. Exp. Fluids 39: 805-818

Devasenathipathy S, Santiago JG, Wereley ST, Meinhart CD and Takehara K (2003) Particle imaging techniques for microfabricated fluidic systems. Exp. Fluids 34: 504–14

Discetti S and Adrian RJ (2012) High accuracy measurement of magnification for monocular PIV. Meas. Sci. Technol. 23: 117001

## References


Elsinga GE, Scarano F, Wieneke B and van Oudheusden BW (2006) Tomographic particle image velocimetry. Exp. Fluids 41: 933– 947

Falchi M and Romano GP (2009) Evaluation of the performance of high-speed PIV compared to standard PIV in a turbulent jet. Exp. Fluids 47: 509-529

Faleiros DE, Tuinstra M, van Rooijen BD, Scarano F and Sciacchitano A (2019) Soap bubbles for large-scale PIV in industrial wind tunnels. 13th International Symposium on Particle Image Velocimetry – ISPIV 2019, Munich, Germany, July 22-24

Fingerson LM and Freymuth P (1983) Thermal anemometers, in: Fluid Mechanics Measurements, (ed. RJ Goldstein) Springer, Berlin

Gonzalez RC and Woods RE (2002) Digital Image Processing. 2nd edition, Prentice Hall, Upper Saddle River, NJ

Gui L, Longo J and Stern F (2001) Towing tank PIV measurement system, data and uncertainty assessment for DTMB Model 5512. Exp. Fluids 31: 336-346

Hain R, Kähler CJ and Tropea C (2007) Comparison of CCD, CMOS and intensified cameras. Exp. Fluids 42: 403-411

Harris JR, Lance BW, Spall RE and Smith BL (2013) Transient mixed convection validation facility and study. 15th International Topical Meeting on Nuclear Reactor Thermal hydraulics, NURETH15-356

Hearst RJ and Ganapathisubramani B (2015) Quantification and adjustment of pixel-locking in particle image velocimetry. Exp. Fluids 56: 191

Hecht E (2002) Optics. 4th edition, Addison Wesley Longman Inc.

Honkanen M and Nobach H (2005) Background extraction from double-frame PIV images. Exp. Fluids 38: 348-362

Honoré D, Lecordier B, Susset A, Jaffré D, Perrin M, Most JM and Trinité M (2000) Time-resolved particle image velocimetry in confined bluff-body burner flames. Exp. Fluids [Suppl] S248-S254

Huang HT, Dabiri D and Gharib M (1997) On errors of digital particle image velocimetry. Meas. Sci. Technol. 8: 1427-40

Hummel A (1987) Representations based on zero-crossings in scale-space. IEEE Computer Vision and Pattern Recognition Conference, 204-209, June; reproduced in Computer Vision: Issues, problems, Principles and Paradigms, M Fischler and O Firschein Eds. Los Altos, CA: Morgan Kaufmann (1987)

Iannetta F, Sciacchitano A, Arpino F and Scarano F (2016) Numerical and experimental comparison of velocity derived quantities in rectangular cavity flows. 4th International Conference on Computational Methods for Thermal Problems THERMACOMP2016, Atlanta: Georgia Tech, July 6-8

International Organization for Standardization ISO (2018) Guide to the Expression of Uncertainty in Measurement

Jamison RA, Fouras A and Bryson-Richardson RJ (2012) Cardiac-phase filtering in intracardiac particle image velocimetry. Journal of Biomedical Optics, 17(3): 036007

Jones GS, Lin JC, Allan BG, Milholen WE, Rumsey CL and Swanson RC (2008) Overview of CFD validation experiments for circulation control applications at NASA. International Power Lift Conference, London, England

Kähler CJ (2009) High resolution measurements by long-range micro-PIV. VKI Lecture Series on Recent Advances in Particle Image Velocimetry, Rhode Saint Genese, Belgium, January 26–30

Kähler CJ, Astarita T, Vlachos PP, Sakakibara J, Hain R, Discetti S, La Foy R and Cierpka C (2016) Main results of the 4th International PIV Challenge. Exp. Fluids 57: 97

Kähler CJ, Sammler B and Kompenhans J (2002) Generation and control of tracer particles for optical flow investigations in air. Exp. Fluids 33: 736-742

## References


Kähler CJ, Scholz U and Ortmanns J (2006) Wall-shear-stress and near-wall turbulence measurements up to single pixel resolution by means of long-distance micro-PIV. Exp. Fluids 41: 327-341

Keane RD and Adrian RJ (1990) Optimization of particle image velocimeters part I: double pulsed systems. Meas. Sci. Technol. 1: 1202-1215

Kislaya A and Sciacchitano A (2018) Peak-locking error reduction by birefringent optical diffusers. Meas. Sci. Technol. 29: 025202

Kislaya A, Deka A, Veenstra P, Tam D and Westerweel J (2018) Ψ-PIV: A novel framework to study unsteady microfluidic flows. 19th International Symposium on the Laser and Imaging Techniques to Fluid Mechanics, Lisbon, Portugal, July 16-19

Koenderink J (1984) The structure of images. Biol. Cybern. 50: 363-370

Konrath R and Schoder W (2002) Telecentric lenses for imaging in particle image velocimetry: a new stereoscopic approach. Exp. Fluids 33: 703–8

Legrand M, Nogueira J, Jimenez R, Lecuona A and De Gregorio F (2018) Full characterization of the peak-locking error by means of orthogonal functions and application to the flow around a helicopter fuselage model. 19th International Symposium on the Laser and Imaging Techniques to Fluid Mechanics, Lisbon, Portugal, July 16-19

Legrand M, Nogueira J, Ventas R and Lecuona A (2012) Simultaneous assessment of peak-locking and CCD readout errors through multiple Δt strategy. Exp. Fluids 53: 121-135

Liao Q and Cowen EA (2005) An efficient anti-aliasing spectral continuous window shifting technique for PIV. Exp. Fluids 38: 197-208

Lin JH and Perlin M (1998) Improved methods for thin, surface boundary layer investigations. Exp. Fluids 25: 431-444

Masullo A and Theunissen R (2016) Adaptive vector validation in image velocimetry to minimise the influence of outlier clusters. Exp. Fluids 57: 33

Meinhart CD, Wereley ST and Santiago JG (1999) PIV measurements of a microchannel flow. Exp. Fluids 27: 414-419

Mejia-Alvarez and Christensen KT (2013) Robust suppression of background reflections in PIV images. Meas. Sci. Technol. 24: 027003

Melling A (1997) Tracer particles and seeding for particle image velocimetry. Meas. Sci. Technol. 8: 1406-1416

Mendez MA, Raiola M, Masullo A, Discetti S, Ianiro A, Theunissen R and Buchlin JM (2017) POD-based background removal for Particle Image Velocimetry. Exp. Therm. Fluid Sci. 80: 181-192

Michaelis D, Neal DR, and Wieneke B (2016) Peak-locking reduction for particle image velocimetry. Meas. Sci. Technol. 27: 104005

Mie G (1908) Contributions on the optics of turbid media, particularly colloidal metal solutions. Annales der Physik, Series IV 25: 377-445

Montgomery DC (2013) Design and Analysis of Experiments. 8th edition, John Wiley & Sons, New York

Montgomery DC, Peck EA and Vining GG (2011) Introduction to Linear Regression Analysis. 3rd edition, John Wiley and Sons, New York

Nobach H (2011) Influence of individual variations of particle image intensities on high-resolution PIV. Exp. Fluids 50: 919–27

Nobach H and Bodenschatz E (2009) Limitations of accuracy in PIV due to individual variations of particle image intensities. Exp. Fluids 47: 27–38

Nogueira J, Lecuona A, Nauri S, Legrand M and Rodriguez PA (2009) Multiple Δt strategy for particle image velocimetry (PIV) error correction, applied to a hot propulsive jet. Meas. Sci. Technol. 20: 074001

Nogueira J, Lecuona A, Nauri S, Legrand M and Rodriguez PA (2011) Quantitative evaluation of PIV peak locking through a multiple Δt strategy: relevance to the rms component. Exp. Fluids 51: 785-793

Nogueira J, Lecuona A, Rodríguez PA, Alfaro JA and Acosta A (2005) Limits on the resolution of correlation PIV iterative methods. Practical

implementation and design of weighting functions Exp. Fluids. 39: 314–21

Oberkampf WL and Roy CJ (2010) Verification and Validation in Scientific Computing. Cambridge University Press

Olsen MG and Adrian RJ (2001) Brownian motion and correlation in particle image velocimetry. Opt. Laser Technol. 32: 621–7

Overmars EFJ, Warncke NGW, Poelma C and Westerweel J (2010) Bias errors in PIV: the pixel locking effect revisited. 15th International Symposium on Applications of Laser Techniques to Fluid Mechanics, Lisbon, Portugal, July 5-8

Perona P and Malik J (1990) Scale-space and edge detection using anisotropic diffusion. IEEE Transactions on Pattern Analysis and Machine Intelligence, 12: 629-639

Pitot H (1732) Description d'une machine pour mesurer la vitesse des eaux courantes et le sillage des vaisseaux, Histoire de l'Académie royale des sciences avec les mémoires de mathématique et de physique tirés des registres de cette Académie, 363-376

Prandtl L (1905) Über Flüssigkeitsbewegung bei sehr kleiner Reibung, Proc. Verhandlungen des III. Internationalen Mathematiker- Kongresses, Heidelberg, 1904, Teubner, Leipzig, 404–491

Prasad AK (2000) Stereoscopic particle image velocimetry. Exp. Fluids 29: 103-116

Prasad AK and Adrain RJ (1993) Stereoscopic particle image velocimetry applied to liquid flows. Exp. Fluids 15: 49-60

Raffel M, Willert CE, Scarano F, Kähler CJ, Wereley S and Kompenhans J (2018) Particle Image Velocimetry: a Practical Guide. 3rd edition, Springer International Publishing AG part of Springer Nature

Ragni D, Schrijer FFJ, van Oudheusden BW and Scarano F (2011) Particle tracer response across shocks measured by PIV. Exp. Fluids. 50: 53-64

Rhode MN and Oberkampf WL (2012) Estimation of uncertainties for a supersonic retro- propulsion model validation experiment in a wind tunnel. 42nd AIAA Fluid Dynamics Conference and Exhibit, New Orleans, Louisiana, USA, June 25-28

Robinson SK (1991) The Kinematics of Turbulent Boundary Layer Structure. NASA Technical Memorandum 103859

Roesgen T (2003) Optimal subpixel interpolation in particle image velocimetry. Exp. Fluids 35: 252

Roth GI and Katz J (2001) Five techniques for increasing the speed and accuracy of PIV interrogation. Meas. Sci. Technol. 12: 238-245

Samimy M and Lele SK (1991) Motion of particles with inertia in a compressible free shear layer. Phys. Fluids 3: 1915-1923

Scarano F (2002) Iterative image deformation methods in PIV. Meas. Sci. Technol. 13: 1

Scarano F and Poelma C (2009) Three-dimensional vorticity patterns of cylinder wakes. Exp. Fluids 47: 69-83

Scarano F and Riethmuller ML (2000) Advances in iterative multigrid PIV image processing. Exp. Fluids 29: S51–60

Scharnowski S and Kähler CJ (2016a) Estimation and optimization of loss-of-pair uncertainties based on PIV correlation functions. Exp. Fluids 57: 23

Scharnowski S and Kähler CJ (2016b) On the loss-of-correlation due to PIV image noise. Exp. Fluids 57: 119

Scharnowski S, Bross M and Kähler CJ (2019a) Accurate turbulence level estimations using PIV/PTV. Exp. Fluids 60: 1

Scharnowski S, Sciacchitano A and Kähler CJ (2019b) On the universality of Keane & Adrian's valid detection probability in PIV. Meas. Sci. Technol. 30: 035203

## References


Schrijer FFJ, Scarano F and van Oudheusden BW (2006) Application of PIV in a Mach 7 double-ramp flow. Exp. Fluids 41: 353-363

Sciacchitano A (2014) Uncertainty quantification in particle image velocimetry. PhD thesis, Delft University of Technology, Delft University Press

Sciacchitano A (2019) Uncertainty quantification in particle image velocimetry. Meas. Sci. Technol. 30: 092001

Sciacchitano A and Scarano F (2014) Elimination of PIV light reflections via a temporal high pass filter. Meas. Sci. Technol. 25: 084009

Sciacchitano A and Wieneke B (2016) PIV uncertainty propagation. Meas. Sci. Technol. 27: 084006

Sciacchitano A, Neal DR, Smith BL, Warner SO, Vlachos PP, Wieneke B and Scarano F (2015) Collaborative framework for PIV uncertainty quantification: comparative assessment of methods. Meas. Sci. Technol. 26: 074004

Sciacchitano A, Wieneke B and Scarano F (2013) PIV uncertainty quantification by image matching. Meas. Sci. Technol. 24: 045302

Smith BL and Oberkampf WL (2014) Limitations of and alternatives to traditional uncertainty quantification for measurements. ASME Fluids Engineering Summer Meeting FEDSM2014, Chicago, Illinois

Stanislas M, Okamoto K and Kähler CJ (2003) Main results of the first international PIV challenge. Meas. Sci. Technol. 14: R63–89

Stanislas M, Okamoto K, Kähler CJ and Westerweel J (2005) Main results of the second international PIV challenge. Exp. Fluids 39: 170-191

Stanislas M, Okamoto K, Kähler CJ, Westerweel J and Scarano F (2008) Main results of the third international PIV challenge. Exp. Fluids 45: 27-71

Terra W, Sciacchitano A and Scarano F (2020) Cyclist Reynolds number effects and drag crisis distribution. Journal of Wind Engineering & Industrial Aerodynamics 200: 104143

Theunissen R, Scarano F and Riethmuller ML (2008) On improvement of PIV image interrogation near stationary interfaces. Exp. Fluids 45: 557-572

Timmins BH, Wilson BW, Smith BL and Vlachos PP (2012) A method for automatic estimation of instantaneous local uncertainty in particle image velocimetry measurements. Exp. Fluids 53: 1133-1147

Tsalicoglou C, Allegrini J and Carmeliet J (2018) PIV Measurements of the Effect of Buoyancy on Urban Flows. 19th International Symposium on the Laser and Imaging Techniques to Fluid Mechanics, Lisbon, Portugal, July 16-19

Tuinstra M, Pröbsting S and Scarano F (2013) On the use of Particle Image Velocimetry to predict trailing edge noise. 19th AIAA/CEAS Aeroacoustics Conference, Berlin, Germany, May 27-29

Tummers MJ (1999) Investigation of a Turbulent Wake in an Adverse Pressure Gradient Using Laser Doppler Anemometry. PhD Thesis, Delft University of Technology, Delft University Press

Urban WD and Mungal G (2001) Planar velocity measurements in compressible mixing layers. Journal of Fluid Mech. 431: 189-222

Violato D and Scarano F (2011) Three-dimensional evolution of flow structures in transitional circular and chevron jets. Phys. Fluids 23: 124104

Wernet MP (1997) PIV for turbomachinery applications. NASA report

Westerweel J (1993) Digital Particle Image Velocimetry – Theory and Application. PhD Thesis, Delft University of Technology, Delft University Press

Westerweel J (1997) Fundamentals of digital particle image velocimetry. Meas. Sci. Technol. 8: 1379-1392

Westerweel J (2000) Theoretical analysis of the measurement precision in particle image velocimetry. Exp. Fluids 29: S003-S012

Westerweel J (2008) On velocity gradients in PIV interrogation. Exp. Fluids 44: 831-842

## References


Westerweel J and Scarano F (2005) Universal outlier detection for PIV data. Exp. Fluids 39: 1096–100

Westerweel J, Elsinga GE and Adrian RJ (2013), Particle image velocimetry for complex and turbulent flows, Annu. Rev. Fluid Mech. 45: 409-36

Wieneke B (2005) Stereoscopic-PIV using self-calibration on particle images. Exp. Fluids 39: 267–280

Wieneke B (2015) PIV uncertainty quantification from correlation statistics. Meas. Sci. Technol. 26: 074002

Wieneke B (2017) PIV uncertainty quantification and beyond. PhD thesis, Delft University of Technology, Delft University Press

Willert CE and Gharib M (1991) Digital particle image velocimetry. Exp. Fluids 10: 181-193

Wilson BM and Smith BL (2013a) Taylor-series and Monte-Carlo-method uncertainty estimation of the width of a probability distribution based on varying bias and random error. Meas. Sci. Technol. 24: 035301

Wilson BM and Smith BL (2013b) Uncertainty on PIV mean and fluctuating velocity due to bias and random errors. Meas. Sci. Technol. 24: 035302

Xue Z, Charonko JJ and Vlachos PP (2014) Particle image velocimetry correlation signal-to-noise ratio metrics and measurement uncertainty quantification. Meas. Sci. Technol. 25: 115301

Xue Z, Charonko JJ and Vlachos PP (2015) Particle image pattern mutual information and uncertainty estimation for particle image velocimetry. Meas. Sci. Technol. 26: 074001

Yang Y (2017) Aerodynamic Interaction between Propeller and Vortex. PhD thesis, Delft University of Technology, Delft University Press

Yang Y, Zhou T, Sciacchitano A, Veldhuis L and Eitelberg G (2016) Propeller and inflow vortex interaction: vortex response and impact on the propeller performance. CEAS Aeronautical Journal 7: 419-428

# List of Publications and Awards

## Journal papers

Adatrao S, van der Velden S, van der Meulen M-J, Cruellas Bordes M and Sciacchitano A (2022) Design of Experiments: a statistical tool for PIV uncertainty quantification. Meas. Sci. Technol. 34:015201

Adatrao S, Sciacchitano A and Bertone M (2021) Multi-Δt approach for peak-locking error correction and uncertainty quantification in PIV. Meas. Sci. Technol. 32:054003

Adatrao S and Sciacchitano A (2019) Elimination of unsteady background reflections in PIV images by anisotropic diffusion. Meas. Sci. Technol. 30:035204

## Conference proceedings

Adatrao and Sciacchitano (2022) Survey on PIV errors and uncertainty quantification. 20th International Symposium on Applications of Laser and Imaging Techniques to Fluid Mechanics, Lisbon, Portugal, July 11-14

Adatrao S, Sciacchitano A, van der Velden S, van der Meulen and Cruellas Bordes M (2021) Design of Experiments: a statistical tool for PIV uncertainty quantification. 14th International Symposium on Particle Image Velocimetry ISPIV 2021, Chicago, Illinois, USA (online), August 1-4

Adatrao S and Sciacchitano A (2019) Multi-Δt approach for peak-locking error correction and uncertainty quantification in PIV. Workshop on Frontiers of Uncertainty Quantification in Fluid Dynamics, Pisa, Italy, September 11-13

Adatrao S and Sciacchitano A (2019) Multi-Δt approach for peak-locking error correction and uncertainty quantification in PIV. 13th International Symposium on Particle Image Velocimetry ISPIV 2019, Munich, Germany, July 22-24

## Awards

Measurement Science and Technology journal's outstanding paper award of year 2019 in optical and laser-based techniques category for the article- "Elimination of unsteady background reflections in PIV images by anisotropic diffusion" (https://iopscience.iop.org/article/10.1088/1361-6501/ab7efb)